Resistance Spot Weld Fatigue Life Prediction Method Compatibility with Self-Piercing Rivets

by

Alan Woo

A thesis
presented to the University of Waterloo
in fulfillment of the
thesis requirement for the degree of
Master of Applied Science
in
Mechanical and Mechatronics Engineering

Waterloo, Ontario, Canada, 2022

Author's Declaration

I hereby declare that I am the sole author of this thesis. This is a true copy of the thesis, including any required final revisions, as accepted by my examiners.

I understand that my thesis may be made electronically available to the public.

Abstract

The Resistance Spot Weld (RSW) is traditional method for structural sheet metal joining with well established durability assessment techniques and methodologies. With increased prevalence of multi-material automotive structures to optimize vehicle light weighting for increased product quality and environmental concerns, traditional joining methods are limited in their capabilities. Alternative joining methods are required that are capable of joining dissimilar materials while maintaining strength and durability. The Self Piercing Rivet (SPR) is an alternative joining method capable of achieving this requirement and providing other economical and manufacturing workplace benefits. Durability assessment of sheet metal joints is essential for the optimum design of automotive sheet metal structures.

While there is no established fatigue life prediction model for SPR joints, Rupp's model is a well established fatigue life prediction method for the RSW joint with a modernized adaptation available in the commercial software nCode DesignLife. The Rupp's model was chosen due to prevalence in industry use, computational efficiency, and ability to capture various loading conditions. The only requirements of this methodology are specimen level experimental fatigue lives and low element count finite element models. The purpose of this study is to investigate the compatibility of SPR joints with the nCode Rupp's model intended RSW joints. An initial study is made with SPR compatibility with the nCode Rupp's model with uniaxially loaded SPR specimens of various configurations collected from literature. Results of this study showed that Rupp's model is compatible with uniaxially loaded SPR specimens and provided confidence to extend this study to cross-tension multiaxially loaded specimens.

Experimental work was performed to obtain fatigue lives of dissimilar thickness Al 6016 SPR joints and dissimilar material Al 6016 and DX54D steel joints under uniaxial and multiaxial loading. Experimentation yielded a pool of data with documentation on failure modes of both joints. Further investigation on the compatibility of nCode Rupp's model was performed with this newly obtained set of data which introduced a wider range of specimens for fatigue life prediction. Compatibility and performance of nCode Rupp's model was clearly seen with this second study.

Clear differences in geometry and joining mechanisms exist between SPR and RSW joints. Studies were performed to investigate these differences with finite elements to understand the differences in stress state of the two joint types. In uniaxial tensile loading of SPR joints Rupp's model overpredicts bending stresses due to slippage allowed by SPR mechanical interlock whereas RSW joints are completely fused. In uniaxial shear loading of SPR joints Rupp's model underpredicts the bending stresses due to the out of plane deformation in the top sheet causing a greater moment arm.

Compatibility of nCode Rupp's model is validated for uniaxially and multiaxially loaded dissimilar material and thickness cross-tension SPR specimens with a collection of experimental results and failure mode documentation.

Acknowledgements

I would like to express my gratitude towards Professor Hamid Jahed for accepting me into his research group and the unrelenting and continuous support provided throughout the entirety of this degree. The availability and patience exercised is profound to me along with the excellent guidance provided.

I would also like to express my gratitude to Dr. Seyed Behzad Behravesh, who provided me with invaluable knowledge and guidance throughout the entirety of this degree with remarkable friendliness.

Lastly, I would like to thank Christine Royer, Saeid Rezaee, Amelie Malpot, Nicolas Fajal and Valerie Klejnot of the industry partner Alliance Renault Nissan Mitsubishi for providing financial support and opportunity to perform the research contained in this document.

Table of Contents

List of Figures

List of Tables

1. Introduction

The concept of vehicle light-weighting is prominently used in the automotive industry to address the paramount environmental issues of today's world while also constantly improving vehicle designs towards their optimum state. Sheet metal structures of a vehicle presents itself as a suitable vehicle system for light-weighting due to the number of components and their varying structural requirements. Traditionally vehicle chassis are comprised of sheet metal structures made of a single material such as steel or aluminum although with introduction of multi-material chassis automotive manufacturers can achieve new levels of vehicle light-weighting while maintaining rigidity and crashworthiness [1].

With introduction of the multi-material chassis a new challenge presents itself in the form of joining dissimilar sheet materials as the conventional method of resistance spot welding or also called spot welding is not suitable. An alternative joining method that addresses the challenge of joining dissimilar sheet materials is the self-piercing rivet or SPR [2], [3]. The SPR joining process uses a high-strength steel semi tubular rivet that is mechanically driven through multiple sheets of material at room temperature resulting in mechanical interlock with the aid of a die. SPR offers several advantages in addition to dissimilar material joining including no welding fumes, no welding sparks, lower energy consumption, negligible heat generation, joining over 2 sheets of material, joining difficult or unweldable materials, and does not require a pre-drilled hole.

1.1. Objective

The objective of this thesis is to validate compatibility of Rupp's model, an existing RSW fatigue life prediction method, with fatigue prediction of dissimilar thickness aluminum-aluminum and aluminum-steel SPR joints under uniaxial and multiaxial loading and to establish a life prediction model for durability assessment of SPR joints.

1.2. SPR Fatigue Life Prediction and Model Development

Fatigue analysis is required for any structural system subject to cyclic loading where durability assessment is required [4]. In the case of the automobile, cyclic loading is generated through regular usage from sources including operator inputs such as steering, acceleration or deceleration and traversing road irregularities such as bumps and cracks. Durability assessment of vehicle chassis and other sheet metal structures must include assessment of joints as they are stress concentration sites and can govern the durability of the overall component. Establishing a method to determine durability will allow joined sheet metal structures to be optimally designed ensuring the best joint locations and establishing the minimum number of required

joints. Reduction of redundant joints results in cost and environmental impact reduction through the improvement of manufacturability. With the introduction of SPR as a new sheet metal joining technology, a fatigue life prediction method must be procured to contribute to the durability assessment of SPR joined sheet metal structures.

While fatigue prediction model is needed for SPR joints, fatigue life prediction method of the spot weld joint by Rupp et al. [5] is well established and the methodology has been implemented in the commercial fatigue and durability analysis software nCode DesignLife [6]. Rupp's model provides methodology to extract spot weld joint tractions from simplified finite element models and uses extracted tractions as inputs for a set of structural stress equations to transfer experimental load-life experimental results to stress-life. Once results of various sets of experiments are overlaid in a single chart, the stress-life results have significantly less scatter than that of load-life results allowing a master curve to be created. While using nCode's adaptation of Rupp's model, stress-life results can then be further improved with statistical optimization. In addition to commercial availability, Rupp's model offers advantages including ease of use, computational efficiency, and capturing various loading and boundary conditions.

Since SPR and spot weld joints have same overall function and similar geometry, compatibility of using Rupp's model for the fatigue life prediction of SPR joints is investigated. Due to geometrical and bonding mechanism differences between SPR and RSW joints the need for model modifications is investigated.

1.3. Outline

Chapter 2 documents previous work done by other researchers in the field of SPR durability analysis and other relevant literature. Chapter 3 documents methodologies for experimental work, SPR fatigue life prediction and statistical optimization. Chapter 4 provides an example and initial investigation of Rupp's model applied to experimental uniaxially loaded SPR fatigue data obtained from literature. Chapter 5 describes quasistatic and cyclic experimental results from uniaxial and multiaxial testing performed at The University of Waterloo. Chapter 6 documents Rupp's model application to Renault Group and The University of Waterloo's test results to further investigate Rupp's model compatibility with SPR joints. Chapter 7 documents comparison between stress states of SPR and RSW joints with finite element modelling. Chapter 8 and 9 summarizes the results of this thesis and outlines potential future work in this area.

2. Background and Literature Review

This chapter documents review of previous work performed by other researchers in the field of the SPR process, SPR quasistatic and fatigue experimental results, and SPR and RSW fatigue life prediction including optimization. An overview of the SPR process details and parameters, technology application, mechanical performance, and other engineering details such as quality control and finite element modelling have been compiled [2], [3].

2.1. SPR Background and Joining Process

Although SPR originated in the 1960s, emergence of the technology in the automotive industry occurred at the beginning of the 1980s as a potential solution to join dissimilar structural sheet materials for vehicle light-weighting [7]. By the 1990s and 2000s automotive manufacturers Audi AG and Jaguar Cars Limited incorporated SPR joints in production vehicles [8], [9]. Since 2016 automotive manufacturers including Audi AG, BMW AG, GM, Jaguar Land Rover Limited and Tesla Inc. have all used SPR technology to join dissimilar material sheet structures in their vehicles [10].

Figure 1: Typical pre-process SPR with varying length. Note sharp edge at open end for sheet piercing and countersunk closed end [2]

SPR is a mechanical joining process where a rivet is driven at room temperature by mechanical force, fully piercing though a single or a multiple stack of sheets and partially piercing and clenching the final bottom sheet. The SPR itself is a high strength steel rivet with a semi-tubular geometry with one open end. Tooling is required to provide lower initial camping force to hold the workpiece in place, high load to drive the SPR to pierce and deform workpiece, and a frame to hold the receiving die. The process steps are as follows:

1) Clamping: The tool applies a perpendicular initial clamping force to hold the workpiece in place in between punch/rivet side and die side of the tool.

2) Piercing: The punch of the tool applies load directly to the SPR's closed side causing the open side to push and pierce though the workpiece.
3) Flaring: Once the SPR has been pushed to a certain point, geometry of the die causes the open side of the SPR to begin flaring outwards radially. Further pushing from the punch causes the clenched sheet to flow into the die axially and radially until desired geometry is formed.
4) Release: The punch is retracted freeing the workpiece.

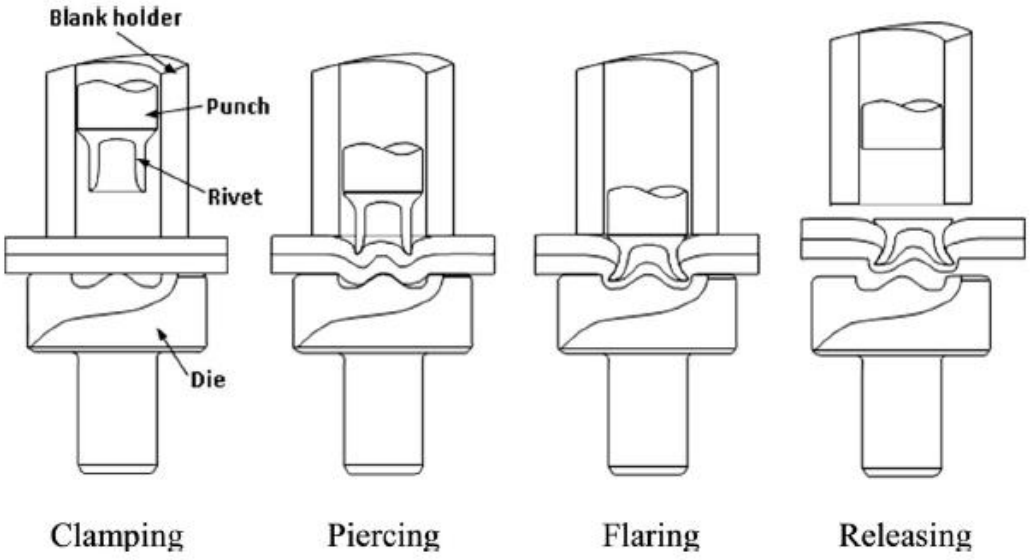

Figure 2: Schematic of SPR process [2]

Compared to traditional and other alternative sheet joining methods, SPR advantages include:

1. Joins multiple similar or dissimilar materials of varying sheet thicknesses including steel, aluminum, magnesium, plastics, and composites.
2. Mechanical joining process results in negligible generated heat maintaining heat treated sheet material properties
3. High static and fatigue strength.
4. Environmentally and operator friendly: no fumes, no sparking, no excessive noise, no debris or other waste material, and minimal heat.
5. While typical rivets require pre-drilled or pre-punched holes, SPR does not.
6. Lower energy consumption compared to traditional RSW joining method.
7. SPR joints can be checked for quality visually, to some degree.
8. Fast cycle time.
9. Compatible with lubricated, coated, or painted surfaces.
10. Compatible with adhesive joints.

Although the SPR process brings many advantages, there are some disadvantages:

1. Access to both sides of the sheet joint is required.
2. Significant deformation caused by the clenching process limits clenched sheet material by ductility.
3. While SPRs include a countersunk head to allow the rivet itself to sit flush to the first pierced sheet, a protrusion is formed in the clenched sheet. Results in non-class A surface which may painting and coating difficulties.
4. SPR process includes forming, high force is required.
5. Higher consumable costs relative to RSW.

2.2. SPR Quasistatic and Cyclic Experimental Work

Testing of sheet joints is commonly performed at a specimen level to characterize behavior before the application to a component level. Differences in the commonly used specimen configurations of SPR joints are shown in *Figure 3*. Tensile-shear configuration specimens connect two partially overlapping flat sheets with the joint at the center of the sheet overlap. Coach-peel configuration specimens have a 90° bend in each sheet to create two tabs which are joined together at the center. Cross-tension configuration specimens connect two overlapping flat sheets at the center of each sheet with one sheet rotated 90° in plane relative to the other.

Tensile-shear and coach-peel configuration specimens are tested by fixing both sheet ends of the test specimen to a load frame while the cross-tension specimens have four fixed sheet ends. Coach-peel specimens can be immediately tested with conventional gripping mechanisms found on commercially available load frames while the tensile-shear configuration required additional spacers joined to either clamed edge so that the center of the sheet joint is not offset from one gripping mechanism to the other. Cross-tension specimens require entirely custom test fixtures or adapters that can incorporate the additional functionality of testing at various angles. While the nature of the cross-tension configuration allows for testing at various angles, the tensile-shear, and coach-peel configurations both can only be loaded in one direction for meaningful joint durability results. Once a test specimen is fixed to the testing apparatus, the load frame applies cyclic load based on user inputs such as load level, load ratio and frequency until failure. For sheet metal joint specimens load ratios are typically greater than 0 to prevent any specimen buckling due to the compressive forces.

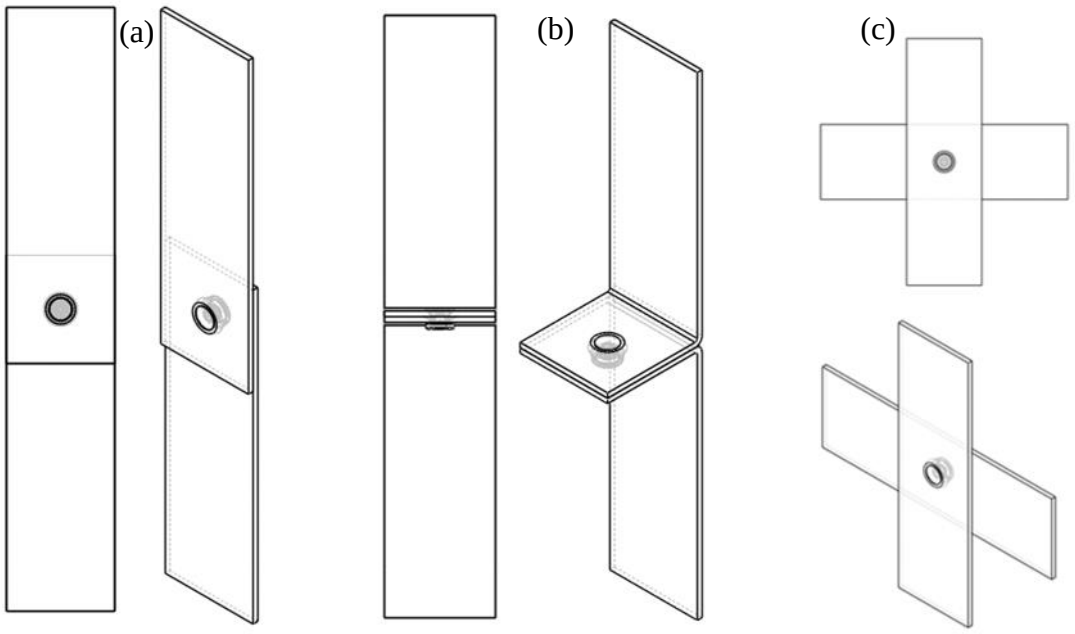

Figure 3: Front and isometric views of common sheet metal joint specimen configurations (a) tensile-shear (b) coach-peel and (c) cross-tension

While most advantages and disadvantages of SPR joints are distinct, the static and fatigue strength of SPR compared to the traditional and other alternative joining methods have been validated by previous researchers. Han et al. [11] have compared the static strength between aluminum SPR and RSW joints and the effect of varying sheet thickness combinations. Direct comparison of static strength is inconclusive due to the range of specimen geometries and sheet thickness combinations. However, it was concluded that coach-peel specimen configuration achieved similar or higher strengths than RSW, strength of the dissimilar thickness SPR joints is highly dependent on the stacking orientation of the sheets, and overall performance of SPR joints improves with increasing sheet thickness. Yan et al. [12] investigated strength of RSW alternative joining methods, where static tests were performed with SPR, blind rivet, self-drilling screws and clinching. Results show that SPR consistently have highest strength at sheet thicknesses of 1mm and above and show similar or slightly lower strength values with 0.8mm sheet thickness specimens *Figure 4*. Su et al. [13] present detailed comparison of fatigue strength of tensile-shear configuration Al 6111 SPR and clinch joint specimens where average strength of SPR is approximately 11.5% higher. Booth et al. [14] investigated static and cyclic strength differences between steel and aluminum SPR and RSW joints concluding that RSW steel joints have higher static strength than SPR steel joints, strength difference between SPR and RSW aluminum joints is ambiguous, and fatigue strength of SPR is typically higher than that of the RSW joints *Figure 5 (left)*. Although further investigation to why SPR typically have higher fatigue life is required, it is suggested that stress concentrations in SPR are less severe than RSW due to

smoother changes in joint geometry. Cai et al. [15] have also documented high fatigue strength of SPR joint compared to both RSW and clinching methods of joining *Figure 5 (right)*.

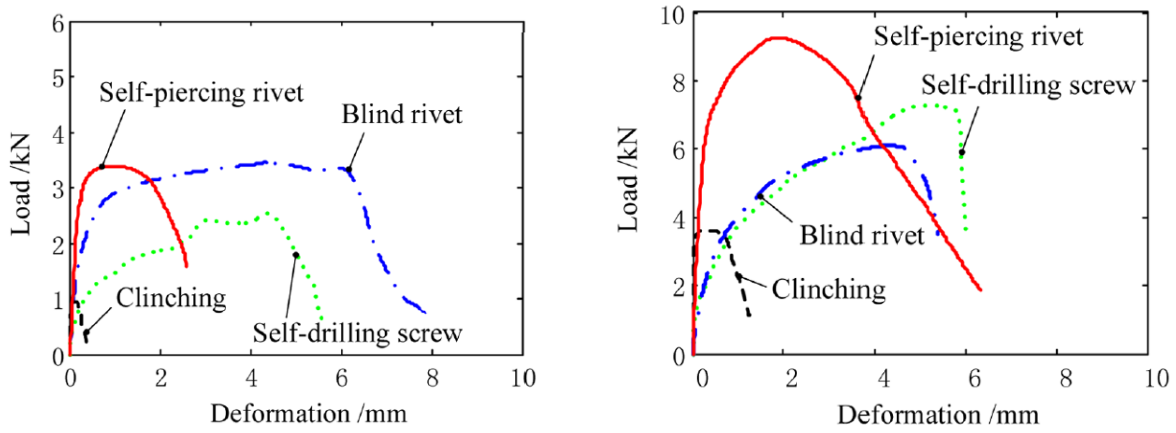

Figure 4: Static strength comparison of SPR and other RSW alternative joining methods clinching, self-drilling screw and blind rivet [12]

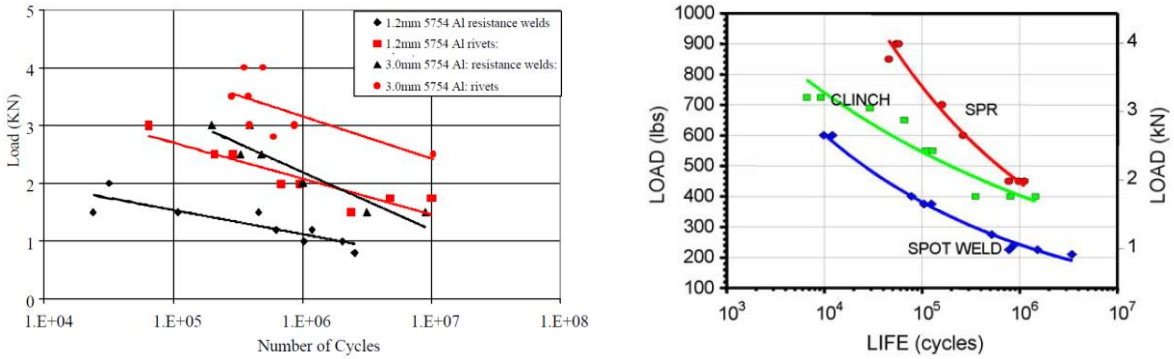

Figure 5: Fatigue life performance comparison between Al 5754 SPR and RSW joints (left) [14], *fatigue life performance comparison between SPR, clinch and RSW joints (right)* [15]

Fatigue behavior of various SPR joints under uniaxial loading have been well documented by previous researchers [13], [14], [16]-[26]. Fu [16] and Iyer et al. [17] investigated fatigue behavior and failure modes of Al 6111 and Al 5754-O tensile-shear specimens respectively, and Zhang et al. [18] performed similar work with titanium specimens. Huang et al. [19], [20] performed fatigue tests on HSLA340 and Al 6111 SPR tensile-shear joints with similar and dissimilar material specimens of various sheet thickness. The following researchers have further contributed to SPR knowledge areas by determining the effects of different specimen geometries as seen in *Figure 3* under uniaxial loading. Booth et al. [14] performed SPR fatigue tests with aluminum, high strength steel, and coated high strength steel joints of same thickness and material combinations in tensile-shear and coach-peel specimen configurations. Khanna et al. [21] investigated effects of varying different sheet thickness combinations and varying fatigue load ratios in Al

6111 SPR tensile-shear and coach-peel configurations, showing higher load ratios result in higher fatigue life. Kang et al. [22] investigated fatigue behavior differences between Al-5052 coach-peel, tensile-shear, and cross-tension specimen configurations. [23] Sun et al. investigated fatigue strength of aluminum to aluminum and aluminum to steel SPR joints in tensile-shear and cross-tension specimen configurations. Typically, under cyclic loading, SPR specimens of tensile-shear configuration have higher fatigue strength than coach-peel configuration indicating SPR joints have higher strength in shearing direction than axial or pullout direction. Regardless of specimen configuration, maximum load levels increase with thicker sheet specimens. For joints with same thickness and material type for both sheets, typical mode of failure is cracking in the top pierced sheet *Figure 6*. For dissimilar thickness or material SPR joints, fatigue strength is sensitive to stacking orientation and strength is mainly determined by the thinner sheet. It should be noted that majority of existing SPR fatigue research has been performed on tensile-shear and coach-peel specimen orientations with minimal work performed with cross-tension specimens. Distinct lack of work on multi-axial loading of SPR joints is also apparent. A benefit of the cross-tension specimen is suitability for muti-axial loading due to higher area moment of inertia compared to tensile-shear and coach-peel specimen orientations.

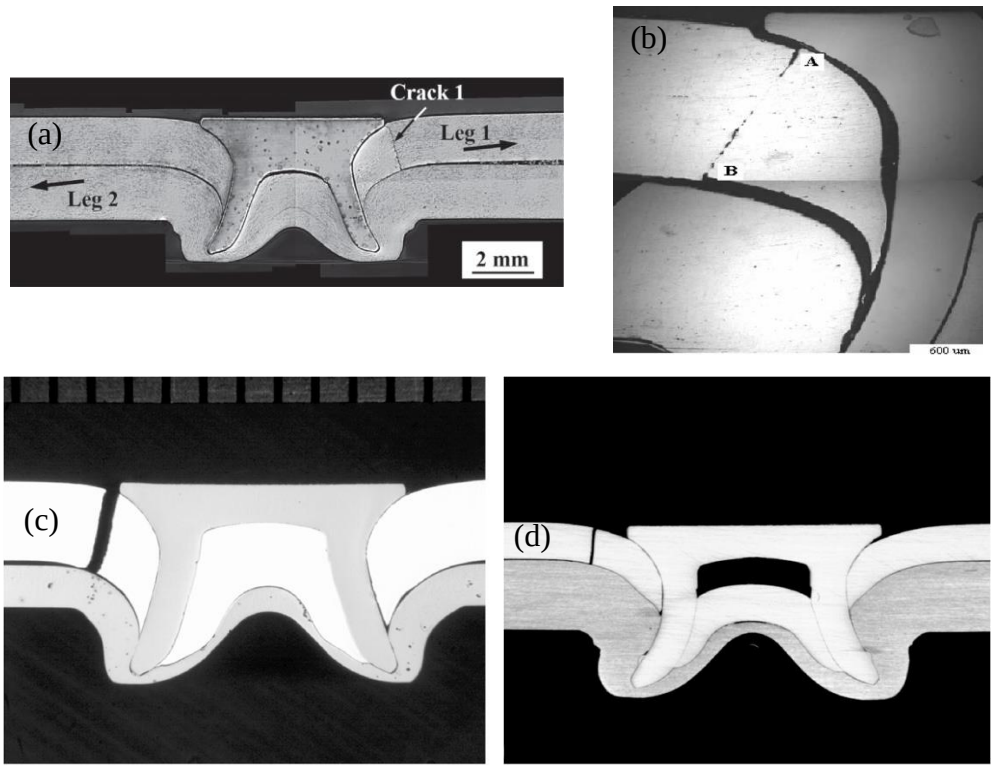

Figure 6: Images of common SPR top pierced sheet fatigue failure from literature (a) Al 6111- T4 2mm by 2mm [13], *(b) Al 6111 equal top pierced and bottom clenched sheet thickness* [21], *(c) Al 5182-O 2mm top sheet by HSLA 350 1mm* [23] *and (d) HSLA 350 1mm by Al 5182-O 2mm* [23]

Since application of SPR is primarily in the automotive industry as replacement for traditional RSW joining method, it should be noted that fretting wear occurs in SPR joint due to the mechanical interlocking between SPR and sheet, and from pierced to clenched sheet contact interfaces. Han et al. [24] and Zhao et al. [25] both identified crack initiation causing rupture failure occurs in fretting regions of tensile-shear Al 5754 and Al 5052 SPR joints respectively. Others have documented occurrence and details of fretting in SPR aluminum to aluminum and aluminum to steel joints; however, have not made any conclusive observations on effects of fretting with fatigue life [26], [27], [28]. While the occurrence and correlation of fretting is documented by previous research, characterization of the effects of fretting and fatigue life of SPR joints is still undetermined.

2.3. SPR and RSW Fatigue Life Prediction

To perform durability assessment of joined sheet structures, fatigue life prediction methods are required early in the design process. Su et al. [13] included fatigue life prediction method by using structural stress equations derived from spot weld geometry correlating SPR experimental and calculated results. Huang et al. [19], [20] used fracture mechanics to derive stress intensity factors for SPR fatigue life prediction. While studies performed in [13], [19], [20] showed good results, durability assessment is restricted to tensile-shear specimen configuration. Kang et al. [22] included fatigue life prediction for tensile-shear, coach-peel, and cross-tension specimen configurations of Al 5052 SPR joints with established RSW stress intensity factors [29] for each individual specimen configuration, yielding promising results.

While effective, previously mentioned SPR fatigue life prediction methods are all configuration dependent. Rupp et al. in 1995 [5] presented a spot weld fatigue life prediction method for steel sheet RSW joints independent of specimen configuration, applicable at an early stage in the design phase requiring only simplified finite element modelling and experimental results of component-like specimens. Rupp's model process then uses tractions obtained from the simplified finite element model to convert and collapse load-life plots to stress-life plots yielding a master curve for fatigue life prediction. The commercial software nCode DesignLife includes updated adaptation of the original 1995 Rupp's model to include aluminum spot weld joints, robust joint modelling methods, and empirical factors for statistical optimization [6]. Rupp's model has been used successfully for SPR fatigue life prediction by Jaguar Land Rover Limited [30] with tensile-shear and coach-peel specimens, and in literature by Rao et al. [31], [32] when investigating fatigue behavior of aluminum to aluminum and aluminum to carbon fiber reinforced polymer tensile-shear joints. Rao et al. [32] also compare performance of Rupp's model to a modified Battelle structural stress method [33], another structural stress method with a similar process and methodology as Rupp's model, showing good collapse after load-life to stress-life conversion with both models. While

previous researchers have presented validation for use of Rupp's model and other RSW life prediction methods in uniaxial SPR joint fatigue life prediction, current work for validation of uniaxial SPR joint fatigue of varying specimen configurations, and multiaxial SPR joint fatigue life prediction is lacking. Some researchers [13], [22], [30], [31], [32], [33] have used models with simpler RSW-like geometry to geometrically represent SPR joint. While this does yield good results there is minimal study on the effects of the complex geometry of SPR and its effect on fatigue life.

2.4. Statistical Optimization

Statistical optimization has been used to further improve Rupp's model data collapse when converting load-life to stress-life with RSW [34] and SPR joints [30] with empirical factors found in nCode DesignLife [6]. The non-linear generalized reduced gradient method (GRG) used in Microsoft Excel's Solver add-in used in [34] is also used in this document to perform statistical optimization. The GRG method in engineering design applications was introduced in 1977 [35] while the process is summarized in [34] and documented in detail in [36].

2.5. SPR Detailed Finite Element Modelling

Several researchers [17], [20], [22], [37] have created models with finite element analysis to study joint deformation modes and stress states SPR joints of various specimen configurations. Iyer et al. [17] created 2D models for local stress analysis using elastic elements and assumed friction coefficient μ =0.2 at all contact interfaces, and 3D models in ABAQUS/Standard with 27 node brick and 15 node prismatic element and single-node slide surface elements. Huang et al. [20] created a detailed finite element model to predict fatigue damage in ABAQUS with 20 node quadratic hexahedron elements (C3D20) and used an assumed friction coefficient μ = 0.2 at all contact interfaces. Kang et al. [22] also used ABAQUS (version 6.6) to determine stress and crack initiation position relations, with linear triangular prism (C3D6) and linear brick (C3D8) elements and used μ = 0.20 and μ = 0.15 for the friction coefficients between the top pierced sheet and bottom pierced sheet respectively. The finite element work performed by the previously mentioned researchers have the goal of understanding the behavior of SPR post joining process and under uniaxial static loading. Additional detailed finite element modelling is presented in this document to investigate the stress state of SPR and compare to the commonly substituted geometry of the RSW joint used in SPR fatigue life prediction.

3. Methodology

The methodology for experimentation, SPR fatigue life prediction, statistical optimization and finite element modelling are documented in this section.

3.1.Experiential Methodology

This experimental methodology section documents materials and geometry of specimens used for experimentation and quasistatic and fatigue testing methodology.

3.1.1. Experimental Specimens

Renault Group has manufactured SPR cross-tension specimens with the following three different sheet combinations, Al 6016 1mm by 1mm, 6016 1mm by DX54D 0.95mm and Al 6016 2mm by 1mm. *Table 1* tabulates quantity of Renault manufactured specimens and their respective testing locations and *Table 2* tabulates the loading orientations, test type and quantities performed at The University of Waterloo.

Table 1: Quantities of cross-tension specimens manufactured by Renault Group and test locations

Specimen	Test Location	
	Renault Group	University of Waterloo
Al 6016 1mm x DX54D 0.95mm	41	13
Al 6016 2mm x 1mm	0	55
Al 6016 1mm x 1mm	50	0

Table 2: Quantities of cross-tension specimens tested at The University of Waterloo

Specimen	Orientation	Loading	
		Quasistatic	Fatigue
Al 6016 1mm x DX54D 0.95mm (quantity = 13)	45°	1	7
	90°	2	3
Al 6016 2mm x 1mm (quantity = 55)	45°	3	3
	90°	22	27

The Al 6016 1mm top sheet is pierced and the bottom DX54D sheet is clenched in 6016 1mm by DX54D 0.95mm specimens and the 2mm top sheet is pierced and the bottom 1mm sheet is clenched for Al 6016 2mm by 1mm specimens. *Figure 7* shows dimensions of the metal sheets used for construction of cross-tension specimens tested at Renault Group and the University of Waterloo with two holes to accommodate locating and fixture clamping.

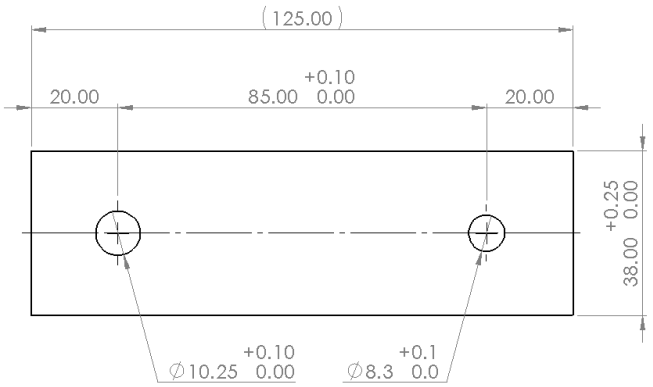

Figure 7: Single sheet geometry for Renault Group and University of Waterloo SPR cross-tension specimen sheet metal joint testing

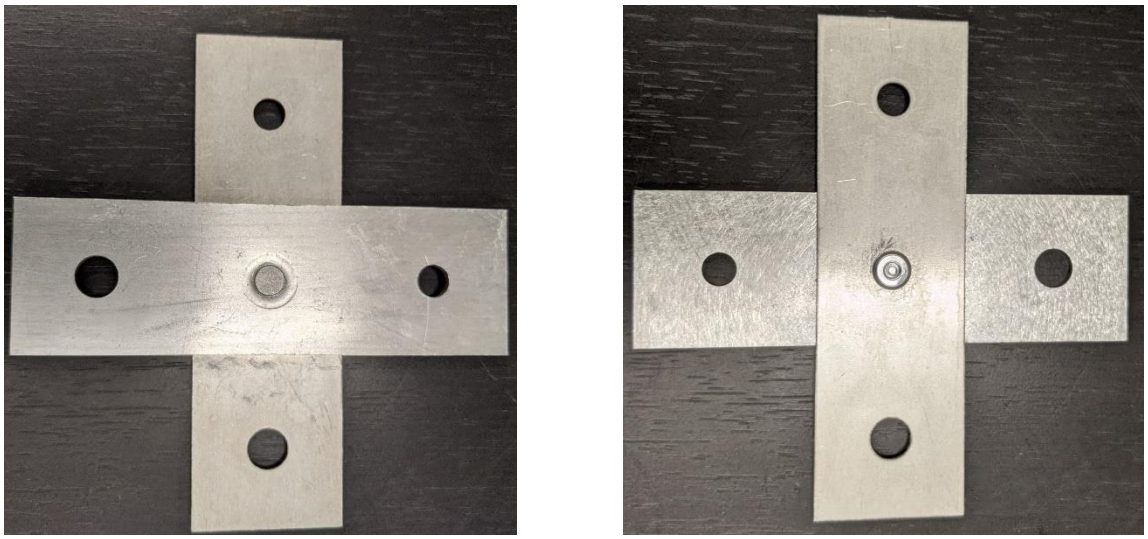

Figure 8: As received Al 6016 2mm by 1mm SPR cross-tension specimens showing SPR head and pierced 2mm pierced sheet (left) and 1mm clenched sheet (right)

3.1.2. Cross-Tension Sheet Metal Joint Test Fixture

The importance of multiaxial loading in materials [38], [39], [40], [41] and welds [42], [43] have been documented. Testing of cross-tension specimens is completed in multiple loading orientations to study associated effects on specimens. In 90° orientation the SPR cross-sectional area in plane with the contact interface of the two sheets is in pure shear, while in 0° the same cross-sectional area is in pure tension. In 45° orientation and any other intermediate angle between 0° and 90° will have combined stress state at the same cross-sectional area.

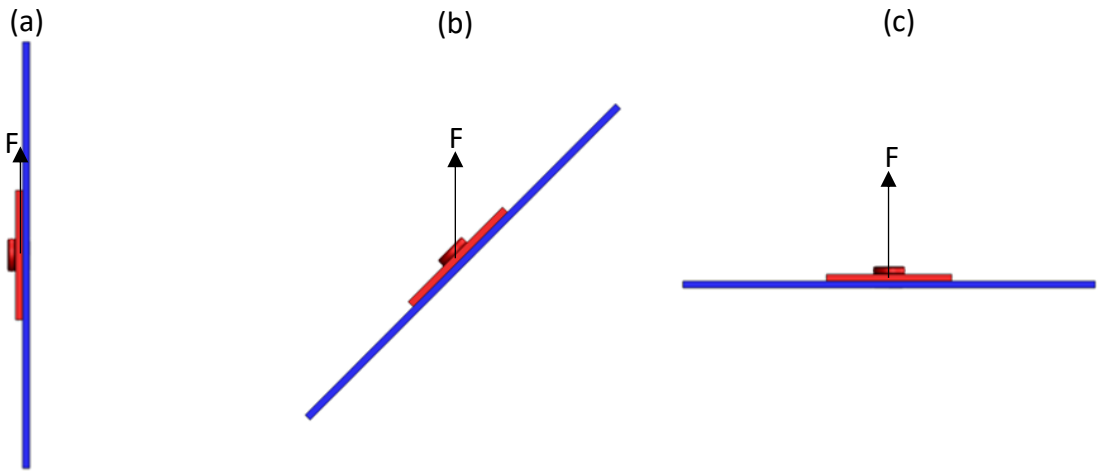

Figure 9: Loading orientations for cross-tension configuration SPR joints where load is applied to the ends of the red coloured sheet and ends of blue sheet are fixed (a) 90° (pure shear), (b) 45° (combined) and (c) 0° (pure tension)

A test fixture was designed and fabricated at the University of Waterloo to perform quasistatic and fatigue testing of cross-tension sheet metal joints with same geometry and loading orientations as the Renault Group fixture. The cross-tension fixture shown in *Figure 13* consists of a fixed frame with two linear motion shafts and interfaced to make a bolted connection to one sheet of the specimen. An inner carriage with linear motion bearings allows axial displacement along linear motion shafts of the fixed frame and has similar interfacing to allow a bolted connection to the other sheet of the cross-tension specimen. A tabbed bar with clevis attached to the carriage allows for conventional load frame grippers to grip and apply load or displacement. The fixture has been designed to perform quasistatic and fatigue testing of cross-tension sheet metal joints with overall thickness maximum of 6mm and a maximum load of 20kN at either 0°, 22.5°, 45°, 67.5° and 90° loading orientations. Fixture design includes features to locate specimens for maintaining test consistency from specimen to specimen. The two inner components that directly contact the specimen or the shim were fabricated with heat treated 4140 steel for strength, while the remainder of fabricated components where fabricated from plain carbon steel.

The commercial finite element software ABAQUS 2019 was used to validate fixture functionally prior to manufacturing. The finite element model in *Figure 10* contains 321,253 total elements with three linear motion bearings modelled as rigid bodies, 183,249 linear elastic tetrahedral and hexahedral elements modelling less critical fixture components fabricated from plain carbon steel, and 138,004 quadratic elastic tetrahedral elements used to model critical fixture 4140 components and the sheet metal joint itself. All bolted connections were modelled with tie connections with no solid bodies representing actual fasteners and general contact modelled at linear motion bearing to linear motion shaft contact interfaces, and sheet

metal joint top to bottom sheet contact interfaces. An applied load of 20kN is applied to the clevis where the load frame clamps to the fixture with all rotational, x and z degrees of freedom fixed, and the fixture base is fixed in all rotational and linear degrees of freedom.

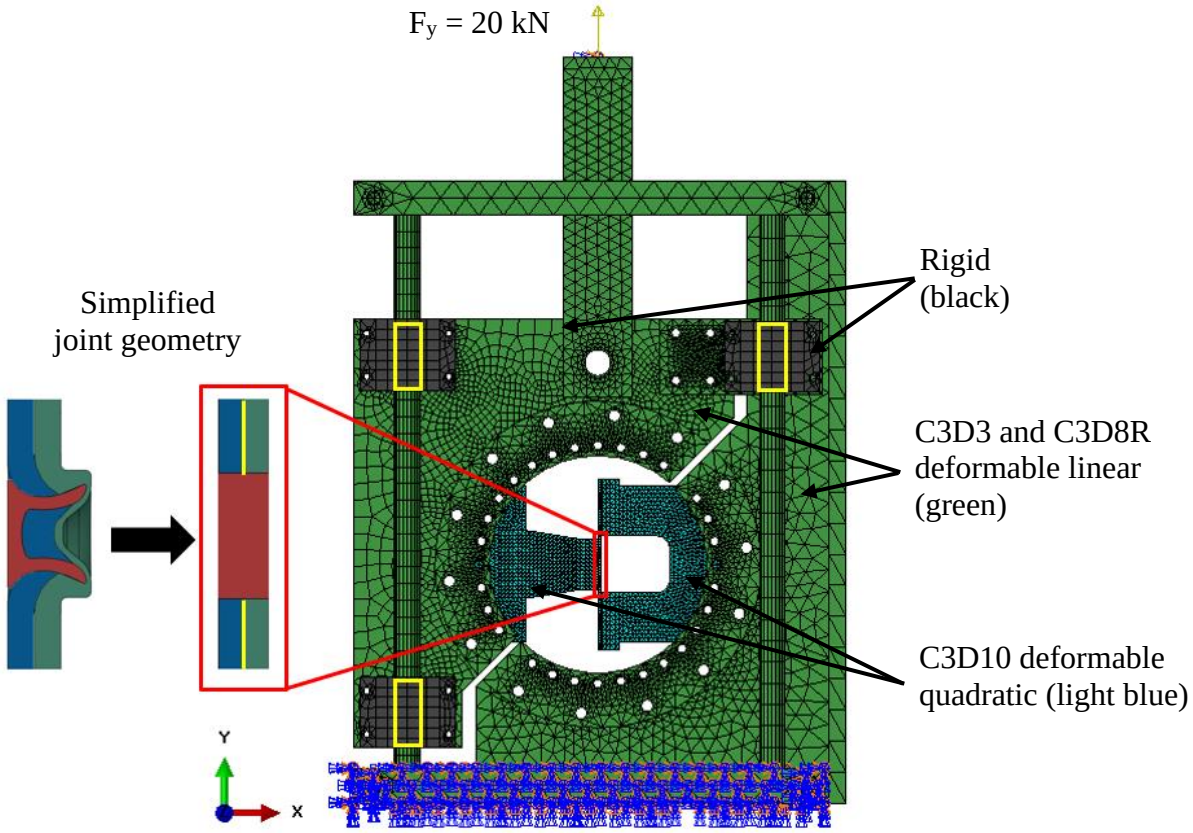

Figure 10: Cross-tension sheet metal joint test fixture Finite Element model with SPR geometry simplification with aluminum top sheet (blue), aluminum bottom sheet (green), SPR steel joint (red) in left images and yellow lines indicating general contact interfaces

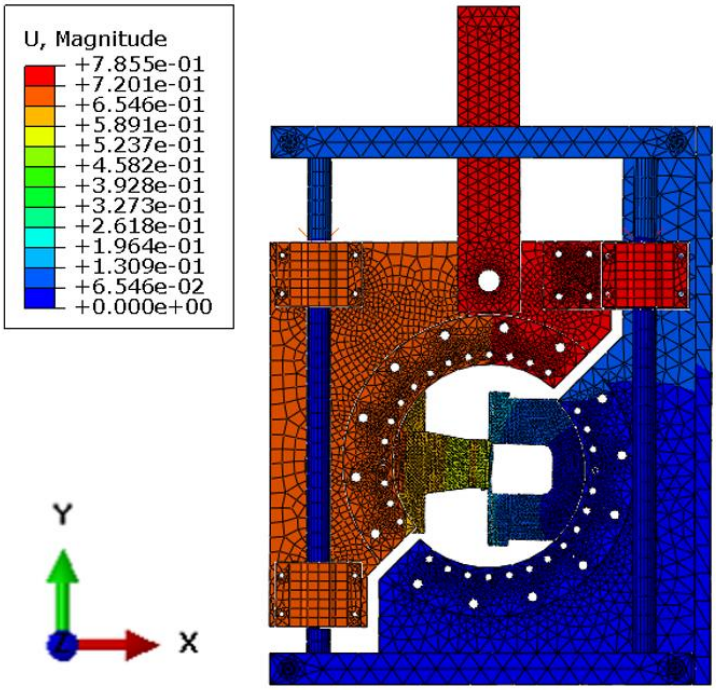

Figure 11: Displacement contour plot of Finite Element model in Figure 10

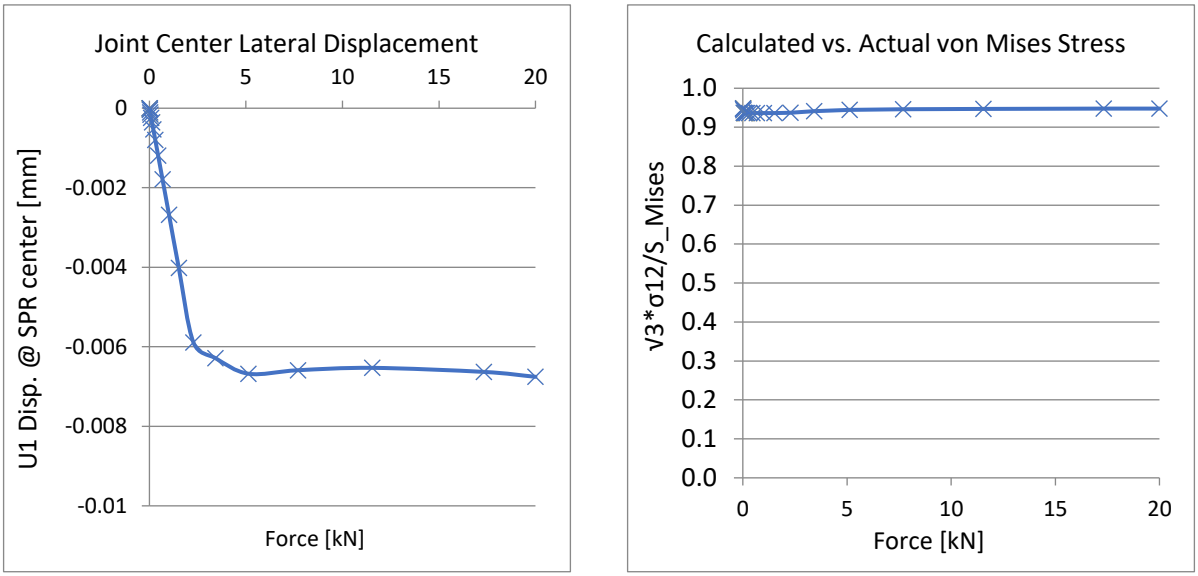

Figure 12: Lateral displacement of sheet metal joint center with 20kN applied load (left) and shear stress ratio with 20kN applied load (right)

Two plots shown in *Figure 12* validate functionality of the cross-tension fixture, where the 90° pure shear orientation is most critical to observe since any lateral deflection is undesirable yet nevertheless will occur due to specimen and fixture geometry. A straightforward method to determine lateral deflection is to obtain

the displacement along the x-axis specimen joint center. *Figure 12 (left)* shows minimal lateral displacement of 6.755 μm at the specimen center with applied load of 20 kN. An alternative method to check functionality in the 90° pure shear orientation uses von Mises stress in the pure shear state where:

$$\sigma_{mises} = \sqrt{3}|\sigma_{12}| \quad (1)$$

A ratio is calculated with equation (1) and actual von Mises stress where σ_{12} and actual von Mises stress are both obtained from finite element post processing. A specimen in pure shear will result in a ratio between calculated and actual von Mises of 1. It can be seen in *Figure 12 (right)* where a ratio of 1 is nearly achieved where all ratios are within the range of 0.9364 and 0.9483.

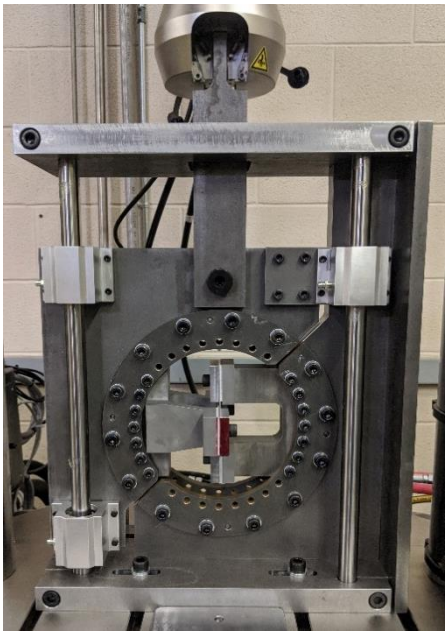

Figure 13: Cross-tension configuration sheet metal joint test fixture in 90° (pure shear) loading orientation

3.1.3. Quasistatic Test Procedure

The Instron 8872 Linear Fatigue Testing System with 25kN load capacity is used with the cross-tension fixture to complete the specimen testing. A limited quantity of quasistatic tests was completed for each specimen at both 90° and 45° loading orientations to observe behavior and reference fatigue testing load levels. Remaining specimens were used for fatigue testing. Quasistatic tests were performed with load the frame in displacement control with a displacement rate of 5mm/min and run to final displacement of 5mm. These test parameters were used to remain consistent with the Renault Group's test parameters and failure criteria.

3.1.4. Fatigue Test Procedure

Cross-tension fatigue tests were performed with the same Instron 8872 load frame as quasistatic tests with specimens in 90° and 45° loading orientations. Fatigue tests were conducted under load control at either 5Hz or 10Hz depending on the specified load levels. Maximum load levels for fatigue testing were obtained at 5% increments starting at 95% of maximum load observed in quasistatic test results until the lowest load level where a specimen achieves runout life of 2,000,000 cycles. The cross-tension fixture has been designed to accommodate Digital Image Correlation (DIC) technology during fatigue testing and is used for crack detection with the GOM-ARAMIS 3D 5M camera system. To remain consistent with Renault Group and quasistatic failure criteria, cyclic tests were run until final displacement of 5mm was traveled for 90° and 45° loading orientations.

3.1.5. Fretting Analysis

Fretting damage examination of SPR joints was performed by obtaining micrographs with scanning electron microscope (SEM) technology and elemental analysis with energy-dispersive X-ray spectroscopy (EDX). The SEM analysis was performed with Zeiss UltraPlus FESEM (with EDX) using 20kV beam, 60 μm spot size, and with all surfaces observed perpendicular to sheets.

3.2. Fatigue Life Prediction

Rupp's model fatigue life prediction method was chosen for this study due ease of use and established use in automotive industry. Although Rupp's model and nCode's adaptation are intended for spot weld joints, some compatibility is documented in literature [30], [31], [32] and further compatibility with wider range of specimen configurations and multi-axial loading is investigated in this document. Rupp's model process starts with a simplified finite element model with experimental specimen geometry, used to extract tractions. This simplified finite element model is created with sheet metal components modelled with linear elastic shell elements and weld nugget modelled by a single beam element. Each beam element end is kinematically coupled to corresponding nodes on both sheets. Beam element length must be an average of both sheet thicknesses so that beam element ends are coincident with midplane of each sheet component. There are no non-linearities such as contact in this simplified finite element model allowing users to apply unit load, eliminating need for multiple finite element models at each load level magnitude. Multiple models are still needed for various specimen geometries, configurations, and boundary conditions. *Figure 14* shows a spot weld joint half model with the nugget modelled as a beam with a circular cross-section.

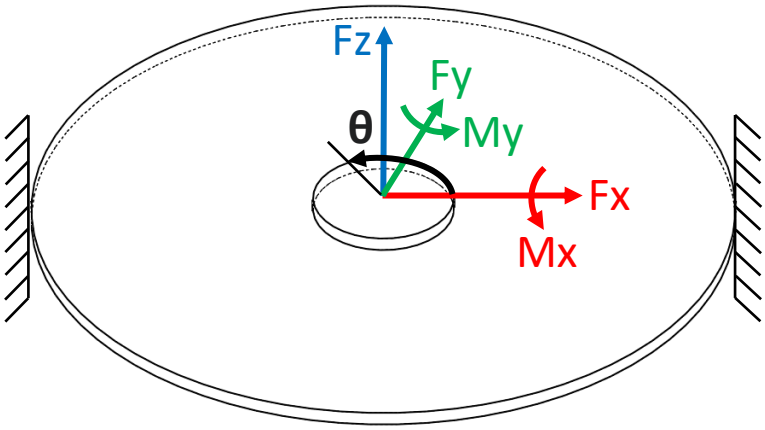

Figure 14: Spot weld half model with annular plate for sheet and circular beam for weld nugget, outer sheet edge fixed.

Post processing starts with obtaining tractions F_x, F_y, F_z, M_x and M_y from the simplified finite element model and substituting them in corresponding local structural stress equations derived from beam, sheet, and plate theory. The following equations (2-4) are equations for determining the structural stresses in the spot weld nugget:

$$\sigma(F_z) = \frac{4F_z}{\pi d^2} \tag{2}$$

$$\sigma\left(M_{x,y}\right) = \frac{32M_{x,y}}{\pi d^3} \tag{3}$$

$$\tau\left(F_{x,y}\right) = \frac{16F_{x,y}}{3\pi d^2} \tag{4}$$

where, d is the nugget diameter. The sheet in *Figure 14* half model is modelled as annular plate with a fixed boundary condition at the outer edge. For both diameter of the cylindrical beam and inside radius of the annulus, spot weld nugget diameter is used. Rupp obtained equations (10-12) by considering the annulus edge restraints shown in *Figure 15* and following the associated structural stress equations (5-9) from work by Young Et al. [44]. If geometry of an annulus with an inside to outside radius ratio of 10:1 is considered and w = unit line load, b = annulus inside radius, a = annulus outside radius, t = sheet thickness and β is a special case tabulated value [44] equations (5) and (8) are calculated to be (7) and (9) respectively.

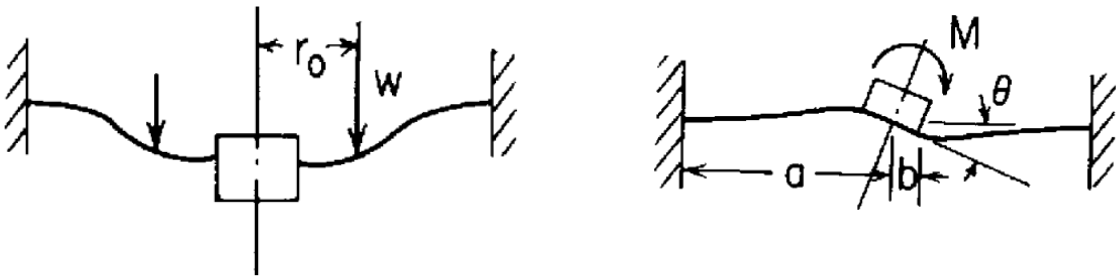

Figure 15: Case 1 f. (left) and Case 21 b. (right) annulus edge restraints [44] *for equations (5-9)*

$$M_{case\ 1f} = \frac{wa\left\{\frac{b}{4a}\left[\left(\frac{b}{a}\right)^2 - 1 + 2\ln\left(\frac{a}{b}\right)\right]\right\}}{\frac{1}{2}\left[1 - \left(\frac{b}{a}\right)^2\right]} \tag{5}$$

$$M_{case\ 1f} = 0.2906F \tag{6}$$

$$\sigma_{case\ 1f} = \frac{6M}{t^2} = \frac{6(0.2906F)}{t^2} = \frac{1.744F}{t^2} \tag{7}$$

$$\sigma_{case\ 21b} = \frac{\beta M}{at^2} \tag{8}$$

$$\sigma_{case\ 21b} = \frac{9.36M}{10bt^2} = \frac{0.936M}{bt^2} \tag{9}$$

Taking Equations (7) and (9) with tractions and coordinate system shown in *Figure 14* equations (10-12) are as follows:

$$\sigma\left(F_{x,y}\right) = \frac{F_{x,y}}{\pi dt} \tag{10}$$

$$\sigma(F_z) = \frac{1.744F_z}{t^2}\ if\ F_z > 0\ otherwise\ \sigma(F_z) = 0 \tag{11}$$

$$\sigma\left(M_{x,y}\right) = \frac{1.872M_{x,y}}{dt^2} \tag{12}$$

and when considering stress equations for membrane and bending a stress factor in the sheets

$$K = 0.6\sqrt{t} \tag{13}$$

has been experimentally determined [5]. If equations (2-4) or (10-12) are used as function of radial angle around weld nugget circumference, sine and cosine functions can approximate stress values at any radial angle along the edge of the weld nugget, allowing for superposition of stresses. Equations (14) and (15) show such superposition stress equations for the nugget and sheet shown in *Figure 14*:

$$\sigma_{nugget} = \left(\frac{4F_z}{\pi d^2}\right) + \left(\frac{32M_x}{\pi d^3}\right)\sin\theta - \left(\frac{32M_y}{\pi d^3}\right)\cos\theta \tag{14}$$

$$\sigma_{sheet} = -\left(\frac{F_x}{\pi dt}\right)\cos\theta - \left(\frac{F_y}{\pi dt}\right)\sin\theta + \frac{1.744F_z}{t^2} + \left(\frac{1.872M_x}{dt^2}\right)\sin\theta - \left(\frac{1.872M_y}{dt^2}\right)\cos\theta \tag{15}$$

Resulting stress values are all in terms of an external unit load applied to the spot-welded specimen or structure and can be multiplied by corresponding load values from experimental fatigue results to convert from load-life curve to stress-life curve. The stress-life plot will have considerable reduction in scatter when compared to the initial load-life plot, resulting in obtaining an adequate master curve from stress-life regression. This master curve is then used to predict joint lives allowing for optimum design of spot-welded structures.

Table 3: nCode empirical factors for steel resistance spot weld joint Rupp's model

Empirical Factors Typical of Steel Spot Welds			
Component	Factor	Diameter Exponent	Thickness Exponent
Fx, Fy	SFFXY = 1.0	DEFXY = 0.0	TEFXY = 0.0
Mx, My	SFMXY = 0.6	DEMXY = 0.0	TEMXY = 0.5
Fz	SFFZ = 0.6	DEFZ = 0.0	TEFZ = 0.5

Table 4: nCode empirical factors for aluminum resistance spot weld joint Rupp's model

Empirical Factors Typical of Aluminum Spot Welds			
Component	Factor	Diameter Exponent	Thickness Exponent
Fx, Fy	SFFXY = 0.4	DEFXY = 0.5	TEFXY = -0.25
Mx, My	SFMXY = 0.4	DEMXY = 0.5	TEMXY = -0.25
Fz	SFFZ = 1.0	DEFZ = 0.0	TEFZ = 1.0

The commercial fatigue and durability assessment software nCode DesignLife has implemented and modified 1995 Rupp's model by including two sets nine experimentally determined empirical factors [6] for steel and aluminum joints to scale sheet structural stresses.

With inclusion of empirical factors, equations (10-12) become equations (16-18) and are substituted into equation (14) to determine the stress state in each sheet component.

$$\sigma\left(F_{x,y}\right) = \frac{F_{x,y}}{\pi dt} \cdot SFFXY \cdot d^{DEFXY} \cdot t^{TEFXY} \tag{16}$$

$$\sigma(F_z) = \frac{1.744F_z}{t^2} \cdot SFFZ \cdot d^{DEFZ} \cdot t^{TEFZ} \; if \; F_z > 0 \; otherwise \; \sigma(F_z) = 0 \tag{17}$$

$$\sigma\left(M_{x,y}\right) = \frac{1.872M_{x,y}}{dt^2} \cdot SFMXY \cdot d^{DEMXY} \cdot t^{TEMXY} \tag{18}$$

3.3. Statistical Optimization

To further optimize the collapse of load-life to stress-life data with Rupp's model for joint fatigue life prediction, statistical optimization can be used. The non-linear GRG method used by Microsoft Excel's Solver add-in is summarized in [34] and documented in [36] is reiterated below. Consider a non-linear programming (NLP) problem:

$$minimize \; f(\boldsymbol{X}) \tag{19}$$

subject to

$$h_j(\boldsymbol{X}) \leq 0, \qquad j = 1,2,\dots,m \tag{20}$$

$$l_k(\boldsymbol{X}) = 0, \qquad k = 1,2,\dots,l \tag{21}$$

$$x_i^{(l)} \leq x_i \leq x_i^{(u)}, \qquad i = 1,2,\dots,n \tag{22}$$

By adding m non-negative slack variables to inequality constraints in equations (19-22) the problem can be rewritten as:

$$minimize \; f(\boldsymbol{X}) \tag{23}$$

subject to

$$h_j(\boldsymbol{X}) + x_{n+j} = 0, \qquad j = 1,2,\dots,m \tag{24}$$

$$h_k(\boldsymbol{X}) = 0, \qquad k = 1,2,\dots,l \tag{25}$$

$$x_i^{(l)} \leq x_i \leq x_i^{(u)}, \qquad i = 1,2,\dots,n \tag{26}$$

$$x_{n+j} \geq 0, \qquad j = 1,2,\dots,m \tag{27}$$

With the total number of variables equal to $n+m$ and the total number of equality constraints equal to $m+l$ in equations (24-27), the problem can be further rewritten as:

$$minimize\ f(\boldsymbol{X}) \tag{28}$$

$$g_j(\boldsymbol{X}) = 0, \qquad j = 1,2,\dots,m+l \tag{29}$$

$$x_i^{(l)} \leq x_i \leq x_i^{(u)}, \qquad i = 1,2,\dots,n+m \tag{30}$$

where $x_i^{(l)}$ and $x_i^{(u)}$ bounds are 0 and infinity respectively. The GRG method eliminates variables using equality constraints where theoretically, a variable can be reduced for each $m+l$ equality constraint. The original $n+m$ variables in $[\boldsymbol{X}]$ can be separated in to two arbitrary sets $[\boldsymbol{Y}]$ and $[\boldsymbol{Z}]$:

$$[\boldsymbol{X}] = \begin{bmatrix}\boldsymbol{Y}\\ \boldsymbol{Z}\end{bmatrix} = [y_1 \quad y_2 \quad \cdots \quad y_{n-l} \quad z_1 \quad z_2 \quad \cdots \quad z_{m+l}]^T \tag{31}$$

where $[\boldsymbol{Y}]$ are the independent variables and $[\boldsymbol{Z}]$ are the dependent variables used to satisfy equation (28). Consider the first variations of the objective function and constraints:

$$df(\boldsymbol{X}) = \sum_{i=1}^{n-l} \frac{\partial f}{\partial y_i} dy_i + \sum_{i=1}^{m+l} \frac{\partial f}{\partial z_i} dz_i \tag{32}$$

$$dg_i(\boldsymbol{X}) = \sum_{j=1}^{n-l} \frac{\partial g_i}{\partial y_j} dy_j + \sum_{j=1}^{m+l} \frac{\partial g_i}{\partial z_j} dz_j \tag{33}$$

or in matrix form:

$$df(\boldsymbol{X}) = \nabla_{\boldsymbol{Y}}^T f d\boldsymbol{Y} + \nabla_{\boldsymbol{Z}}^T f d\boldsymbol{Z} \tag{34}$$

$$d\boldsymbol{g} = [C]d\boldsymbol{Y} + [D]d\boldsymbol{Z} \tag{35}$$

Assuming the GRG method starts at a feasible point leading to $g(\boldsymbol{X}) = 0$ and assuming maintaining feasibility at $\boldsymbol{X} + d\boldsymbol{X}$ leads to $d\boldsymbol{g} = 0$ then equation (35) can be rearranged for:

$$d\boldsymbol{Z} = -[D]^{-1}[C]d\boldsymbol{Y} \tag{36}$$

Substituting equation (36) into equation (34) yields:

$$df(\boldsymbol{X}) = \left(\nabla_{\boldsymbol{Y}}^{T} f - \nabla_{\boldsymbol{Z}}^{T}[D]^{-1}[C]\right) d\boldsymbol{Y} = \mathbf{G}_{R}^{T} d\boldsymbol{Y} \tag{37}$$

where $\mathbf{G}_{\boldsymbol{R}}$ is the generalized reduced gradient and provides search direction. Then various NLP elimination or interpolation minimization methods can be applied to iteratively solve until $\mathbf{G}_{\boldsymbol{R}} \leq \boldsymbol{\varepsilon}$ where $\boldsymbol{\varepsilon}$ is a small convergence number.

3.4. Summary of nCode Rupp's model Steps

This section summarizes and lists the steps of obtaining a stress-life curve to predict the life of spot weld joints with nCode's adaptation of Rupp's model.

1. Create Finite element model with unit load with sheet components modelled with shell elements and the weld nugget modelled with a single beam element.
2. Extract forces and moments from finite element model.
3. Substitute extracted forces and moments to structural stress equations.
4. Scale unit stress to fatigue load levels from experimental data.
5. Plot stress-life.
6. Perform statistical optimization to obtain master curve.

3.5. Finite Element Modelling

Finite element method has been used for 3 purposes in this overall study: validation of cross-tension sheet metal joint test fixture described in Section 3.1.2, modelling simplified sheet metal joints for Rupp's model fatigue life prediction method in Section 4.1 and Section 6, and detailed SPR joint modelling in Section 7. The commercial finite element software Abaqus/CAE 2019 has been used in all finite element modelling instances in this document with model details documented in their respective sections.

4. Uniaxially Loaded SPR Compatibility with nCode Rupp's Model

To begin SPR fatigue life prediction compatibility with Rupp's model for RSW investigation, aluminum SPR experimental fatigue data was collected from [13], [21], [22], [24] and processed to observe results. Chosen literature results were selected on availability of information needed to perform Rupp's model which are specimen geometry details, boundary conditions, loading, material properties and experimental fatigue load-life results.

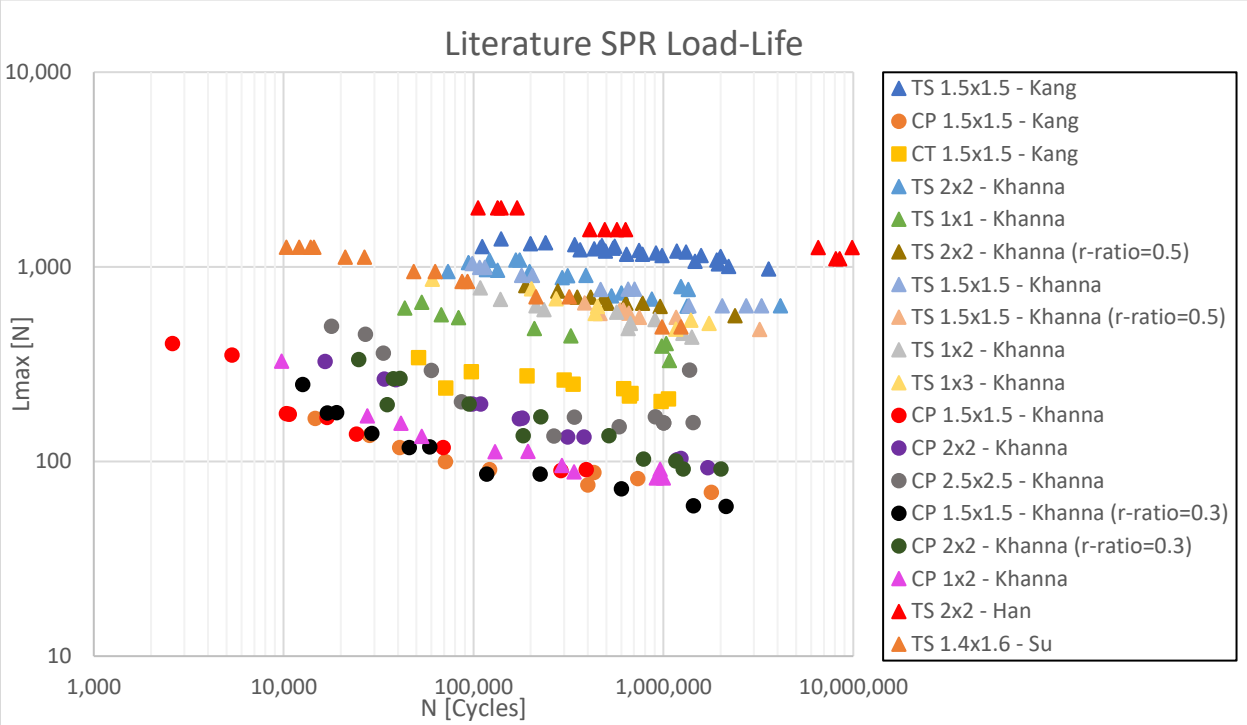

Figure 16: SPR load-life plot with experimental fatigue life results collected from literature with tensile-shear (TS), coach-peel (CP) and cross-tension (CT) configurations [13], [21], [22], [24]

This collection of 218 aluminum SPR fatigue tests and their results consisting of 130 tensile-shear, 77 coach-peel and 11 cross-tension specimens of varying aluminum alloy, sheet thicknesses and thickness combinations, and load ratios provides wide range of specimens and process parameters contributing to the scatter in *Figure 16*, which is desired for studying Rupp's model performance and compatibility with SPR joints. *Figure 16* shows that greatest cause of high scatter is specimen configuration where a distinct pool of data exists for both the tensile-shear and coach-peel configurations. *Table 5* shows specimen sheet materials consist of 5000 and 6000 series aluminum alloys with thicknesses ranging from 1mm to 3mm, SPR diameters ranging from 4.5mm to 6mm, and load levels ranging from 0.1 to 0.5. An undesirable variable is inconsistency in definition of final life found in each of the four studies. Kang et al. [22] states the final life to be complete joint separation, Su et al. [13] defines final separation as 5mm displacement,

Han et al. [24] defines as fracture and Khanna et al. [21] defines as visible failure. Although this discrepancy exists, compatibility studies can still be performed since life differences are negligible as 5mm displacement, fracture or visible damage life will be close to complete separation life.

Table 5: SPR experimental and specimen details collected from literature

Author	Specimen Configuration	Sheet Material	Sheet Young's Modulus [MPa]	Pierced Sheet Thickness [mm]	Clenched Sheet Thickness [mm]	SPR Diameter [mm]	r-ratio	Quantity
Kang	Tensile-Shear	5052	78,300	1.5	1.5	5	0.1	26
	Coach-Peel			1.5	1.5		0.1	9
	Cross-Tension			1.5	1.5		0.1	11
Khanna	Tensile-Shear	6111	80,700	1	1	6	0.1	9
				1.5	1.5		0.1	12
				1.5	1.5		0.5	8
				2	2		0.1	18
				2	2		0.5	11
				1	2		0.1	10
				1	3		0.1	8
	Coach-Peel			1.5	1.5		0.1	9
				1.5	1.5		0.3	11
				2	2		0.1	12
				2	2		0.3	12
				2.5	2.5		0.1	13
				1	2		0.1	11
Han	Tensile-Shear	5754	Unspecified	2	2	4.5	0.167	2
				2	2		0.125	2
				2	2		0.111	4
				2	2		0.139	4
				2	2		0.185	2
Su	Tensile-Shear	6111	Unspecified	1.4	1.6	5.72	0.1	14

4.1.nCode Rupp's Model Pre-Processing

To complete the first step of Rupp's model, simplified finite element models were created for each specimen configuration in ABAQUS with sheets modelled with linear elastic S4R elements and SPR modelled with a single B31 element. Sheet geometries for all data sets were modeled to exact size in length, width, and thickness, and were coarsely meshed for approximate shell element size of 5mm by 5mm. Since the simplified model is entirely linear elastic with the sole purpose of extracting tractions, a relatively fine mesh

is counterproductive by causing undesired compliance. Young's Modulus values in Table 5 are provided by Kang et al. [22] and Khanna et al. [21] and extrapolated for Su et al. [13] since same material 6111 is used. For 5754 aluminum alloy used in Han et al. [24] a Young's Modulus of 70 GPa and 80 GPa were compared and resulted in no difference up to 4 decimal places in traction results of *Table 6*. This shows that Rupp's model is not sensitive to relatively high Young's Modulus values from [21] and [22], where the latter was experimentally determined. For all specimen configurations the beam element length is average thickness of both sheets, each beam element end is kinematically coupled in all degrees of freedom to either sheet, and orientated perpendicular to both sheets. The beam element cross-sectional area is circular and calculated from the diameters found in *Table 5* and should have a stiffness value high enough so that overall joint stiffness is not sensitive to beam compliance. Bonnen et al. [45] suggests a completely rigid beam element while Rupp et al. [5] simply suggests using high stiffness and nCode DesignLlife Theory Guide [6] suggests stiffness achieved by common steel Young's Modulus values are sufficient. For this study Young's Modulus value of 200 GPa is used for modelling the beam element stiffness.

Each finite element model has been orientated in the global coordinate system so that the z-direction is axial to the tubular geometry of SPR itself. The use of linear elastic elements and with exclusion of contact in these simplified models allow users to apply unit load, so that only a single finite element model per specimen geometry is required. This allows any set of test results for the same specimen geometry to be scaled with varying load levels during post processing, significantly increasing ease of use of this fatigue life prediction method. Each specimen configuration has been modelled to reflect the same boundary conditions that have been applied during experimental process of determining fatigue life.

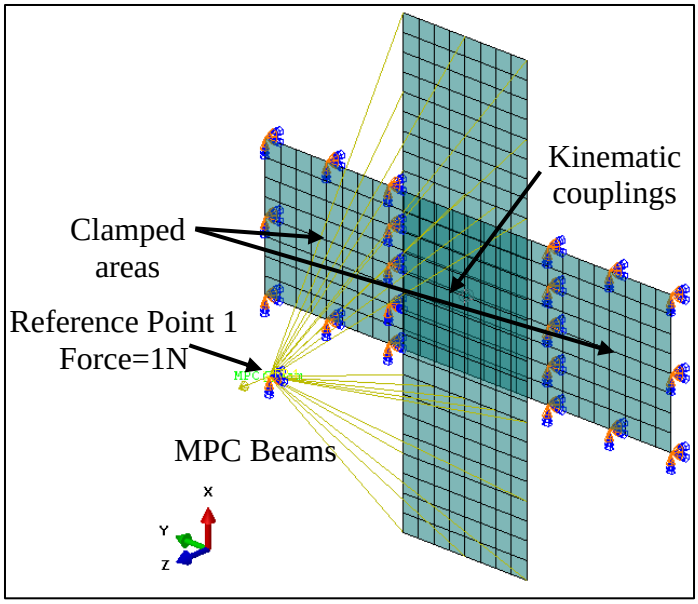

Figure 17: Simplified finite element model of cross-tension SPR joint in pure tension loading

The finite element models with cross-tension configuration have left and right ends of one sheet fixed in all degrees of freedom to simulate specimen fixture clamping during experimental process. The other sheet has the same two end areas connected to a reference point with beam type multi-point constraints. This arbitrarily located reference point will be constrained in all rotational degrees of freedom and two linear degrees of freedom which depend on and allow desired loading of the cross-tension specimen to be modelled. *Figure 17* provides an example where the applied load is in positive z direction meaning that the linear displacement in the respective direction must be free, resulting in x and y linear degrees of freedom to be fixed.

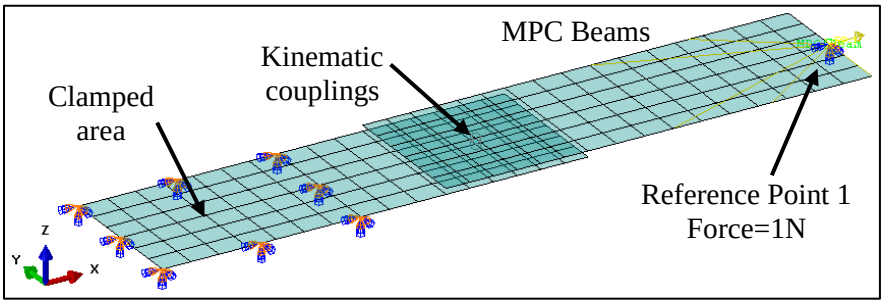

Figure 18: Simplified finite element model of tensile-shear configuration SPR joint with load in x-direction

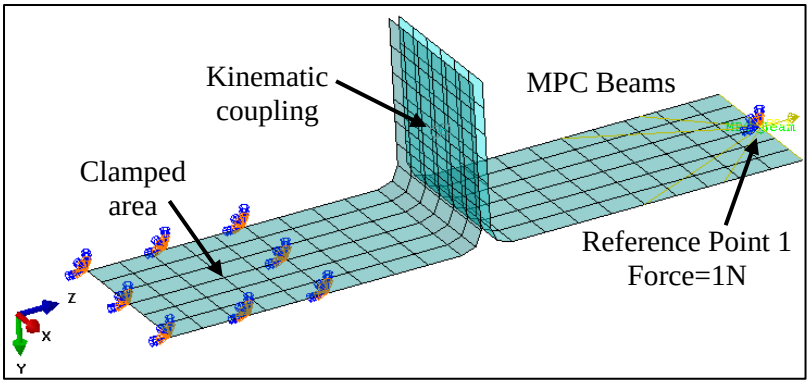

Figure 19: Simplified finite element model of coach-peel configuration SPR joint with load in z-direction

The modeling techniques used in the cross-tension finite element model were applied to tensile-shear and coach-peel configurations. These two specimen configurations only require one sheet end to be constrained in all degrees of freedom to simulate specimen fixture clamping. The reference point is connected to the opposite clamped area with beam type multi-point constraints as shown in *Figure 18* and *Figure 19*. For all coach-peel simplified models, neutral bend line radii were used. Since tensile-shear and coach-peel configurations only provide meaningful durability results in uniaxial loading orientations, loads will always be applied so that tensile-shear specimens will cause two sheets to slide apart, and coach-peel specimens will cause joined sheet tabs to pry apart.

4.2.nCode Rupp's Model Post-Processing

Post processing begins with extracting tractions from completed finite element simulations. Required values for Rupp's model are F_x, F_y, F_z, M_x and M_y according to *Figure 14* and *Figure 20*, and are obtained by extracting nodal forces and moments at each beam element end with ABAQUS NFORC1, NFORC2, NFORC3, NFORC4, and NFORC5 field outputs respectively. Coordinate transformations may be needed during traction extraction depending on coordinate system differences between finite element model and Rupp's model convention and may be unnecessary if F_z is consistent. All extracted traction values from the literature collection of results are shown in *Table 6* along with the geometrical properties sheet thickness and SPR diameters, which are required for structural stress calculations. Structural stress calculations are only required for one sheet if the specimen consists of two sheets with the same thickness and material due to symmetry. For dissimilar thickness, dissimilar material or combination of both, structural stresses are still only calculated for the sheet which has failed during testing, as life corresponds to the failed sheet damage.

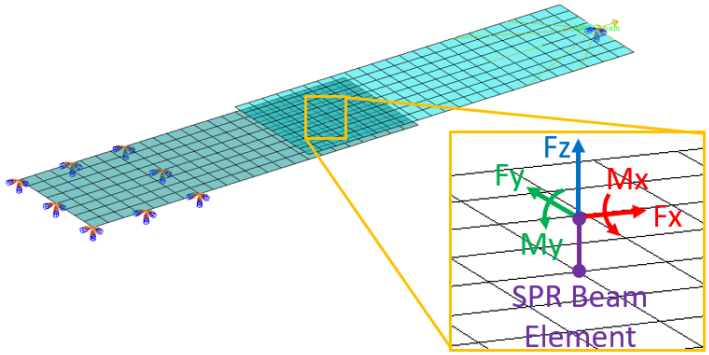

Figure 20: Detail view of bottom sheet and beam element with tractions at beam end (top sheet hidden)

With values from *Table 6*, equations (15-17) and empirical factors typical of aluminum spot welds from *Table 4*, unit structural stresses in *Table 7* are calculated. Since simplified finite element models contained no non-linearities, unit structural stresses can be directly scaled by multiplying by their corresponding load level values from experimental data and plotted. *Figure 21* contains the literature SPR fatigue results after load-life to stress-life conversion and clearly shows a considerable reduction in scatter when compared to the load-life plot in *Figure 16*. The result of applying spot weld life prediction model introduced by Rupp et al. and modified by nCode with empirical factors typical of aluminum spot welds, has resulted in significant collapse of SPR fatigue data.

Table 6: Specimen material, geometries, and extracted unit traction values for experimental fatigue results collected from literature

Specimen Configuration	Sheet Material	t1 [mm]	t2 [mm]	Diameter [mm]	Load [N]	Fx [N]	Fy [N]	Fz [N]	Mx [Nmm]	My [Nmm]
Tensile-Shear	5052	1.5	1.5	5	1	1	0	0.0226	0	0.7500
	6111	1	1	6	1	1	0	0.0274	0	0.5000
	6111	1.5	1.5	6	1	1	0	0.0410	0	0.7500
	6111	2	2	6	1	1	0	0.0546	0	1.000
	6111	1	2	6	1	1	0	0.0246	0	0.3618
	6111	1	3	6	1	1	0	0.0148	0	0.2127
	5754	2	2	4.5	1	1	0	0.0271	0	1.000
	6111	1.4	1.6	5.72	1	1	0	0.0176	0	0.6959
Coach-Peel	5052	1.5	1.5	5	1	0	0	1	-11.84	0
	6111	1.5	1.5	6	1	0	0	1	-7.706	0
	6111	2	2	6	1	0	0	1	-7.614	0
	6111	2.5	2.5	6	1	0	0	1	-7.568	0
	6111	1	2	6	1	0	0	1	-7.590	0
Cross-Tension	5052	1.5	1.5	5	1	0	0	1	0	0

Table 7: Unit stress values calculated from tractions in Table 6

Specimen Configuration	Sheet Material	σ(fx) [MPa]	σ(fy) [MPa]	σ(fz) [MPa]	σ(mx) [MPa]	σ(my) [MPa]	θ	σsheet [MPa]
Tensile-Shear	5052	0.0343	0	0.0263	0	0.1009	180	0.1615
	6111	0.0520	0	0.0478	0	0.1528	180	0.2526
	6111	0.0313	0	0.0477	0	0.0921	180	0.1711
	6111	0.0219	0	0.0476	0	0.0643	180	0.1337
	6111	0.0520	0	0.0428	0	0.1106	180	0.2054
	6111	0.0520	0	0.0257	0	0.0650	180	0.1427
	5754	0.0252	0	0.0237	0	0.0742	180	0.1231
	6111	0.0350	0	0.0220	0	0.1022	180	0.1591
Coach-Peel	5052	0	0	1.163	-1.592	0	270	2.755
	6111	0	0	1.163	-0.946	0	270	2.109
	6111	0	0	0.872	-0.489	0	270	1.361
	6111	0	0	0.698	-0.294	0	270	0.992
	6111	0	0	1.744	-2.320	0	270	4.064
Cross-Tension	5052	0	0	1.163	0	0	0	1.163

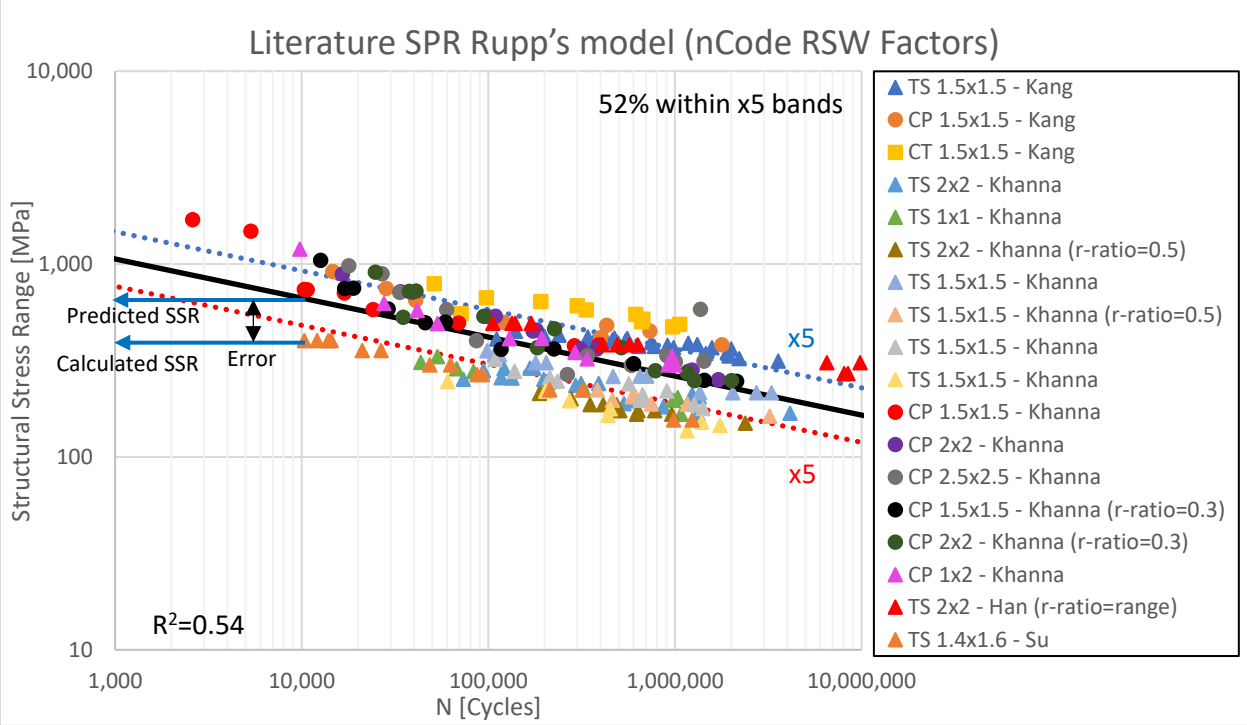

Figure 21: SPR stress-life plot transferred from load-life with experimental fatigue life results collected from literature, difference between predicted and calculated structural stress range labeled for a single tensile-shear data point (r-ratio = 0.1 unless otherwise specified)

Collapse in *Figure 21* can be further improved with statistical optimization described in Section 3.3 by using nine empirical factors in equations (15-17). The objective of optimization is to maximize the coefficient of determination or R^2, a value ranging from 0 to 1 where a R^2 value of 1 indicates no error in any data point and regression yields a statistical model with perfect fitting. Equations (38-40) show that total sum of squares is constant for a given set of data and to maximize the R^2 value, sum of squared residuals must be minimized. The sum of squared residuals is a value that is the sum of all deviations from the actual to predicted values squared, one of which can be seen in *Figure 21* where a tensile-shear specimen has a structural stress range of 401 MPa with a predicted structural stress range 642 MPa. Equation (38) therefore becomes the objective function for the non-linear generalized reduced gradient method and is a function of structural stress for each 218 data points in *Figure 21*. Each structural stress term in the objective function includes an empirical factor from *Table 4* which are used as variables which can be altered within specified bounds to achieve optimization. The non-linear generalized reduced gradient solver available in commercial software Microsoft Excel is used in this study where empirical factors have upper and lower bounds of +/-1 and when convergence is met when iteration of the generalized reduced gradient becomes less than 0.0001.

$$Sum\ of\ Squared\ Residuals = SS_R = \sum (y_i - \hat{y}_i)^2 \tag{38}$$

$$Total\ Sum\ of\ Squares = SS_T = \sum (y_i - \bar{y}_i)^2 \tag{39}$$

$$R^2 = 1 - \frac{Sum\ of\ Squared\ Residuals}{Total\ Sum\ of\ Squares} = \frac{SS_R}{SS_T} \tag{40}$$

Figure 22 shows results of non-linear generalized reduced gradient optimization for SPR fatigue results collected from literature where the R^2 value from pre-optimization stress-life plot has increased from 0.54 to 0.59 showing slight improvement. Another method to assess the collapse performance is the change in percentage of values included in the scatter bands as seen in *Figure 21* and *Figure 22*, where the percentage of data within the domain of +/- x5 increases from 52% to 70%. Newly optimized empirical factors generated by non-linear generalized reduced gradient optimization process accommodate any sheet thickness, SPR diameter and stress effects and are shown in *Table 8*. The initial nCode aluminum and optimized SPR values for TEFXY and TEMXY are both negative exponents, indicating that unmodified Rupp's structural stress equations (10) and (12) over-predict stresses when compared to steel RSW. Any positive or negative optimized exponent empirical factor near a value of 0 indicates Rupp's model structural stress equations require minimal scaling.

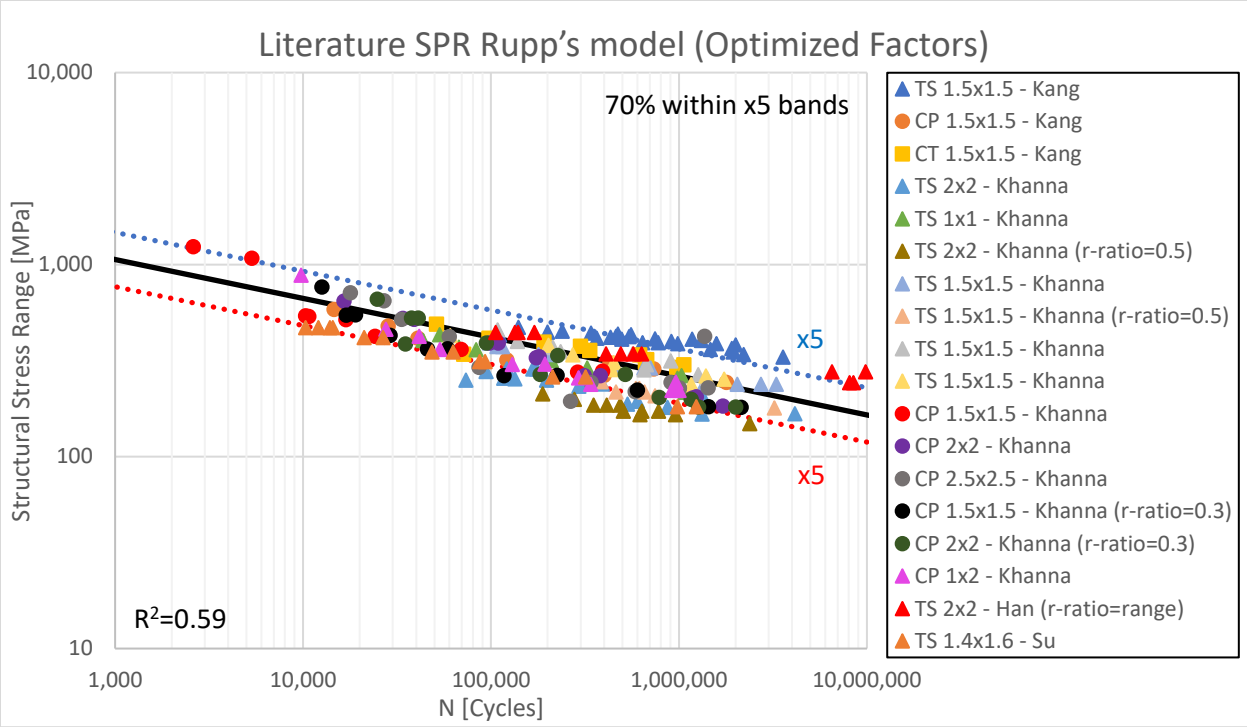

Figure 22: SPR stress-life plot post non-linear generalized reduced gradient data collapse

Overall results of this study show use of Rupp's model and statistical optimization to predict fatigue life of uniaxially loaded SPR sheet metal joints yield good results and are compatible. high reduction in scatter has been achieved from transferring load-life SPR fatigue results from literature to stress-life with the method introduced by Rupp et al. and updated by nCode. Further optimization of stress-life data can be achieved with an optimization method such as the non-linear generalized reduced gradient although with less effectiveness.

Table 8: Original nCode suggested aluminum RSW empirical factors and non-linear generalized reduced gradient optimized empirical factors

	SFFXY	DEFXY	TEFXY	SFMXY	DEMXY	TEMXY	SFFZ	DEFZ	TEFZ
nCode suggested aluminum RSW factors	0.4	0.5	-0.25	0.4	0.5	-0.25	1	0	1
Literature SPR factors	0.57	1	-0.79	0.12	1	-0.31	0.12	1	1

5. Quasistatic and Cyclic Experimental Results

While Section 4 shows promising results when applying Rupp's model to SPR fatigue life prediction, experimentation was performed by different institutions with different procedures and research goals in mind, where process parameters, manufacturing processes, and materials were varying. Cross-tension SPR specimens have been tested in 0°, 45° and 90° orientations by automotive manufacturer Renault Group who have shared their experimental results. A test fixture at the University of Waterloo was used perform quasistatic and fatigue testing of cross-tension sheet metal joints with same geometry and loading orientations as Renault Group. These results generated data to observe performance of Rupp's model when applied to fatigue life prediction of SPR in a more controlled environment, well-established process parameters and under multiaxial loading.

5.1. Quasistatic Experimental Results

The following subsections document results of quasistatic testing including load-displacement responses, failure modes and damage details. *Table 2* tabulates quasistatic testing completed at the University of Waterloo where a total of 6 quasistatic tests were completed for Al 6016 2mm by 1mm and 3 for Al 6016 1mm by DX54D 0.95mm joints.

5.1.1. Quasistatic Al 6016 2mm by 1mm

For Al 6016 2mm by 1mm cross-tension specimens, all 6 quasistatic specimens failed at the protrusion of the 1mm bottom clinched sheet as shown in *Figure 23 (right)* and *Figure 24 (right)*. The SPR head and 2mm pierced sheet show no signs of displacement, deformation or damage as seen in *Figure 23 (left)* and *Figure 24 (left)*. For 90° loaded specimens, contact surfaces of the two sheets have remained mostly coincident while the clenched sheet has displaced axially in the controlled direction with visible damage. Slight out of plane deformation is visible in *Figure 23 (right)* at the top edge of the clenched sheet. Significant out of plane deformation of the clenched sheet is visible in *Figure 24 (right)* due to bending caused by the normal load component from the 45° loading orientation. Mechanical interlock still provides enough friction to prevent sheets from moving relative to each other in all specimens.

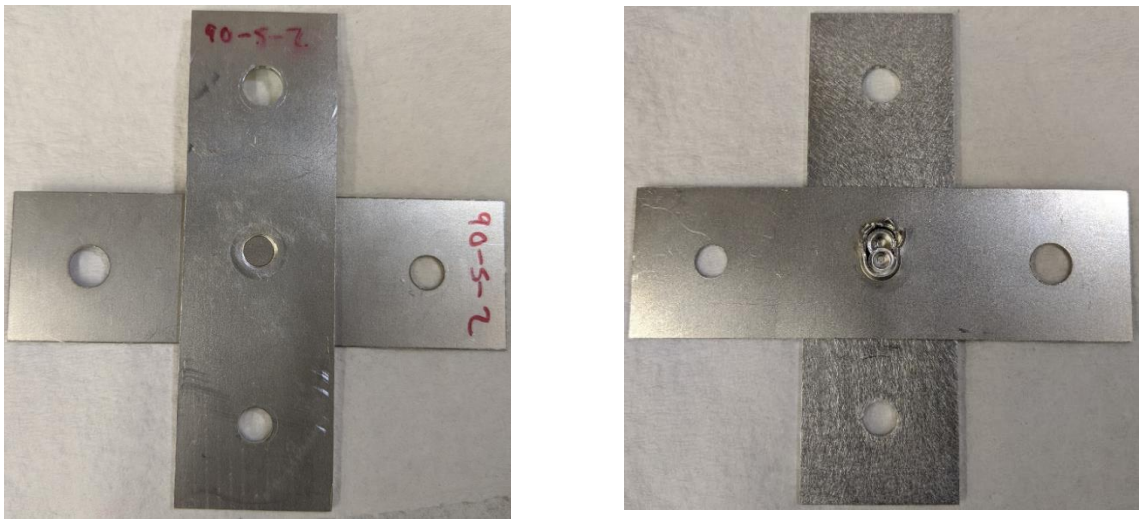

Figure 23: Al 6016 2mm by 1mm SPR cross-tension post quasistatic test 90° test pierced 2mm sheet (left) and clenched 1mm sheet (right)

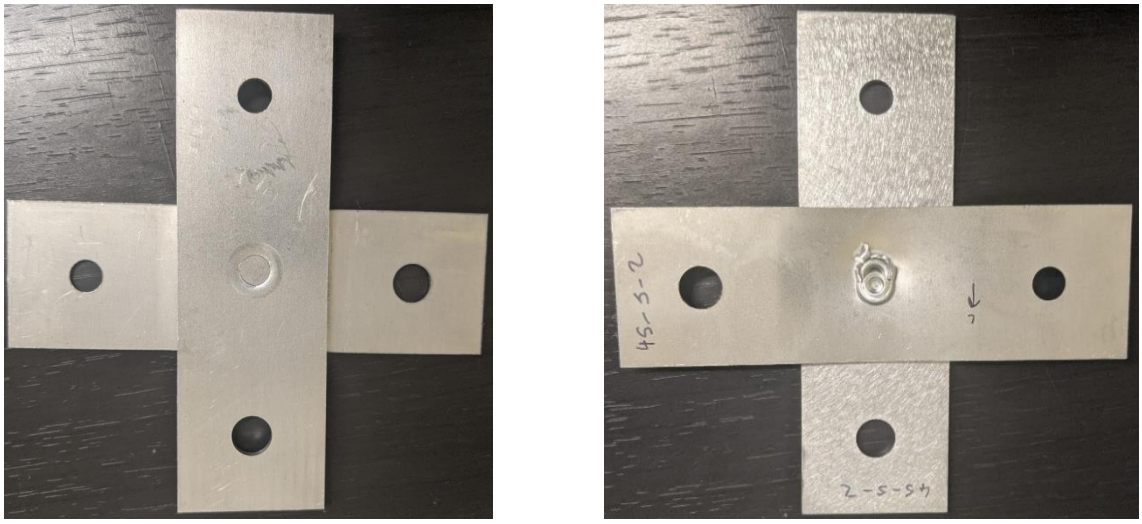

Figure 24: Al 6016 2mm by 1mm SPR cross-tension post quasistatic test 45° test pierced 2mm sheet (left) and clenched 1mm sheet (right)

Load responses from all 3 90° quasistatic test results in *Figure 25 (left)* have similar profiles where load sharply rises to approximately 2,600N and begins to plateau at onset of yielding. Load then drops after initial rupture where the SPR breaks through the protrusion of the bottom clinched sheet. After the protrusion sustains enough damage to the point where no structural support is provided, the SPR continues to displace causing damage by tearing clenched sheet unformed areas as seen in *Figure 24 (right)*. This behaviour can also be seen from load response in *Figure 25 (left)* where from approximately 1.3mm-1.8mm to 5mm displacement, significant load still exists.

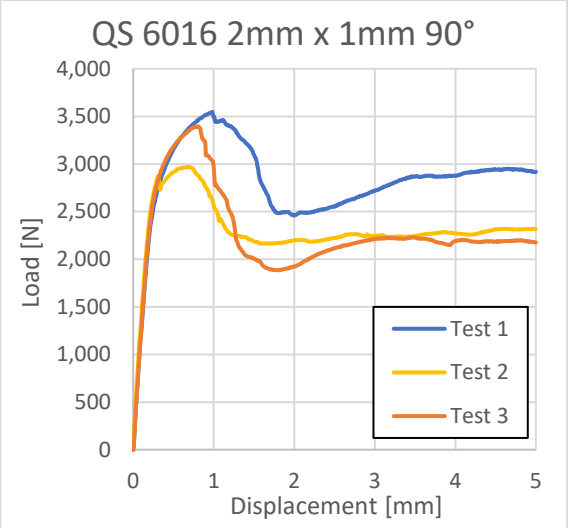

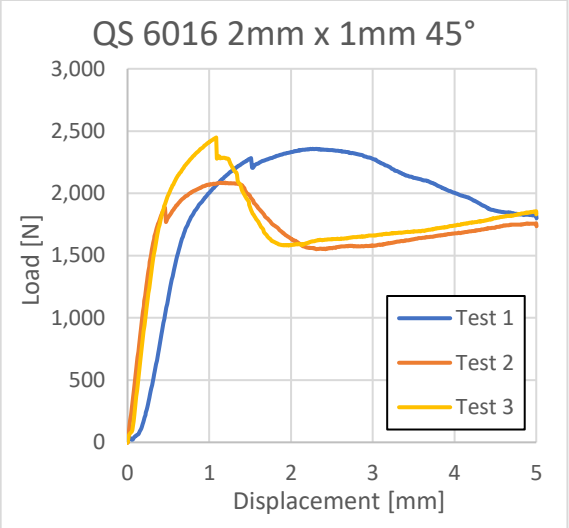

Figure 25: Al 6016 2mm by 1mm SPR cross-tension load-displacement curves for 90° (left) and 45° (right) loading orientations

Combined loading at 45° test 2 and test 3 in *Figure 25 (right)* behave similarly to quasistatic tests at 90° at lower range of loads. *Figure 26 (center)* and *(right)* shows similar failure mode and damage occurring in clenched sheets of 45° test 2 and test 3 when compared to 90° specimens. Test 1 in *Figure 25 (right)* shows different behaviour where load response rises in magnitude after a small displacement of approximately 0.2mm occurs whereas rise in load is immediate in test 2 and test 3. Onset of yielding in test 1 occurs at the same load of 1,700N when compared to test 2 and test 3 although a different response in plastic regime is observed where load reaches its peak at further displacement of about 1mm more than test 2 and test 3. Load response after peak has much gradual drop and reaches same level of test 2 and test 3 around 5mm. Visible differences in damage is observed when comparing test 1 damage shown in *Figure 26 (a)* to test 2 and test 3 damage shown in *Figure 26 (b)* and *Figure 26 (c)* respectively. This difference in damage correlates to differences in load response seen in *Figure 25 (right)*. Sheet protrusions in test 2 and test 3 show several rupture points along the bottom radius that supports SPR during loading. Ruptured fragments are still attached to the sheet and have been severely deformed to fold over, providing minimal or no structural support to the overall joint. The ruptures themselves create a sharp discontinuity along the direction of loading in the sheet structure causing lower load response during displacement. The sheet protrusion in test 1 *Figure 26 (a)* shows less damage and has remained more intact with less rupture points, less deformation and remains less fragmented than test 2 and test 3 *Figure 26 (b)* and *(c)*. Unformed areas of the clenched sheet just before ruptured areas in test 2 and test 3 has minimal damage whereas unformed areas of the clenched sheet have visible out of plane deformation due to compressive loading seen in *Figure 26 (a)*. Although out of plane deformation is visible, no rupture has occurred in this area which contributes

to the additional strength of the overall joint. All 3 45° tests have a small sudden drop in load that occurs just before force plateau of test 1, at onset of yielding in test 2 and at the plateau in test 3.

Figure 26: Al 6016 2mm by 1mm SPR cross-tension post quasistatic test 45° clenched sheet (a) damage test 1 (b) test 2 (c) test 3

5.1.2. Quasistatic Al 6016 1mm by DX54D 0.95mm

A total of 3 quasistatic tests were completed with Al 6016 1mm by DX54D 0.95mm specimens with 2 specimens completed at 90° and 1 specimen completed at 45°. Both sheets in 90° specimens have deformation where mechanical interlock between both sheets and SPR have been compromised. The clenched bottom DX54D sheet has displaced axially in the loading direction and SPR itself has visible angular displacement. Unformed areas of both pierced and clenched sheets have deformed out of plane in either direction depending on SPR direction of rotation as shown in *Figure 27*. Contact areas of the two sheets have slightly separated with the bottom edge of the clenched sheet still contact with the pierced sheet. The sheets are still held together by SPR mechanical interlock with no play.

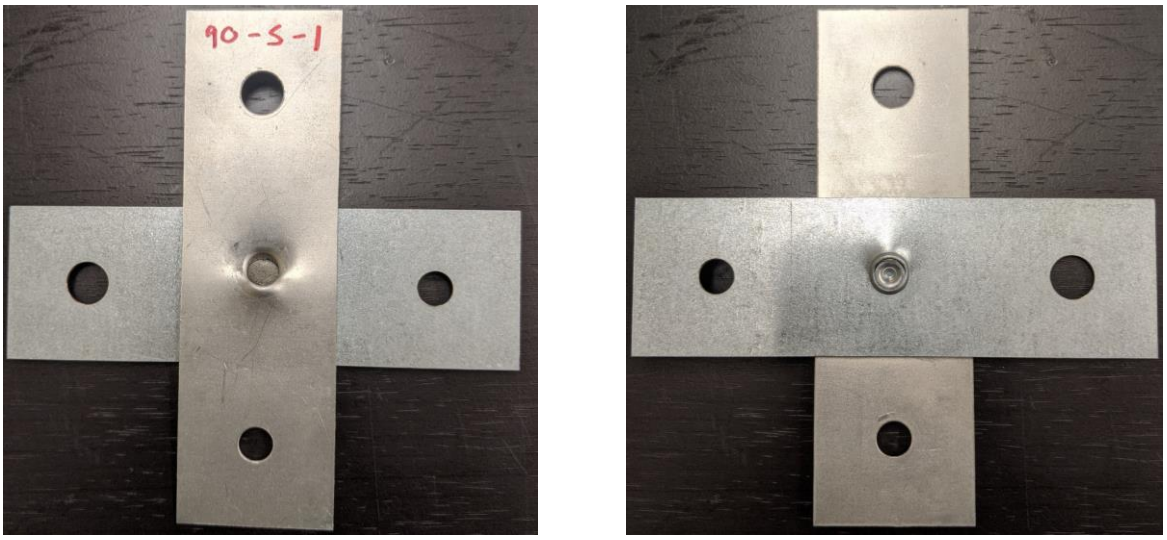

Figure 27: Al 6016 1mm by DX54D 0.95mm SPR cross-tension post quasistatic test 90° pierced Al 6016 sheet (left) and clenched DX54D sheet (right)

Deformation response of 45° quasistatic specimens is like 90° specimens where similar rotation of SPR and associated deformation in the sheet occurs. Due to the normal component of applied load, 45° specimen's top and clenched sheets have additional deformation due to bending. Significant separation between top and clenched sheets has occurred with no contact between unformed areas of the joint. The sheets are minimally held together by mechanical interlock of damaged sheets. The SPR remains partially embedded in the bottom steel sheet and pierced sheet damage causes significant play in the joint.

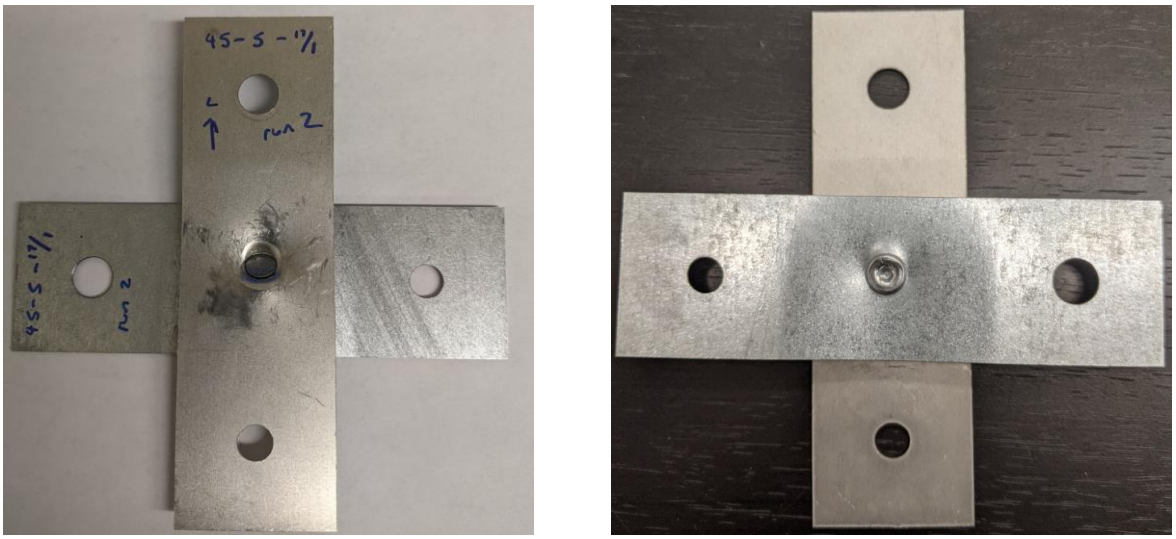

Figure 28: Al 6016 1mm by DX54D 0.95mm SPR cross-tension post quasistatic test 45° pierced Al 6016 sheet (left) and clenched DX54D sheet (right)

Joint details shown in *Figure 29 (left)* and *Figure 30 (left)* show pierced sheet material damage due to SPR angular displacement. The same SPR angular displacement has caused a crack tangent to the SPR diameter on the clenched sheet top side in 90° specimens exposing the SPR's flared base *Figure 29 (right)*. This crack occurs at the outermost radius of the clenched sheet protrusion. Small radial cracks have developed along the top edge of this tangential crack as SPR rotation pushes this top edge out of plane.

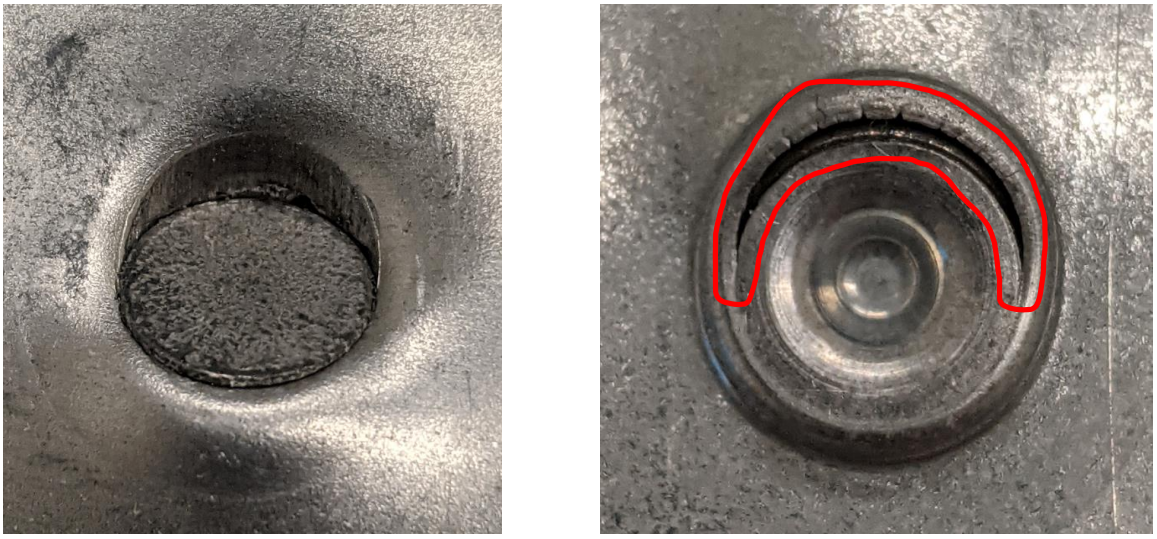

Figure 29: Al 6016 1mm by DX54D 0.95mm SPR cross-tension post quasistatic test 90° pierced Al 6016 sheet (left) and clenched DX54D sheet (right) SPR local damage details

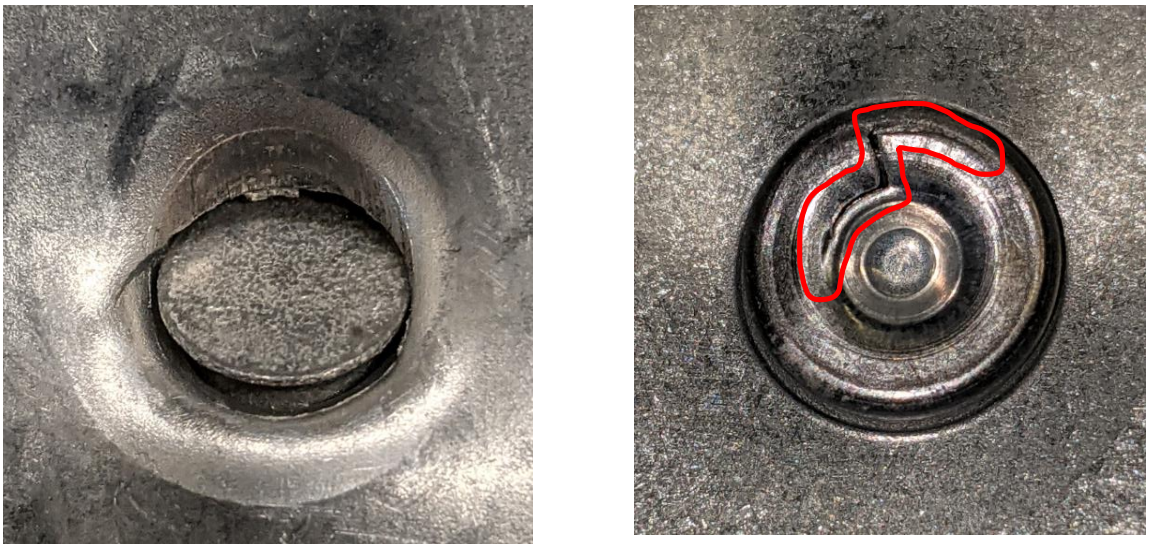

Figure 30: Al 6016 1mm by DX54D 0.95mm SPR cross-tension post quasistatic test 45° pierced Al 6016 sheet (left) and clenched DX54D sheet (right) SPR local damage details

Figure 30 (left) shows a crack on the left side of surface damage discontinuity in the pierced sheet. *Figure 30 (right)* shows clenched sheet damage where a crack changes path from being tangent to the SPR at the outermost radius of the formed protrusion, then to radial, and then back to tangent at the formed protrusion's inside radius.

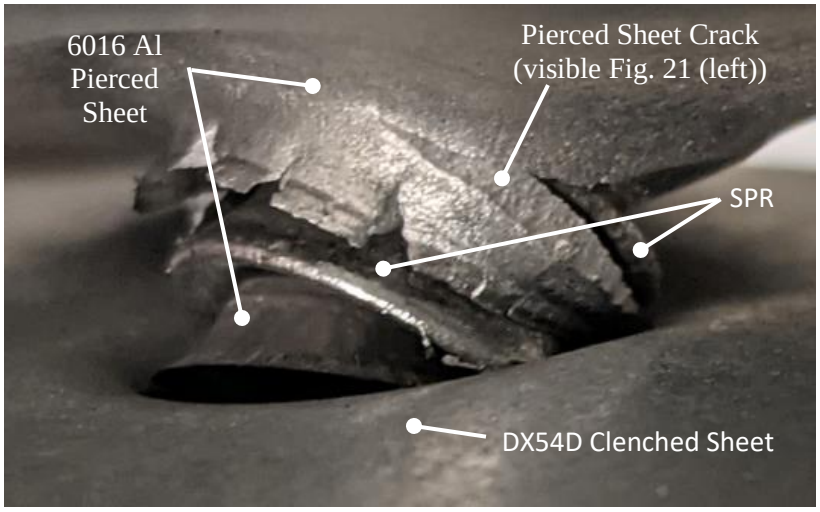

Figure 31: Al 6016 1mm by DX54D 0.95mm SPR cross-tension post quasistatic test 45° partially separated joint details

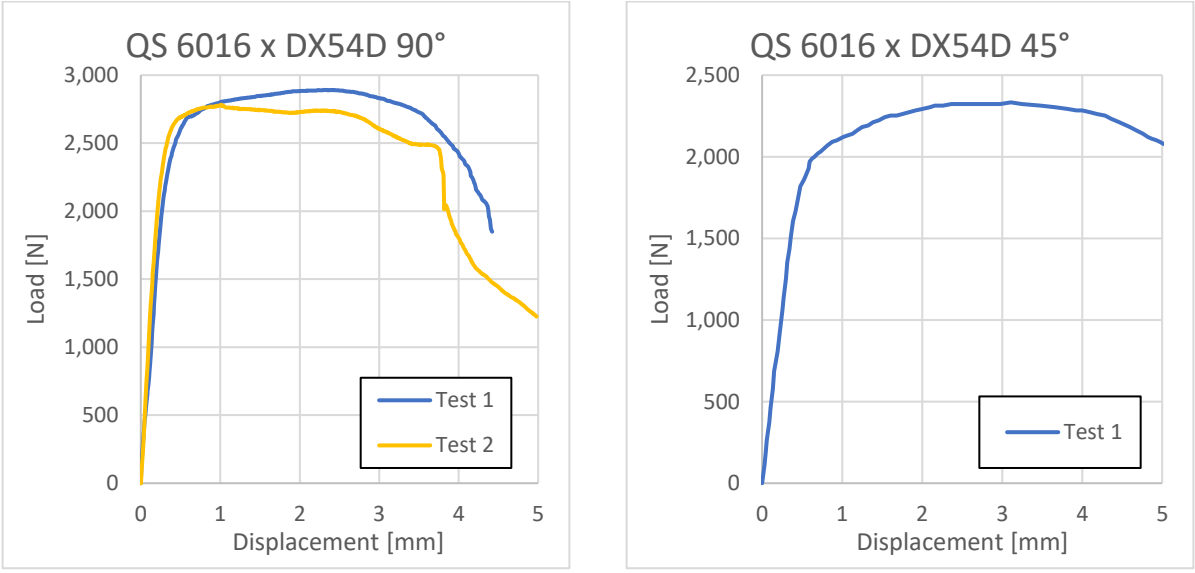

Figure 32: 6016 1mm by DX54D 0.95mm SPR cross-tension load-displacement curves for 90° (left) and 45° (right) loading orientations

Due to significant separation sheets in 45° quasistatic specimens, one can see post test state of the joint. *Figure 31* shows full separation of sheet surfaces and angular displacement of SPR to cause itself to partially

uproot from the clenched sheet. The pierced sheet captive inner portion formed during SPR process is now visible and moves freely. The pierced sheet is punctured by SPR top edge and causes a tangential crack seen in *Figure 30 (left)* and *Figure 31* to propagate due to out of plane shear. Large and small radial cracks also appear at the outermost flared edge of the pierced sheet. Test 1 and Test 2 90° quasistatic specimens visually have same deformation responses and sheet damage although *Figure 32* shows difference in smoothness after joint yielding. Test 1 45° quasistatic specimen has similar load-displacement curve profile to 90° Test 1; however, has overall lower load magnitude.

5.2. Fatigue Experimental Results

The following subsections document results of fatigue testing including load-life plots, stiffness response curves, failure modes and damage details. *Table 2* tabulates the fatigue testing completed at the University of Waterloo where a total of 55 fatigue tests were completed for Al 6016 2mm by 1mm and 10 for Al 6016 1mm by DX54D 0.95mm joints.

5.2.1. Fatigue Al Al 6016 2mm by 1mm

Load levels used for fatigue testing are shown in *Table 9* where 8 load levels with 3 replications were performed for 90° cross-tension until runout was achieved at load level where maximum load is 60% of peak quasistatic load. At 95%, 90% and 85% load levels, 5 specimens were excluded in *Figure 33* due to first cycle failure with identical failure modes observed in quasistatic test results. For 45° only two replications were performed at 95% since both tests at 95% load level failed with identical failure modes observed in quasistatic test results resulting in 8 meaningful load levels. Runout was achieved at 55% load level where two other replications resulted in finite lives. At 90% load level, range of life in 3 replicates was high so a fourth replicate was performed. *Figure 33* shows 90° cross-tension fatigue tests yielded results with minimal scatter at each load level and most load levels at 45° yielded results with minimal scatter and 95% and 65% with reasonable scatter.

Table 9: Completed test matrix for Al 6016 2mm by 1mm SPR cross-tension specimens with load levels determined from maximum load of quasistatic results and r-ratio = 0.1

90°				
% QS L_{max}	L_{max} [N]	L_{min} [N]	Frequency [Hz]	Quantity
95%	3363	336.3	5	3
90%	3186	318.6	5	3
85%	3009	300.9	5	3
80%	2831	283.1	5	3
75%	2655	265.5	5	3
70%	2478	247.8	10	3
65%	2300	230	10	3
60%	2124	212.4	10	1

45°				
% QS L_{max}	L_{max} [N]	L_{min} [N]	Frequency [Hz]	Quantity
95%	2326	232.6	5	2
90%	2204	220.4	5	4
85%	2082	208.2	5	3
80%	1959	195.9	5	3
75%	1837	183.7	5	3
70%	1714	171.4	5	3
65%	1592	159.2	10	3
60%	1469	146.9	10	3
55%	1347	134.7	10	3

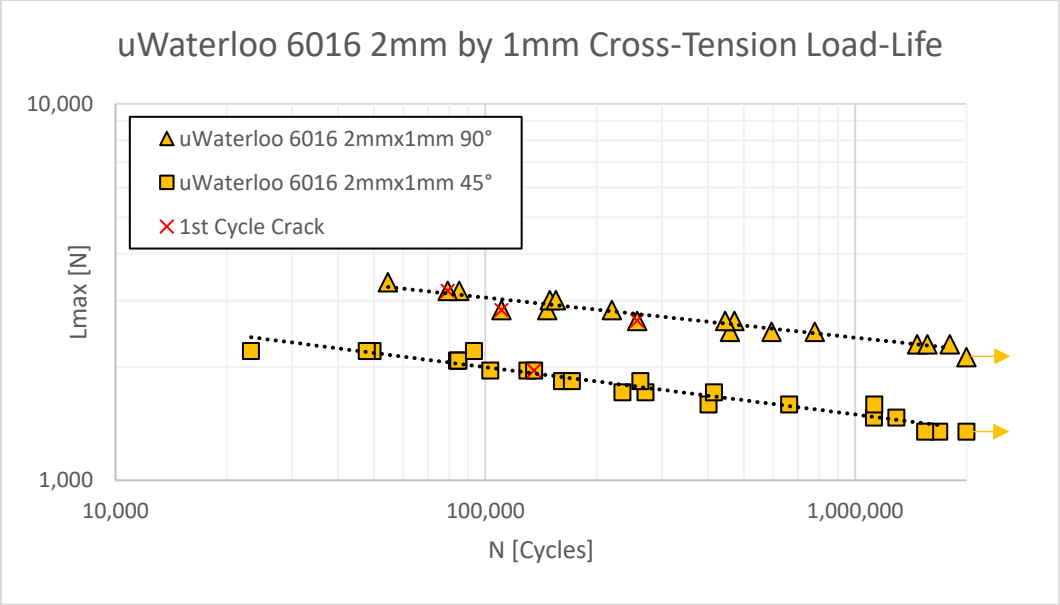

Figure 33: Al 6016 2mm by 1mm SPR cross-tension load-life plot with arrow indicating runout data points and specimens with 1st cycle cracking

All Al 6016 2mm by 1mm SPR cross-tension fatigue specimens in both 90° and 45° loading orientations failed at the 1mm bottom clinched sheet with no visible damage in the 2mm pierced sheet as shown in *Figure 34* and *Figure 35*.

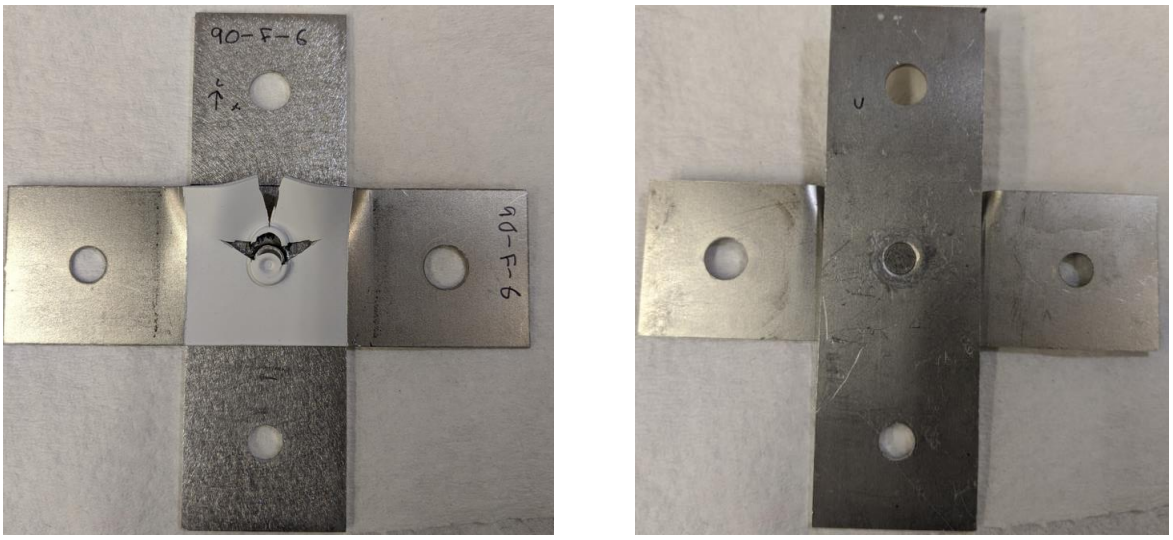

Figure 34: Al 6016 2mm by 1mm SPR cross-tension post fatigue test 90° test pierced 2mm sheet (left) and clenched 1mm sheet (right) N_{final} = 110,571

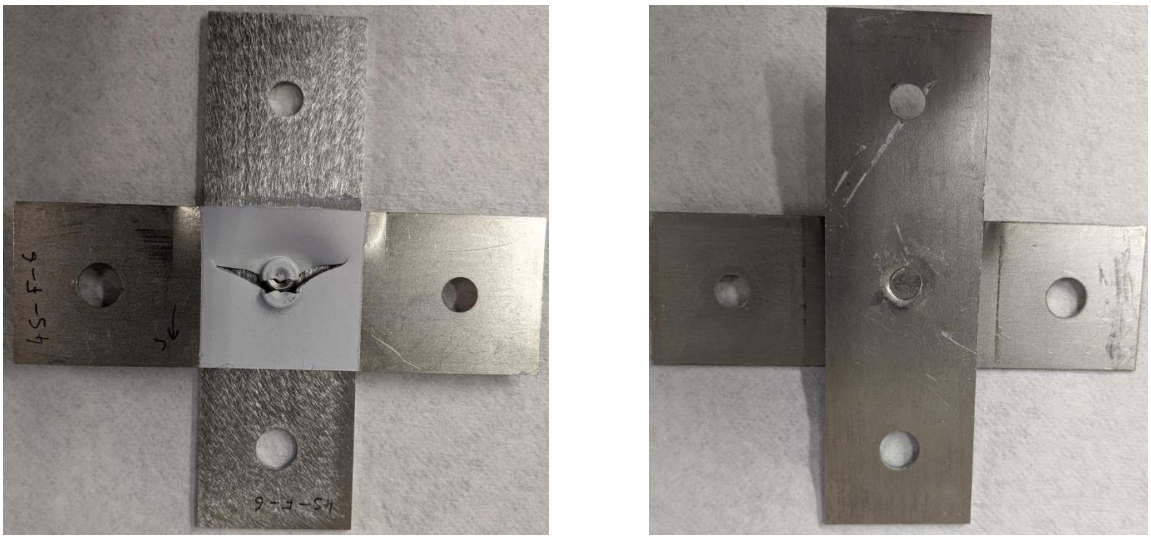

Figure 35: Al 6016 2mm by 1mm SPR cross-tension post fatigue test 45° test pierced 2mm sheet (left) and clenched 1mm sheet (right) N_{final} = 663,483

One specimen from each load level at 90%, 80%, and 75% L_{max} tested in 90° loading orientation, and one specimen at 80% L_{max} tested in 45° loading orientation developed a tangential crack at the formed protrusion of the clenched sheet during first cycle. Damage occurs in between two edges of the formed protrusion's outermost surface, where the SPR flared leg has penetrated furthest into the clenched sheet shown in *Figure 36*. This damage is consistently on the side of the joint where load is applied and where the sheet is in tension at both L_{max} and L_{min} load levels. Final life values of three specimens tested in 90° loading orientation with first cycle tangential cracks were all lowest life data points amongst their respective load

levels, with increasing difference in life as load level decreases *Figure 33*. The single specimen with first cycle tangential cracking at 45° loading orientation had highest final life value at 80% L_{max} load level suggesting the 1st cycle damage has a greater effect on specimens loaded in the 90° orientation.

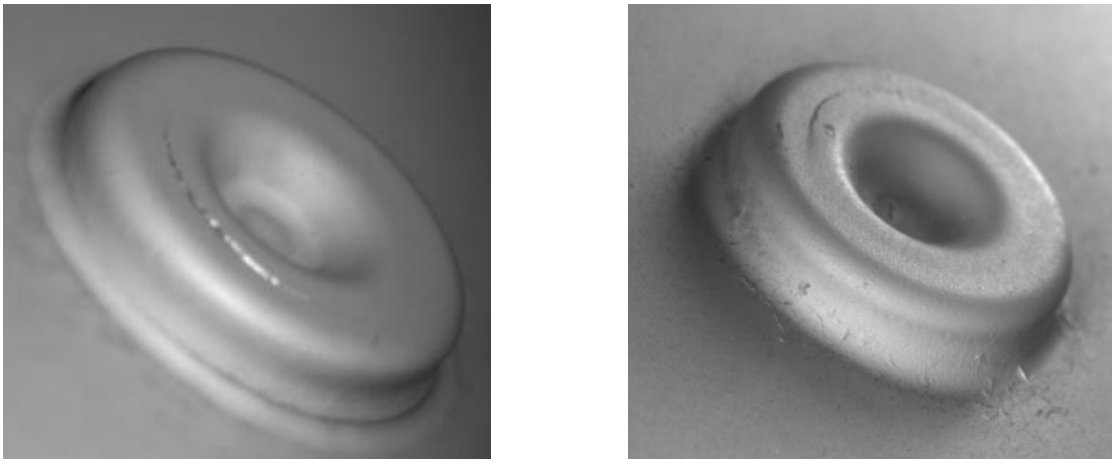

Figure 36: Al 6016 2mm by 1mm SPR cross-tension first cycle DIC images tangential crack typical of three 90° fatigue tests (left) and one 45° fatigue test (right) on clenched sheet protrusion

Figure 37: Al 6016 2mm by 1mm SPR cross-tension post fatigue test 90° clenched sheet damage at varying load levels and undamaged runout (h)

Figure 37 shows typical clenched sheet damage observed at various 90° specimen load levels where a horizontal Mode I crack passing though the formed protrusion paths outwards at both ends and transitions upwards at an angle of approximately 20°, towards loading direction in unformed areas of sheet. The small mass of clenched sheet material at the protrusion, keeping the SPR itself captive within the joint, either

splits in half horizontally along the crack or will separate concentric to the SPR flared base. Most specimens have developed Mode I cracks at the sheet top edge where crack separation plane is vertical and axial to loading direction of sheet. *Figure 37* shows depth and occurrence of this vertical crack is inconsistent and uncorrelated at all load levels. Out of plane deformation is pronounced in mass of clenched sheet separated from main mass of material by two radial cracks where two modes of deformation can be observed. A radial bulge due to buckling where deformation is most severe at a radius of about 10mm is shown in *Figure 37 (a), (c), (e)* and *(g)*, outwards twisting of sheet shown in *Figure 37 (b)* and *(f)* or combination of both as seen in *Figure 37 (d)*, where top left quadrant has twisted out of plane and top right quadrant has radial bucking.

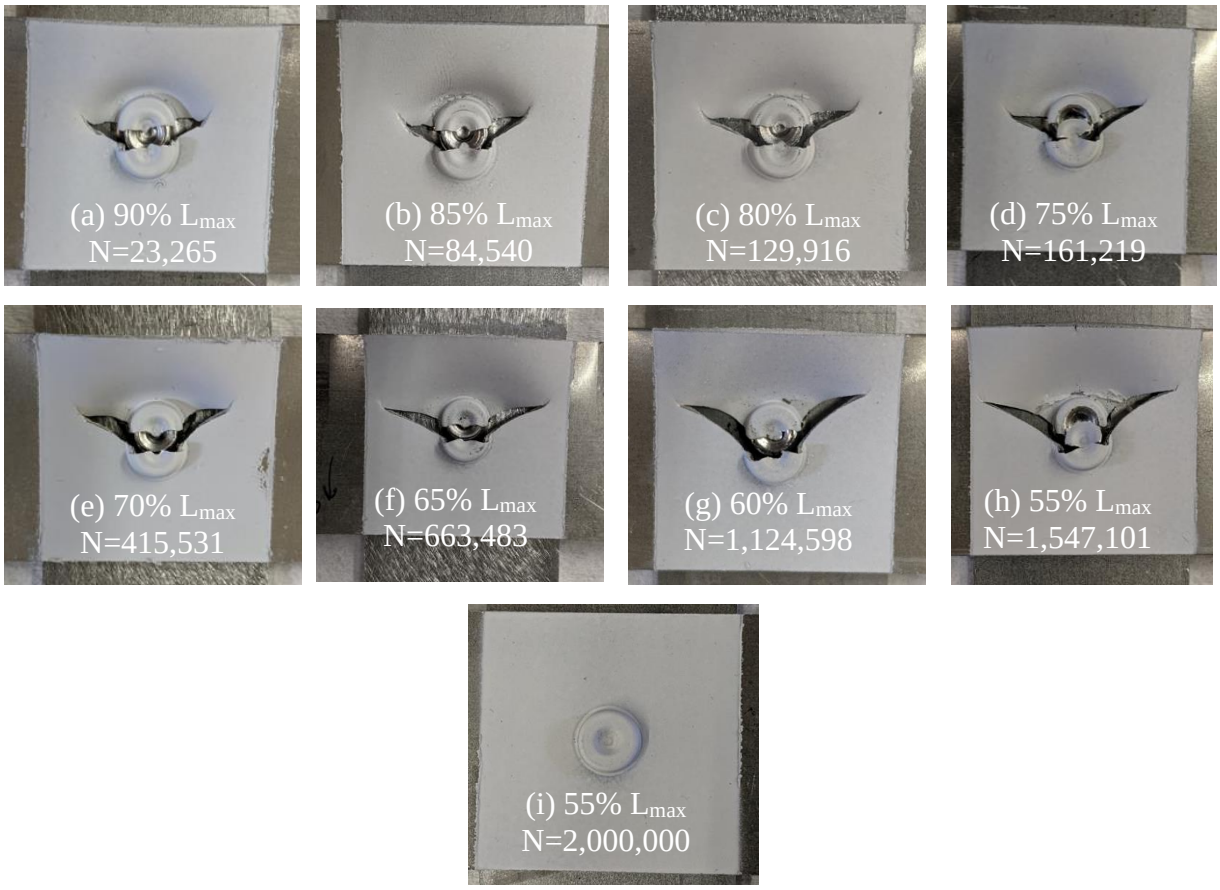

Figure 38: Al 6016 2mm by 1mm SPR cross-tension post fatigue test 45° clenched sheet details of varying load levels undamaged runout (i)

Figure 38 shows typical clenched sheet damage observed at various 45° specimen load levels with primarily Mode I crack passing horizontally though the formed protrusion and upwards toward in-plane loading direction in unformed areas. When compared to 90° specimens in *Figure 37*, this crack propagates differently in length and direction in unformed areas of the clenched sheet. Additionally, correlation exists

for crack length and crack pathing as load levels change from high to low. High load level specimens shown in *Figure 38 (a), (b), (c)* and *(d)* have short straight crack paths of approximately 6-8mm in length, are approximately 30° offset from horizontal plane and propagate towards in-plane loading direction of the sheet. As load levels decrease from 90% to 75% l_{max} the crack length typically increases and remains straight. *Figure 38 (e), (f), (g)* and *(h)* show that with load level decrease, crack length further increases and propagates along a curved path away from in-plane loading direction of the sheet. These curved cracks in unformed sheet areas at lower load levels appear near tangent with circumference of the SPR itself, whereas higher load level cracks appear to be near radial.

The two observed out of plane deformation modes in clenched sheet unformed areas also show correlation with load level decrease. Similar to 90° specimens, out of plane deformation occurs in unformed clenched sheet areas where applied load initially causes compression and have been partially isolated by crack discontinuity. At all load levels, sheet separation of approximately 3-5mm occurs at the top edge closest to sheet in-plane loading direction, and approximately 2-4mm at the opposite edge. Specimens tested at high load levels with short cracks show an inflection point in between the small radius out of plane radial bend near SPR protrusion and the shallower outer radial bend *Figure 38 (a) and (b), (c), (d)* and *(e)* caused by multiaxial loading. As load levels reduce in magnitude, the outer shallow radius approaches infinity. Furthermore, increase in crack length results in change in geometry and boundary conditions contributing to joint stiffness decrease. This change in geometry and reduction of stiffness changes high load level deformation mode to out of plane twisting *Figure 38 (g)* and *(h)*. Crack ends at all load levels have sudden change in angle towards in-plane loading direction of the sheet.

DIC images in *Figure 39 (b)* and *(f)* show signs of damage where two radial cracks propagating at approximately 20° offset from horizontal plane, though unformed areas of the clenched sheet, are visible. The growing geometrical discontinuity caused by two propagating radial cracks change boundary conditions and therefore stiffness of the clenched sheet, allowing previously described bending, buckling, and twisting damage to occur in the near separated mass. Once two radial cracks have sufficiently propagated, most specimens develop a third crack at the clenched sheet top edge due to tensile bending stress, the intensity of which increases as radial cracks extend. *Figure 39 (c)* and *(g)* show that two radial cracks eventually join by propagating through the entire formed protrusion. *Figure 39 (g)* shows this crack due to bending just before final separation and the increase in crack depth after final separation *Figure 39 (d)* and *(h)*. *Figure 39* also shows any significant out of plane deformation such as twisting, buckling or a combination of both, is direct cause of final separation as this occurs during final cycle of fatigue testing.

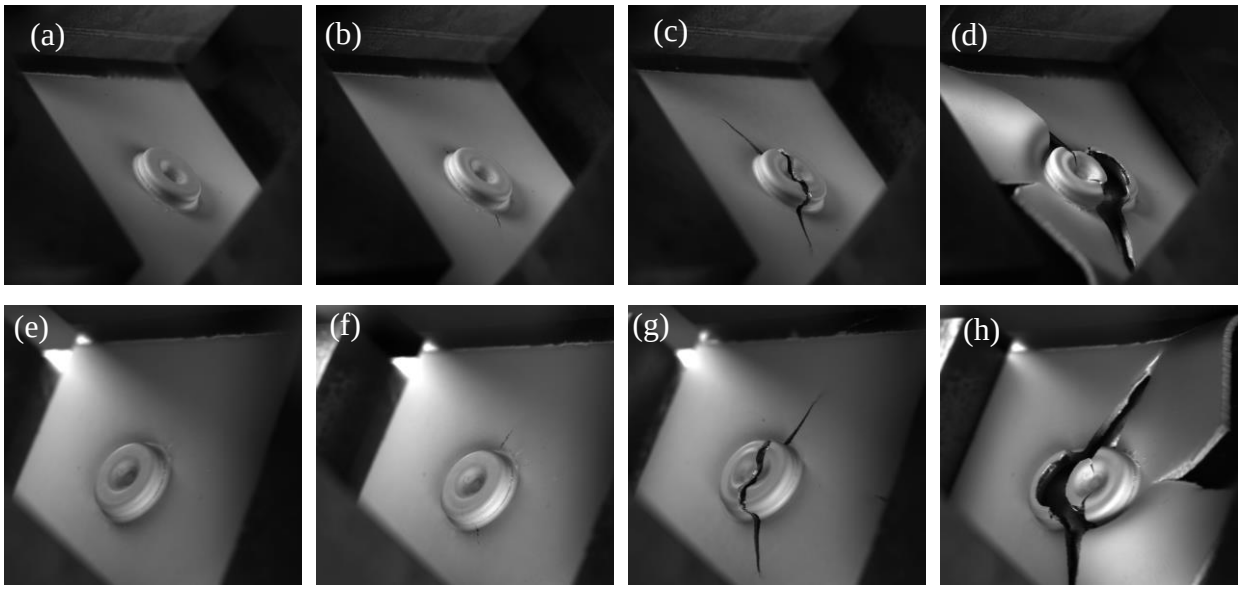

Figure 39: Al 6016 2mm by 1mm SPR cross-tension 90° DIC images (a) (b) pre-test, (b) (f) visible crack at N = 210,000, (c) (g) frame before separation, (d) (h) separation at N_{final} = 220,142 clenched sheet details (top row camera 1, bottom row camera 2)

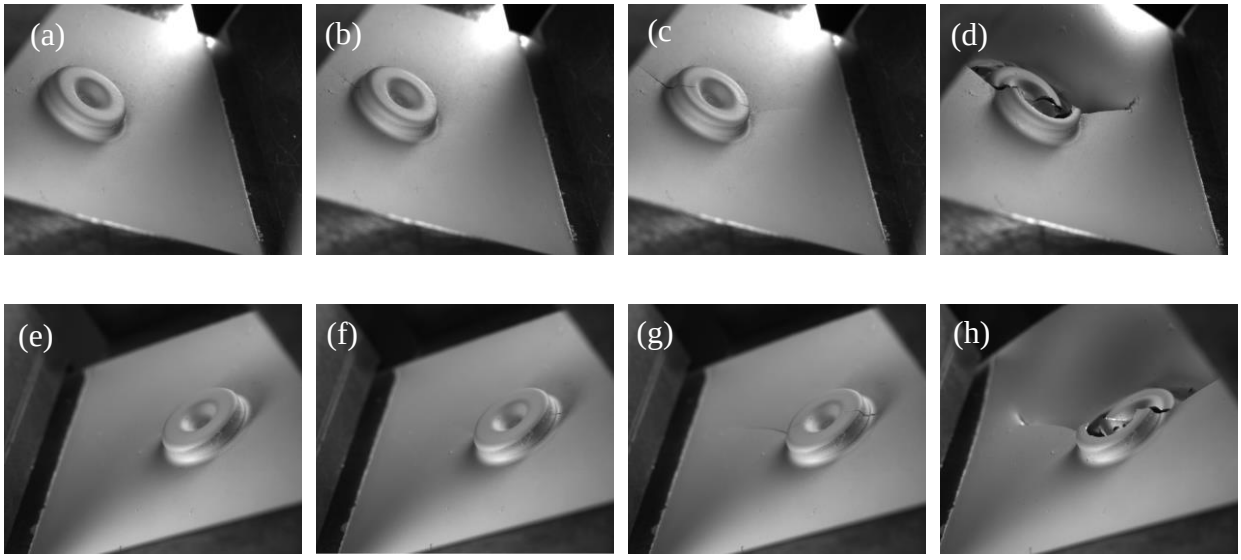

Figure 40: Al 6016 2mm by 1mm SPR cross-tension 45° DIC images (a) (b) pre-test, (b) (f) visible crack at N =247,500, (c) (g) frame before separation, (d) (h) separation at N_{final} = 262,459 clenched sheet details (top row camera 1, bottom row camera 2)

Although *Figure 37* and *Figure 38* show 90° and 45° specimens have different crack pathing and modes of failure after sufficient radial crack development, *Figure 39* and *Figure 40* show occurrence of damage throughout cyclic life is consistent. *Figure 39* and *Figure 40 (b)* and *(f)* show similar cracking at the formed

protrusion and unformed areas of the sheet at 95% final life, *(c)* and *(g)* show similar crack advancement in unformed sheet and over the formed protrusion causing two radial cracks to meet, and *(d)* and *(h)* show out of plane deformation causing final separation at the final cycle. *Figure 38 (a)* and *(h)* show that minority of specimens develop a crack due to bending at the clenched sheet top edge, similar to specimens in 90° loading in *Figure 37*, and does not correlate with load level. The crack due to bending does not noticeably propagate any further during final cycle where major deformation occurs since multiaxial loading and final cycle out of plane deflection cause bending load component to be of small magnitude. Sudden change in crack direction at crack tips seen in *Figure 40 (d)* and *(h)* is absent in frame before separation, meaning crack transition occurs due to clenched sheet out of plane deformation. While the clenched sheet remains in plane, primarily Mode I radial cracks develop due to in plane tensile load normal to crack propagation plane. However, when out of plane deformation occurs, the applied shear load component normal to joint sheets becomes dominant, transitioning the Mode I crack to out of plane shear Mode III.

Figure 41 and *Figure 42* show closer view of crack propagation behavior of specimens shown in *Figure 39* with N_{final} = 220,142 and *Figure 40* with N_{final} = 262,459 respectively. *Figure 41 (e)* and *Figure 42 (b)* show first visible signs of damage where a crack is visible formed protrusion base radius to halfway up the formed protrusion sidewall. The crack in *Figure 41 (e)* is more visibly identifiable at the formed protrusion base where black aluminum fretting debris has leaked providing high visual contrast, whereas *Figure 42* shows a visible crack with no traces of fretting debris. Absence of visually identifiable damage at the surface shown in *Figure 41 (b)* and *Figure 42 (e)*, which shows the opposite side of the formed protrusion, suggests that two expected radial cracks may not develop simultaneously. *Figure 41* and *Figure 42 (c)* and *(f)* show development of a second radial crack, and where both radial cracks have advanced at both ends. In one direction, radial cracks propagate outwards and upwards approximately 20° towards sheet loading direction on unformed areas of the 90° specimen's clenched sheet, with significant traces of fretting debris. 45° specimens develop similarly to that of 90° specimens; however, radial cracks are at greater angle of approximately 30° towards sheet loading direction and have small traces of fretting debris. On the opposite end, cracking has extended the full length of formed protrusion sidewall, over protrusion outer radius, and across the outer most surface, with no signs of fretting debris in both 45° and 90° specimens.

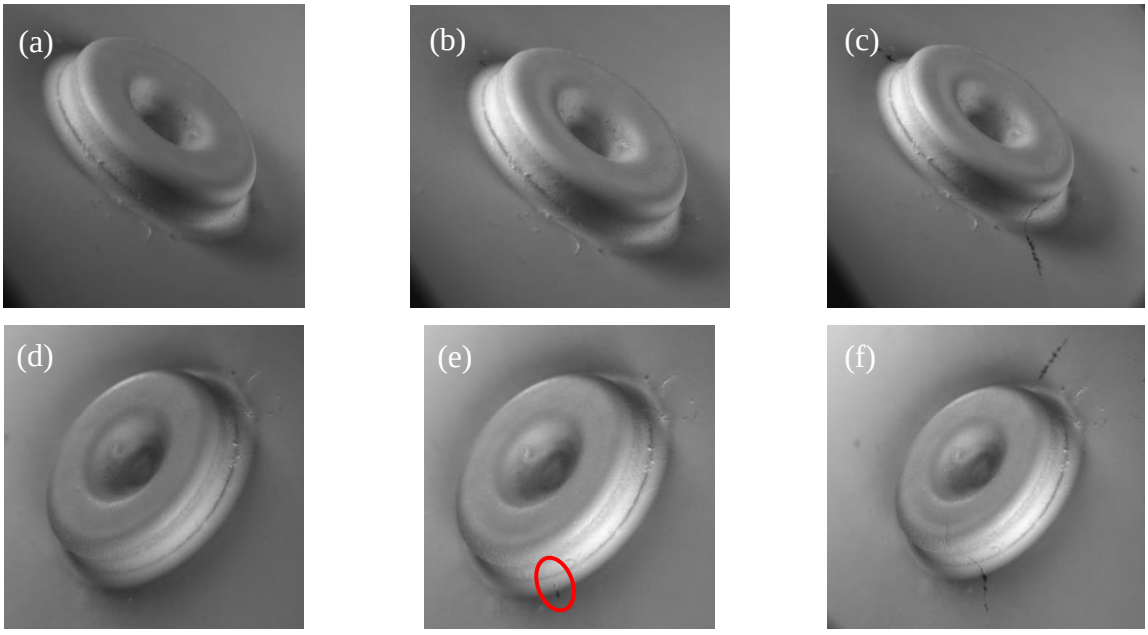

Figure 41: 90° specimen clenched sheet protrusion crack propagation details of Figure 39 specimen DIC images (a) (d) pre-test, (b) (e) N = 172,500, and (c) (f) N = 210,000 (top row camera 1, bottom row camera 2)

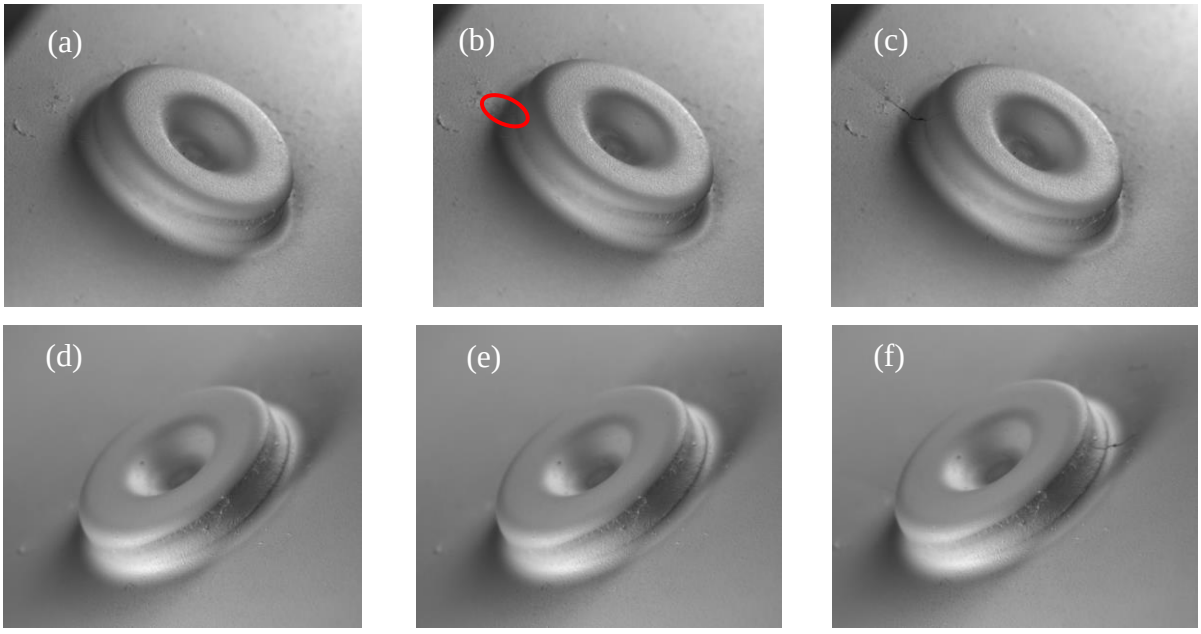

Figure 42: 45° specimen clenched sheet protrusion crack propagation details of Figure 40 specimen DIC images (a) (d) pre-test, (b) (e) N = 225,000 and (c) (f) N = 247,500 (top row camera 1, bottom row camera 2)

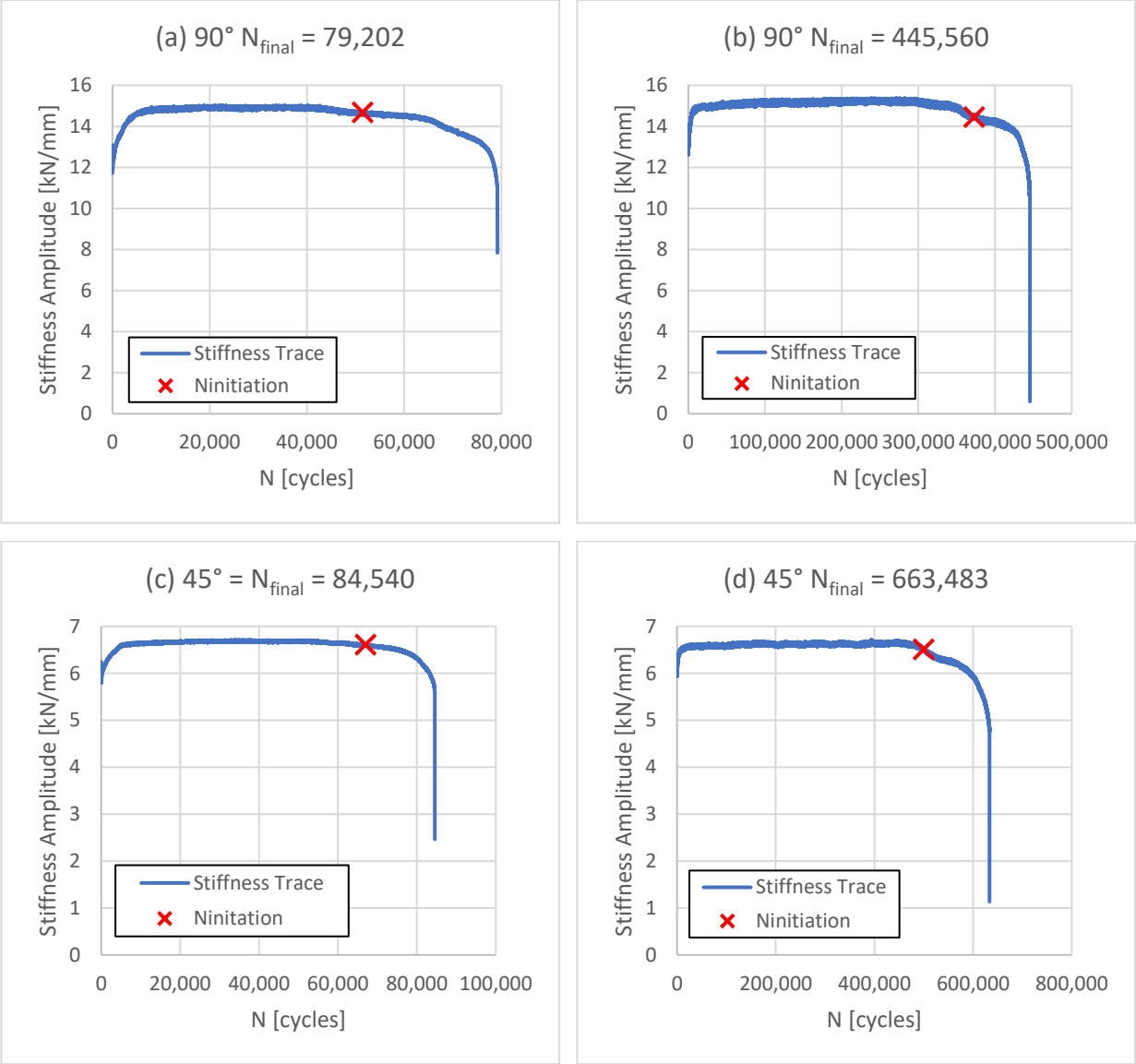

Figure 43: Al 6016 2mm by 1mm SPR cross-tension stiffness plots of 90° specimens (a), (b) and 45° specimens (c), (d) and crack initiation life

Time history of SPR joint stiffness during cyclic testing is calculated from force and displacement values acquired from load frame transducers where k, the stiffness amplitude is calculated by:

$$k = \frac{force\ amplitude}{displacment\ amplitude} \tag{41}$$

Figure 43 shows typical stiffness plots of Al 6016 2mm by 1mm SPR cross-tension 90° and 45° specimens where $N_{initiation}$ is life at first DIC image where cracking is visually identifiable. When cyclic loading begins, SPR joints increase in stiffness and plateau at a range of 3,000 to 6,000 cycles for specimens tested at high

load levels and up to 20,000 cycles for specimens tested at lower load levels. Stiffness then plateaus and remains constant until near end of life where gradual reduction in stiffness begins and then exponentially decreases towards 0. In all stiffness plots $N_{initiation}$ occurs after initial gradual stiffness drop indicating that cracking has developed below visible surface of the sheet where it is unobservable by DIC. *Figure 43 (a)* behaves slightly differently where $N_{initiation}$ occurs earlier in life and stiffness is not as constant after the stiffness plateau relative to *Figure 43 (b), (c)* and *(d)*. Some high load level specimen's stiffness traces show linear drop in stiffness after the initial gradual reduction as seen in *Figure 43 (a)* from 65,000 to 75,000 cycles.

While most specimens remained mechanically interlocked after experimentation, two 45° and one 90° specimen fully separated allowing observation of fretting at inside contact interfaces of joint shown in *Figure 44* and *Figure 45*. It can be seen that black fretting areas in 90° specimens exist on both top and bottom sides of the crack in the clenched sheet, visible *Figure 44 (right)* suggesting that the crack initiation occurs in the fretting region. Black fretting areas of 90° specimens are larger than 45° specimens and occur where clenched sheet remained in contact with pierced sheet until final separation. This is expected since the shearing force causing the sheet bending has a smaller component in 45° loading orientation in addition to the perpendicular tensile component that tends to separate the sheets axially along the SPR. Although traces of fretting residue exist on clenched sheet bottom side, a black fretting region as seen in the 90° specimen is absent.

Figure 44: Fully separated Al 6016 2mm by 1mm SPR cross-tension 90° specimen N_{final} = 415,531 2mm pierced sheet (left) and 1mm clenched sheet (right) fretting damage at sheet contact interface

Figure 45: Fully separated Al 6016 2mm by 1mm SPR cross-tension 45° specimen N_{final} = 83,947 2mm pierced sheet (left) and 1mm clenched sheet (right) fretting damage at sheet contact interface

The 90° 1mm specimen clenched sheet micrograph in *Figure 46* shows relatively smooth surface in fretting area towards the SPR itself with a patch of damage consisting of cracks circled in red, where crack propagation planes are perpendicular and normal to loading direction. In fretting areas adjacent to undamaged areas of sheet, large ridges have developed with smaller ridges towards the center of the joint. *Figure 47* show that similar ridges exist at similar locations in fretting areas on 90° 2mm pierced sheet, although only larger ridges have developed. Inner areas circled orange and red show delamination damage, with finer damage occurring in red highlighted areas, indicating different damage modes occurring in 2mm pierced sheet and 1mm clenched sheet. *Figure 48* again shows ridges developed at outer edges of fretting area and several damaged areas with oblique crack propagation planes. Although ridge edges appear smooth in 90° 1mm clenched sheet and 45° 2mm sheet, *Figure 48* shows buildup of cracked debris at ridge ends closest to SPR joint center. EDX was used to obtain the elemental composition of ridges observed in fretting regions where *Figure 50* show that the elemental composition consists mostly of aluminum and oxygen resulting in Al2O3, also discovered by [25]. Small traces of other elements such as silicon, iron and carbon exist as they are alloying components to the Al 6016 sheet material and steel SPR itself. Presence of carbon and iron at this location indicates that debris from SPR itself has been transported across and to the edge of the fretting regions. It should be noted that fretting investigation was not performed on any Al 6016 1mm by DX54D 0.95mm specimens since all remained mechanically interlocked after experimentation.

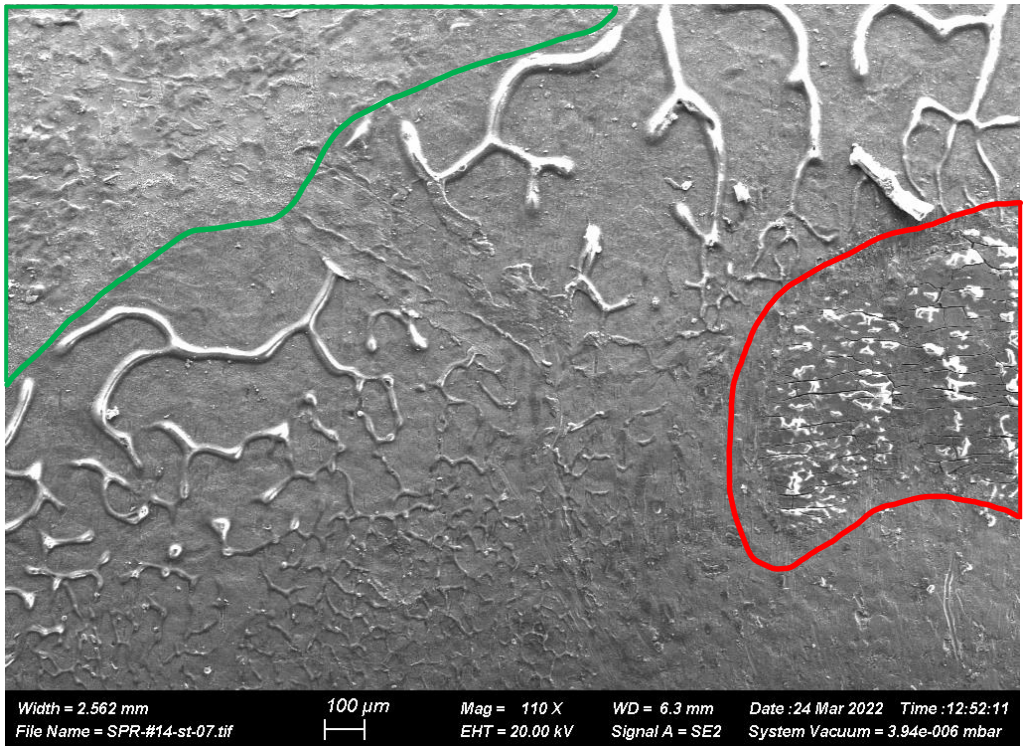

Figure 46: SEM micrograph of 1mm clenched sheet from Figure 44 (right) with undamaged area (green), visible cracks (red) in fretting region

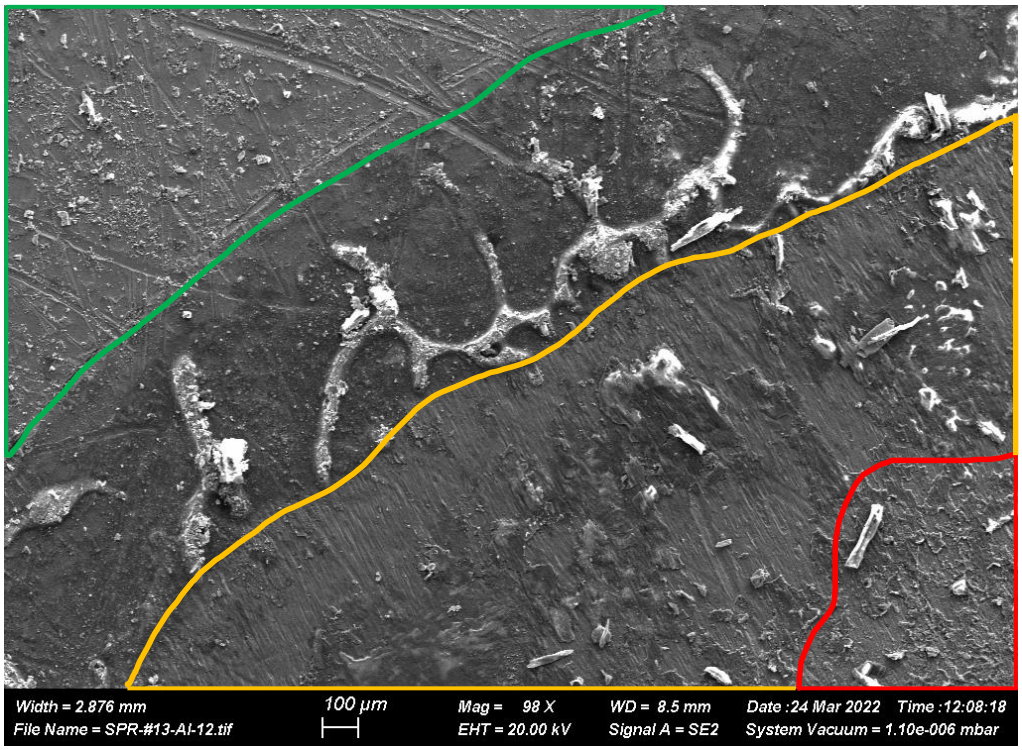

Figure 47: SEM micrograph of 2mm pierced sheet from Figure 45 (left) with undamaged area (green), visible damage in fretting region (red and orange)

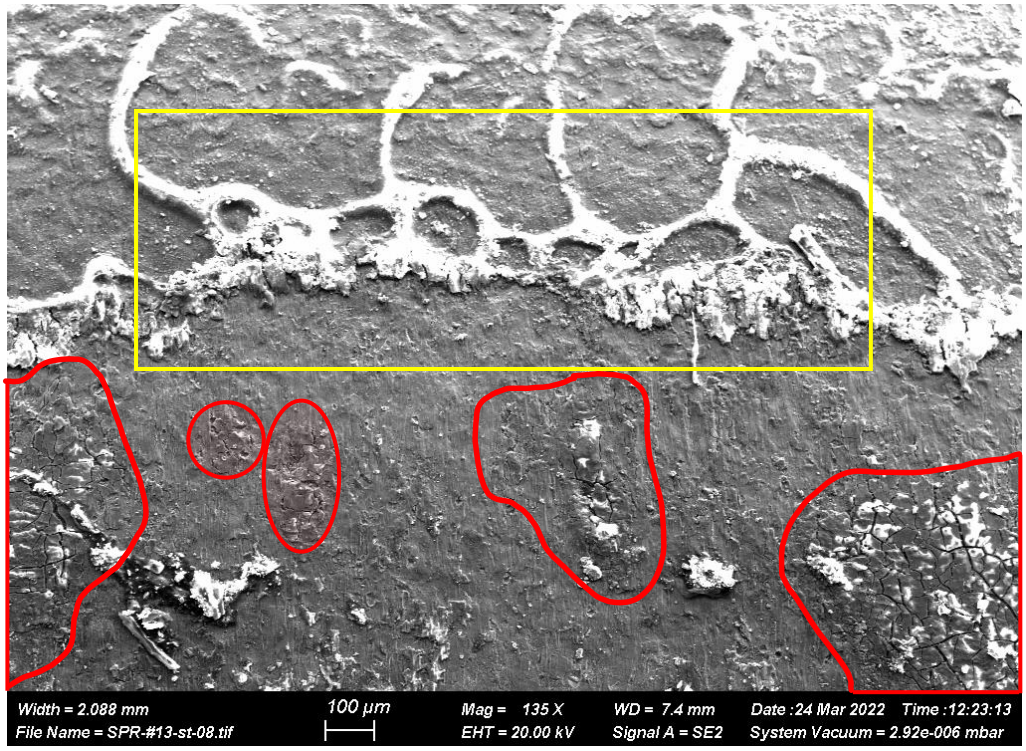

Figure 48: SEM micrograph of 1mm clenched sheet from Figure 45 (right) with visible cracks (red) in fretting region with EDX zone highlighted in yellow

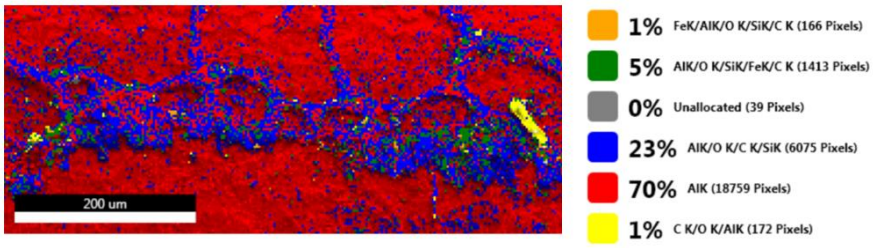

Figure 49:EDX zone highlighted in yellow from Figure 48

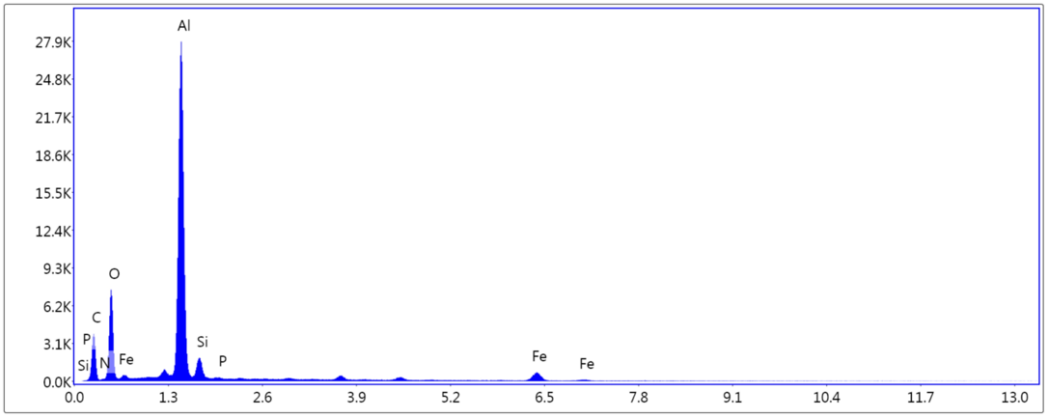

Figure 50: Fretting debris spectrum of yellow highlighted area Figure 48 and Figure 49

5.2.2. Fatigue Al 6016 1mm by DX54D 0.95mm

Al 6016 1mm by DX54D 0.95mm cross-tension fatigue test load levels used in *Figure 51* are shown in *Table 10.* All resulted in finite life and load levels with multiple replicates have minimal scatter.

Table 10: Completed test matrix for Al 6016 1mm by DX54D 0.95mm cross-tension specimens with load levels determined from maximum load of quasistatic results and r-ratio = 0.1

90°				
% QS L_{max}	L_{max} [N]	L_{min} [N]	Frequency [Hz]	Quantity
85%	2763	276.3	5	1
75%	2438	243.8	5	1
70%	2275	227.5	5	1

45°				
% QS L_{max}	L_{max} [N]	L_{min} [N]	Frequency [Hz]	Quantity
80%	2000	200.0	5	2
70%	1750	175.0	5	1
65%	1625	162.5	5	1
60%	1500	150.0	5	3

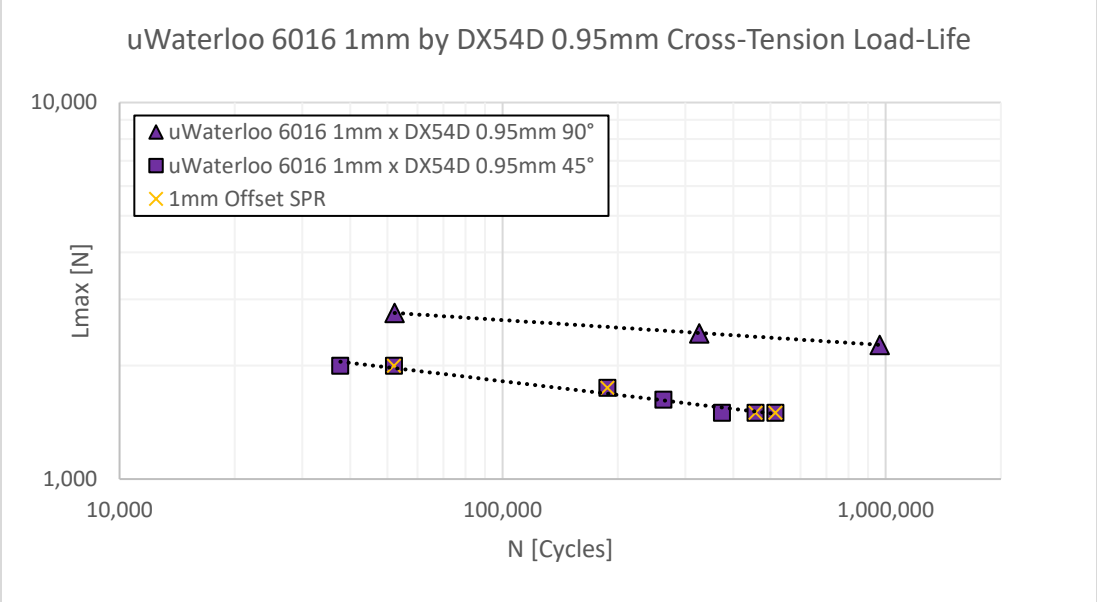

Figure 51: Al 6016 1mm by DX54D 0.95mm SPR cross-tension load-life plot with offset SPR specimens indicated

All Al 6016 1mm by DX54D 0.95mm SPR cross-tension fatigue specimens in both 90° and 45° loading orientations show damage in both pierced and clenched sheets as shown in *Figure 52* and *Figure 53*.

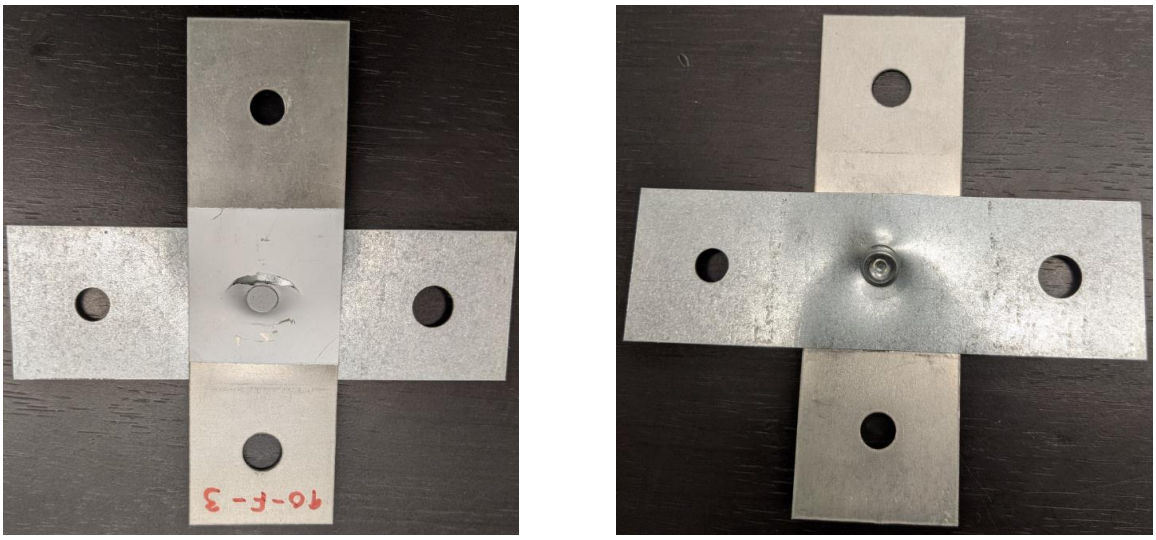

Figure 52: Al 6016 1mm by DX54D 0.95mm SPR cross-tension post fatigue test 90° test pierced 1mm sheet (left) and clenched 0.95mm sheet (right) N_{final} *= 52,271*

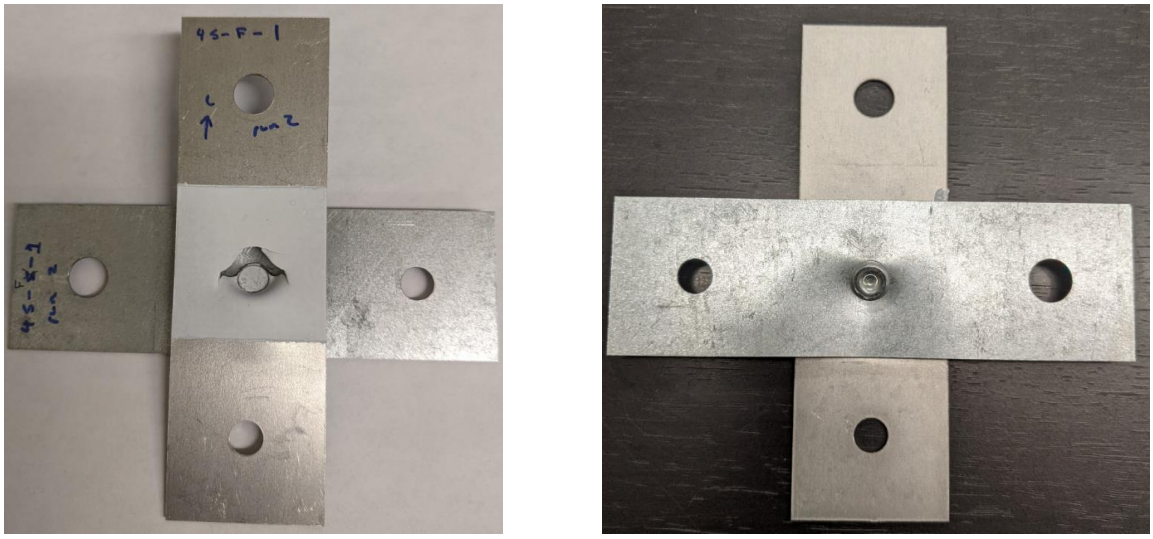

Figure 53: Al 6016 1mm by DX54D 0.95mm SPR cross-tension post fatigue test 45° test pierced 1mm sheet (left) and clenched 0.95mm sheet (right) N_{final} *= 374,527*

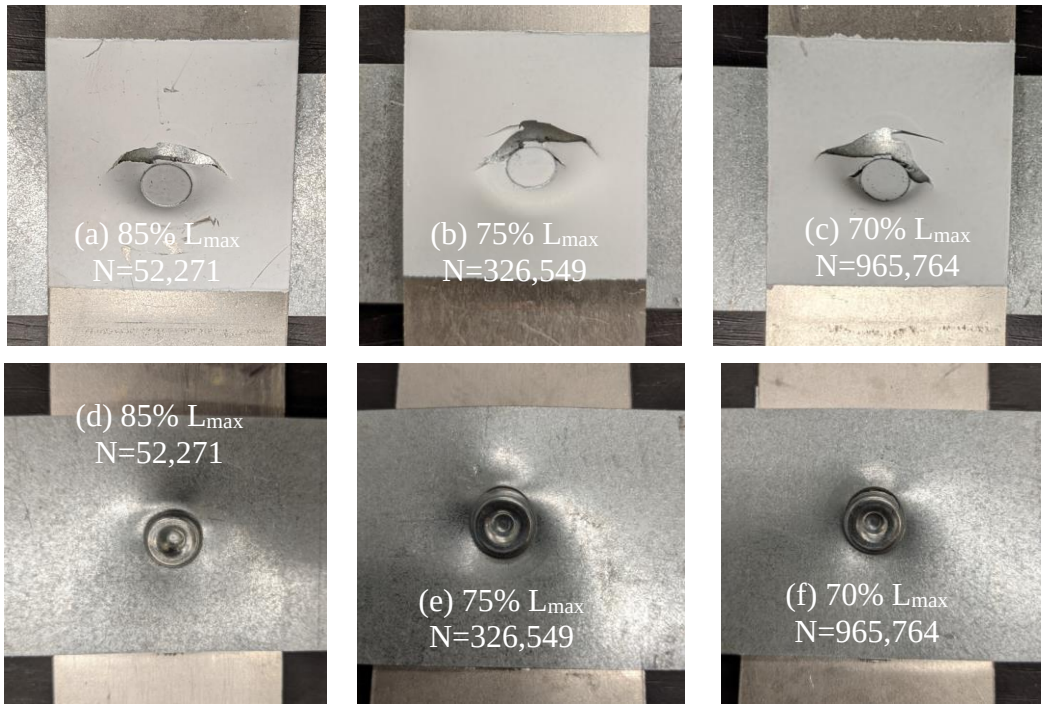

Figure 54: Al 6016 1mm by DX54D 0.95mm SPR cross-tension post fatigue test 90° pierced sheet details (a-c) and clenched sheet details (d-h) of varying load levels

Figure 54 (a), (b) and *(c)* show damage in pierced sheet of 90° specimens where Mode I cracking has developed tangent to SPR head where the stress state is tension at both L_{max} and L_{min} load levels. Damage seen *Figure 54 (a)* consists of single crack whereas *Figure 54 (b)* and *(c)* consist of multiple joined cracks. All crack tips path away from loading direction towards compressive side of the pierced sheet in all 90° specimens. *Figure 15 (right)* describes joint deformation behavior well, where the SPR has significant angular displacement similar to quasistatic specimens, and where the SPR top edge in contact with tension side of the pierced sheet displaces inwards towards the clenched sheet, and the SPR bottom edge in contact with compression side displaces outwards. The compressive side of unformed and unclamped areas of the pierced sheet have severely deformed out of plane, away from the clenched sheet where deformation is due to SPR rotation, bending the remainder of mechanically interlocked pierced sheet. It is visible in *Figure 54 (e)* and *(f)* that tangential cracking develops at high cyclic life specimens at the clenched sheet protrusion base while no crack exists in low cyclic life specimen in *Figure 54 (d)*. Cracking in *Figure 54 (f)* has propagated further and has wider crack width than higher life specimen *Figure 54 (e)*. Similar to pierced sheet, bottom sheet has same out of plane sheet deformation seen in quasistatic testing caused by same angular displacement of the SPR itself. Pierced and clenched sheets have separated from each other; however, still maintain contact at clenched sheet bottom edges and at pierced sheet surrounding the SPR itself.

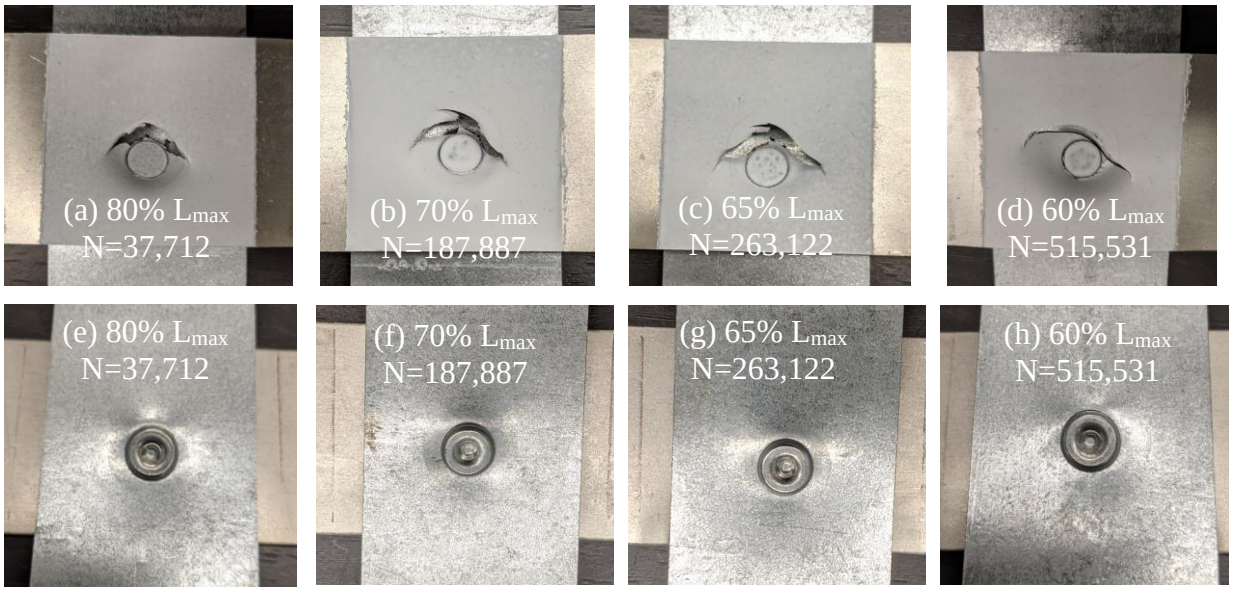

Figure 55: Al 6016 1mm by DX54D 0.95mm SPR cross-tension post fatigue test 45° pierced sheet details (a-d) and clenched sheet details (e-h) of varying load levels

Figure 55 (a), (b), (c) and *(d)* show pierced sheet damage of 45° specimens with cracking in same locations, tangent to SPR head at tension side of the pierced sheet, as 90° specimens. Similar to 90° specimens, crack direction typically paths away from loading direction towards compression side of pierced sheet although, at greater angle. The observation in *Figure 38* where final life increase results in crack length increase, is also apparent in *Figure 55 (a), (b), (c)* and *(d)* suggesting that under45° loading, crack length is dependant on load level magnitude. 4 specimens as indicated in Figure 51 were erroneously manufactured with SPR offset 1mm off center, along the direction perpendicular to loading. *Figure 55 (b)* and *(d)* show damage details of pierced sheet with offset SPR, where higher load level specimens have crack propagation similar to centered SPR specimens and lower load level specimens have all shown typical asymmetrical cracking seen in *Figure 55 (d)*. *Figure 55 (d)* shows crack geometry tangent to SPR circumference offset towards the shorter 18mm side. Crack pathing on 18mm side behaves similarly to typical crack pathing seen in centered SPR joints in *Figure 55 (a)* and *(c)*. However, crack propagating towards the 20mm side paths upward toward loading direction and then reverses to path downwards away from loading direction. It can be seen in *Figure 51* that L_{max} = 2000N and L_{max} = 1500N load levels have minimal scatter and contain replicates with and without off centered SPR, suggesting that offset of 1mm is negligible in terms of fatigue life.

When compared to 90° specimens, since 45° specimens experience in-plane load component of smaller magnitude and additional out of plane load component, the deformation mode of 45° specimen joint differs. The SPR itself has significantly less angular displacement resulting in different deformation modes in

compression side of the pierced sheet where two bends and inflection point exist. The pierced sheet tension side remains undeformed, and sheets overall have fully separated at outer edges by about 3-5mm and only remain in contact in the area immediately surrounding remaining mechanically interlocked material.

Figure 55 (e), (f), (g) and *(h)* show expected deformation in 45° specimen clenched sheet as described by *Figure 15 (right)* although with less deformation compared to 90° specimens. *Figure 55 (e)* shows at high load levels typical cracking develops in similar manner as *Figure 36* where tangential cracking is seen midway between two edges of the formed protrusion's outer most surface. This cracking occurs where the clenched sheet cross-sectional area is smallest due to SPR's flared base deforming the bottom sheet to create mechanical interlock. At lower load levels specimens from a small crack in the same location as 90° specimens at the tension side of the sheet *Figure 55 (h)*.

Figure 56 and *Figure 57 (b)* show damage in the form of tangential cracking at the transition between unformed and formed pierced sheet caused by SPR countersink during forming. This crack consistently appears on the pierced sheet tension side with two crack tips propagating towards compression side. Once cracking has propagated enough, final separation with significant out of plane deformation occurs during final cycle of fatigue testing shown in *Figure 56* and *Figure 57 (c)*. *Figure 56 (c)* shows further details of significant angular displacement of SPR and remaining mechanical interlock causing bending in pierced sheet. Similar twisting and tearing failure modes observed in the 45° 6016 2mm by 1mm specimens can be seen in *Figure 57 (c)*.

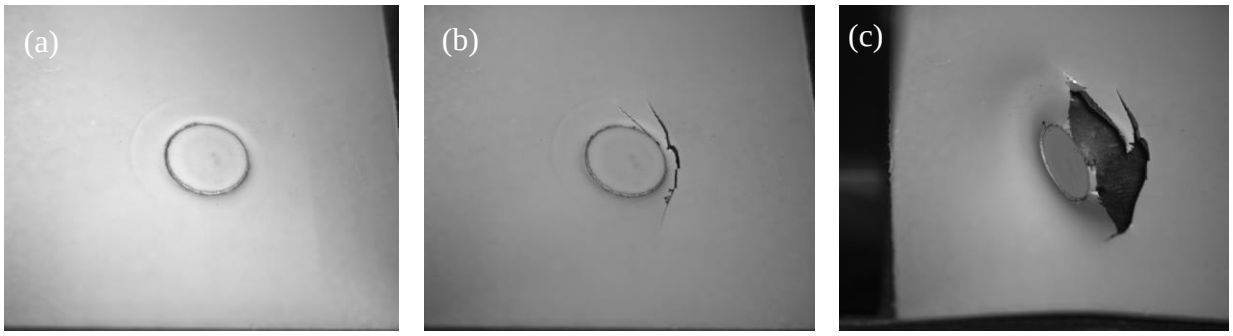

Figure 56: Al 6016 1mm by DX43D 0.95mm SPR cross-tension 90° DIC with pre-test (a), frame before separation of 5mm (b), and separation at N_{final} = 326,549 (c) pierced sheet details

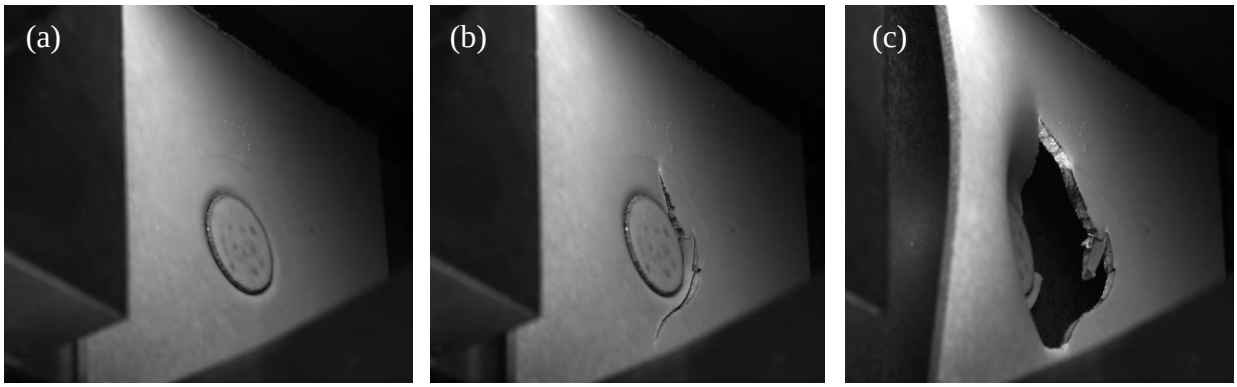

Figure 57: Al 6016 1mm by DX43D 0.95mm SPR cross-tension 45° DIC images with pre-test (a), frame before separation of 5mm (b), and separation at N_{final} = 263,122 (c) pierced sheet details

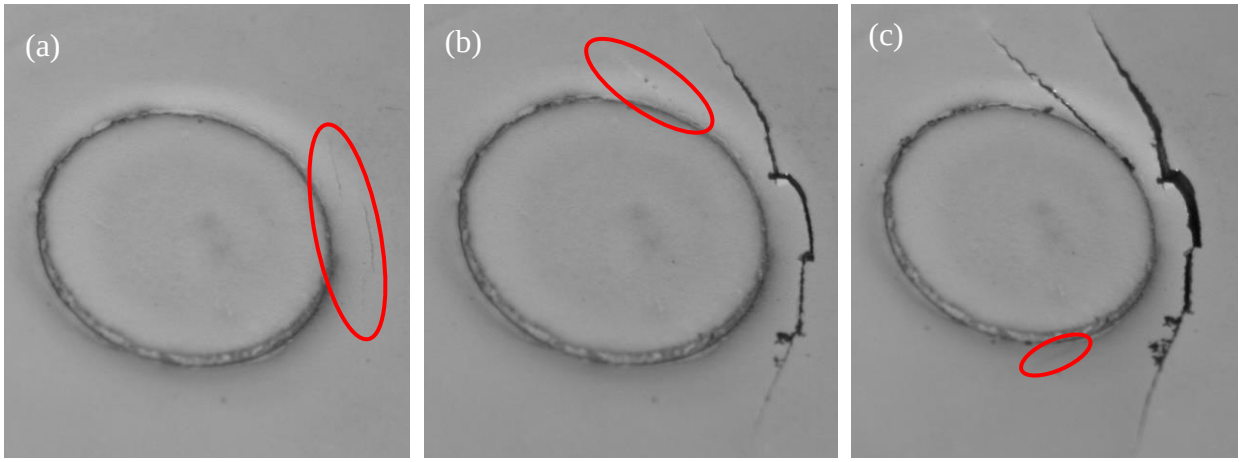

Figure 58: Pierced sheet details from N_{final} = 326,549 90° specimen in Figure 56 with first visible crack at N = 111,000 (a), propagated first crack and visible second crack at N = 300,000 (b), and frame before separation (c)

Figure 58 (a) shows cracking with two short and abrupt changes in path direction at tension side of the pierced sheet of a centered SPR specimen where crack propagation plane is normal to applied load. *Figure 58 (b)* shows development of the first crack where two crack ends have propagated outwards and slightly towards the pierced sheet compressive side. Black fretting debris has leaked out of this crack with high concentration where pathing is sharp and jagged. A second crack has developed where one end is tangent to the SPR head itself and the other end pathing more directly towards the pierced sheet compressive side. *Figure 58 (c)* shows more separation and fretting debris in the second crack and development of a third crack symmetric to the second crack. *Figure 56 (c)* shows the third crack in *Figure 58 (c)* does not significantly contribute to final separation of the joint where main cause of separation is first and second crack damage.

Figure 59: Pierced sheet details from N_{final} = 263,122 45° specimen in Figure 57 with first visible crack at N = 188,000 (a), propagated first crack and visible second crack at N = 240,000 (b), and frame before separation (c)

Figure 59 (a) shows tangential cracking at tension half, on the shorter 18mm side of pierced sheet, of off centered SPR specimen. One crack end then propagates concentrically about the SPR head, along pierced sheet unformed and formed transition radius towards the longer 20mm side, while the other end paths away from loading direction towards the pierced sheet's compressive side *Figure 59 (b)*. *Figure 59 (c)* shows angular displacement of SPR, areas of pierced sheet with intact mechanical interlock, and crack surface exposure. The second crack highlighted in *Figure 59 (b)* has propagated outwards at one end and pathed inwards radially to join with the first crack. No signs of fretting debris are observable. *Figure 60* shows stiffness traces of high load level 6016 1mm by DX54D 0.95mm SPR specimens typically behave similarly to Al 6016 2mm by 1mm specimens where an initial increase in stiffness transitions to a plateau, continuing until stiffness drop occurs near end of life. *Figure 60 (d)* shows drop in stiffness and visible cracking sooner than typical occurrence of lower life specimens where stiffness decreases linearly until near end of life. *Figure 60 (b)* shows typical behavior of Al 6016 1mm by DX54D 0.95mm 90° specimens at lower load levels where a steep stiffness drop occurs early in life. Stiffness then somewhat stabilizes, however, gradually decreases for remainder of life. For specimens with this stiffness profile, $N_{initation}$ typically occurs after the steep initial stiffness drop suggesting cause of visible damage. Like Al 6016 2mm by 1mm specimens, all Al 6016 1mm by DX54D 0.95mm stiffness traces show $N_{initation}$ occurring after stiffness drops, indicating crack initiation below observable sheet surface *Figure 61*, also documented by Fu [16] and Iyer et al. [17].

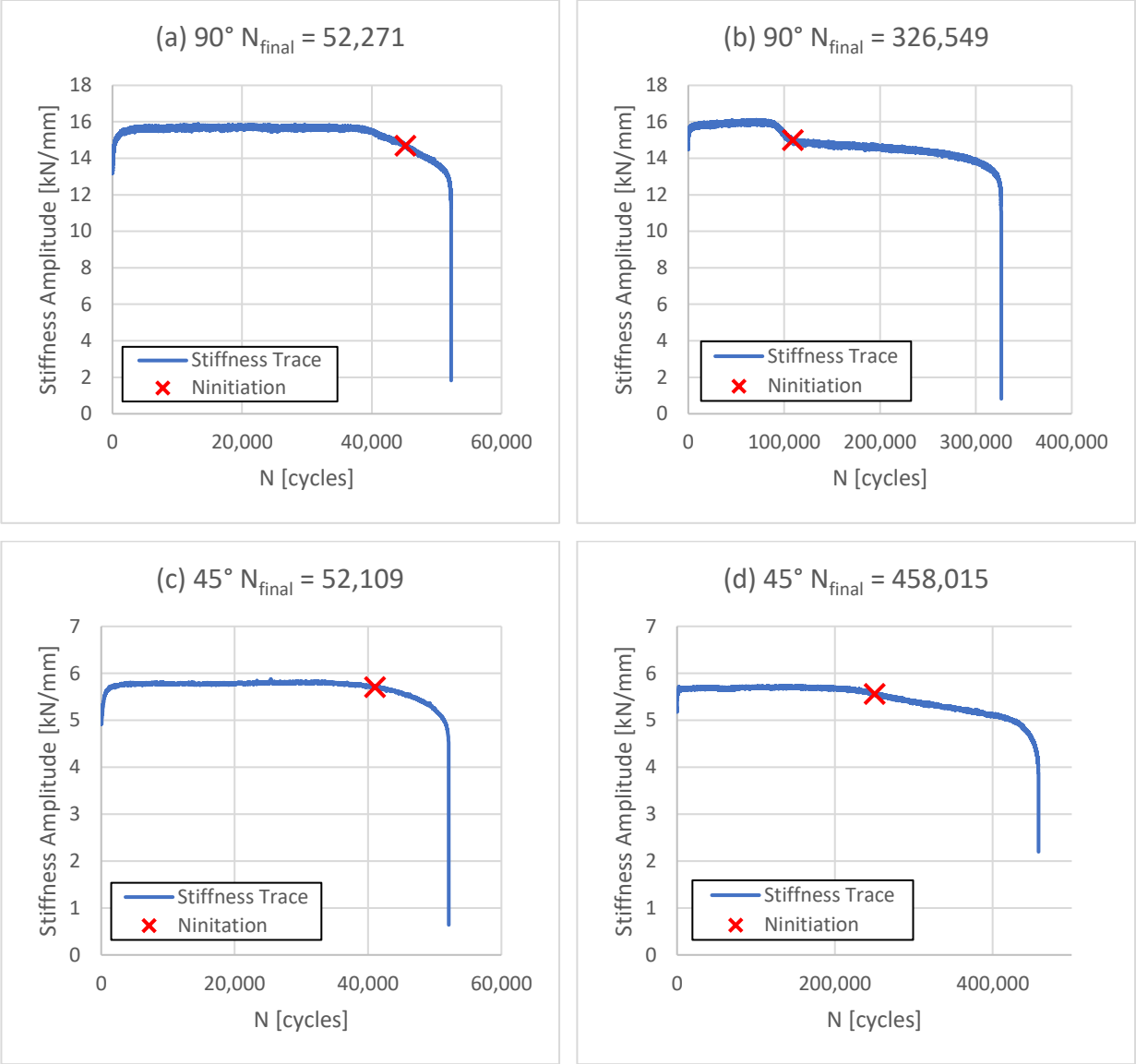

Figure 60: Al 6016 1mm by DX54D 0.95mm SPR cross-tension stiffness plots of 90° specimens (a), (b) and 45° specimens (c), (d) and crack initiation life

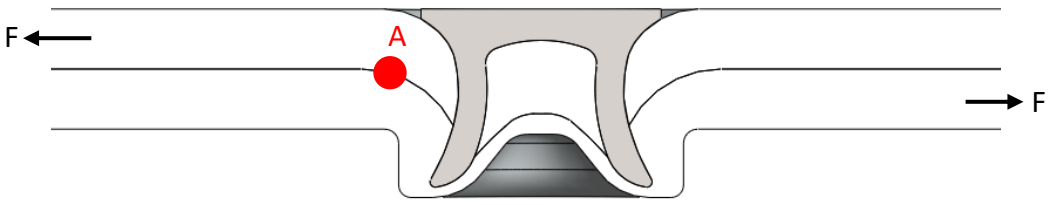

Figure 61: Typical SPR top sheet crack initiation location at point A

6. Rupp's Model Application to Uniaxial and Biaxial Loaded Cross-Tension SPR Specimens

To determine performance of nCode Rupp's Model with uniaxial and biaxial loaded cross-tension SPR specimens the procedure documented in Section 4 is replicated with Renault Group and the University of Waterloo results from Section 5. To begin, simplified linear elastic finite element models as seen in *Figure 62* were created, with sheet geometry in *Figure 7*, using 416 linear quadrilateral shell S4R elements and 1 linear beam B31 element for sheets and SPR respectively. While 2D sheet geometry is consistent with all specimens, different thickness and material combinations require unique finite element models where shell element Young's Modulus = 70 GPa and 200 GPa for aluminum and steel respectively, and steel beam element Young's Modulus = 200 GPa. Tractions from all simplified finite element models shown in *Table 11* where values were extracted for failed sheet highlighted in red, and respective stress values are shown in *Table 12*. Calculated unit stress values are scaled with corresponding load levels and plotted with corresponding final life values from experimental fatigue results.

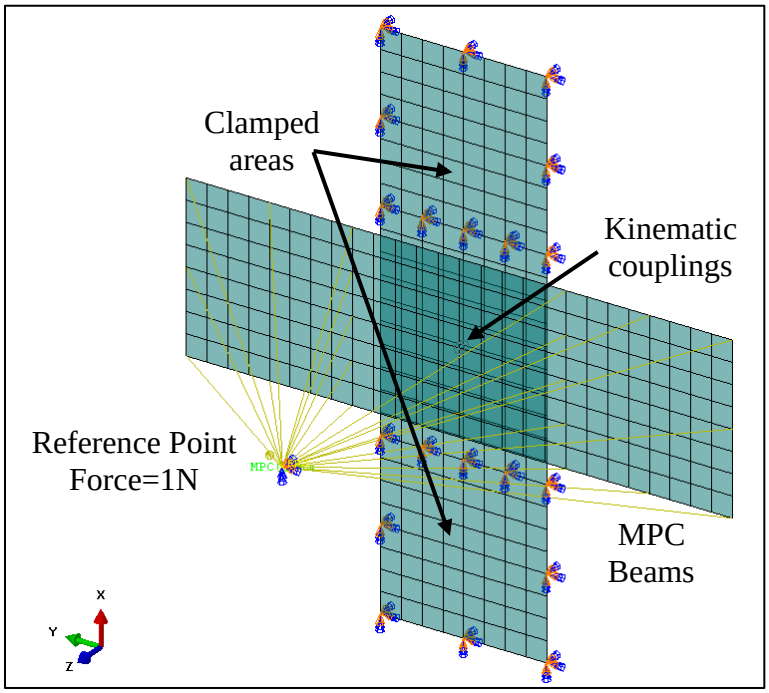

Figure 62: Simplified finite element model of cross-tension SPR joint in biaxial loading with Renault Group/The University of Waterloo tested specimen geometry

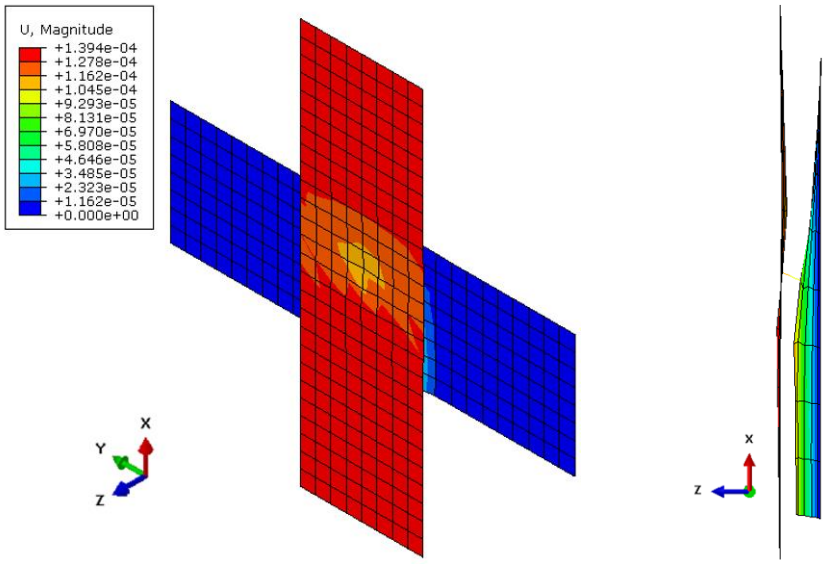

Figure 63: Displacement contour plot of cross-tension 6016 2mm by 1mm simplified finite element model 45° loading (deformation scale factor: 20,000) isometric view (left) and right view (right)

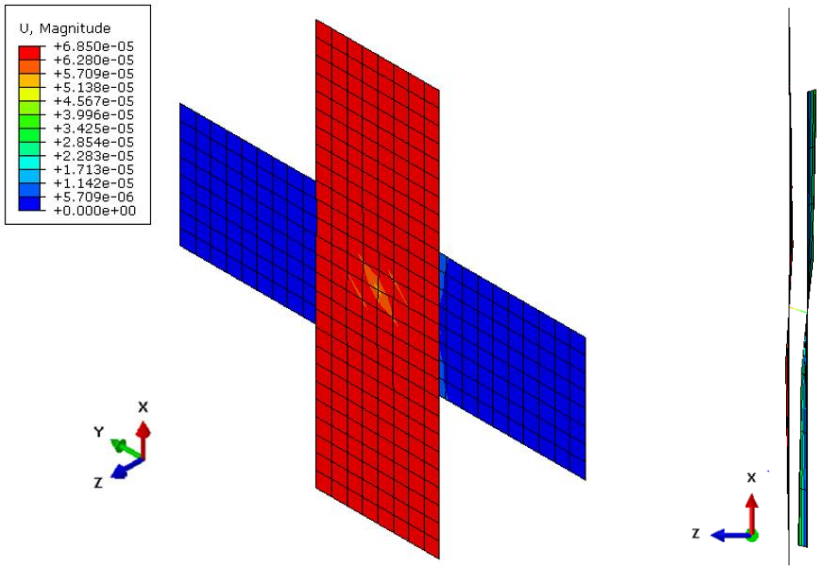

Figure 64: Displacement contour plot of cross-tension 6016 2mm by 1mm simplified finite element model 90° loading (deformation scale factor: 20,000) isometric view (left) and right view (right)

Figure 63 and *Figure 64* show deformation mode of simplified cross-tension finite element models where observed deformation is expected and agrees with experimental results. It should be noted that in *Table 11* F_x and F_z values from 45° loading are not expected, where F_x values are approximately 1.4N and F_z values are approximately 0.02N when values around $\sqrt{2}$ are expected. The beam end coupled to failed sheet F_x value is double the sum of section forces of any set of deformable shell elements along the y-direction.

Since the failure mode in all experimental results are in sheet, it may be more representative to use the sum of shell element section forces to obtain F_x and solve for F_z with static equilibrium since shell element formulation does not offer a F_z output; however, this was studied and resulted in extremely poor Rupp's model performance. For this reason and to stay consistent with existing Rupp's model methodology for the goal of compatibility validation, nodal tractions extracted from the beam element are used.

Table 11: Specimen material, geometries, and extracted unit traction values for experimental fatigue results performed by Renault/The University of Waterloo S1 (pierced sheet) or S2 (clenched sheet) red highlight indicates rupturing sheet for which tractions were extracted

Test Location	Load Angle	S1	S2	t1 [mm]	t2 [mm]	Load [N]	Fx [N]	Fz [N]	My [Nmm]
UW	45°	6016	DX54D	1	0.95	1	1.395	0.0196	0.4136
	90°	6016	DX54D	1	0.95	1	1	0	0.2966
	45°	6016	6016	2	1	1	1.387	0.0271	0.2664
	90°	6016	6016	2	1	1	1	0	0.1921
Renault	0°	6016	DX54D	1	0.95	1	0	1	0
	45°	6016	DX54D	1	0.95	1	1.395	0.0196	0.4136
	90°	6016	DX54D	1	0.95	1	1	0	0.2966
	0°	6016	6016	1	1	1	0	1	0
	45°	6016	6016	1	1	1	1.392	0.0225	0.7225
	90°	6016	6016	1	1	1	1	0	0.5191

Table 12: Unit stress values calculated from tractions and geometry in Table 11

Test Location	Load Angle	S1	S2	σ(fx) [MPa]	σ(fz) [MPa]	σ(my) [MPa]	θ	σsheet [MPa]
uWaterloo	45°	6016	DX54D	0.0562	0.0341	0.0979	180	0.1882
	90°	6016	DX54D	0.0403	0	0.0702	180	0.1104
	45°	6016	6016	0.0558	0.0476	0.0631	180	0.1666
	90°	6016	6016	0.0403	0	0.0455	180	0.0857
Renault	0°	6016	DX54D	0	1	0	0	1.744
	45°	6016	DX54D	0.0561	0.0341	0.0979	180	0.1882
	90°	6016	DX54D	0.0403	0	0.0702	180	0.1104
	0°	6016	6016	0	1	0	0	1.744
	45°	6016	6016	0.0560	0.0392	0.1711	180	0.2664
	90°	6016	6016	0.0403	0	0.1229	180	0.1632

A critical detail that should be noted; while expected failure of similar material and thickness SPR joints is usually in pierced sheets at the location where specimens are consistently under tension, failure mode is shown in *Figure 38* where the bottom clenched sheet develops cracks approximately 90° offset from applied load in either direction around the formed protrusion due to a thicker pierced sheet. A shortcoming of Rupp's model is approximation of stresses at different angles or radial locations around the SPR. Since clenched sheet fails 90° away from expected location, cosine functions in equation (15) reduce stress values

to 0. Although this should be investigated, the experimental results in *Figure 66* where the failure occurs 90° offset from applied load on either side of the formed protrusion, have been included in this study and modelled so stress values are maximum in equation (15).

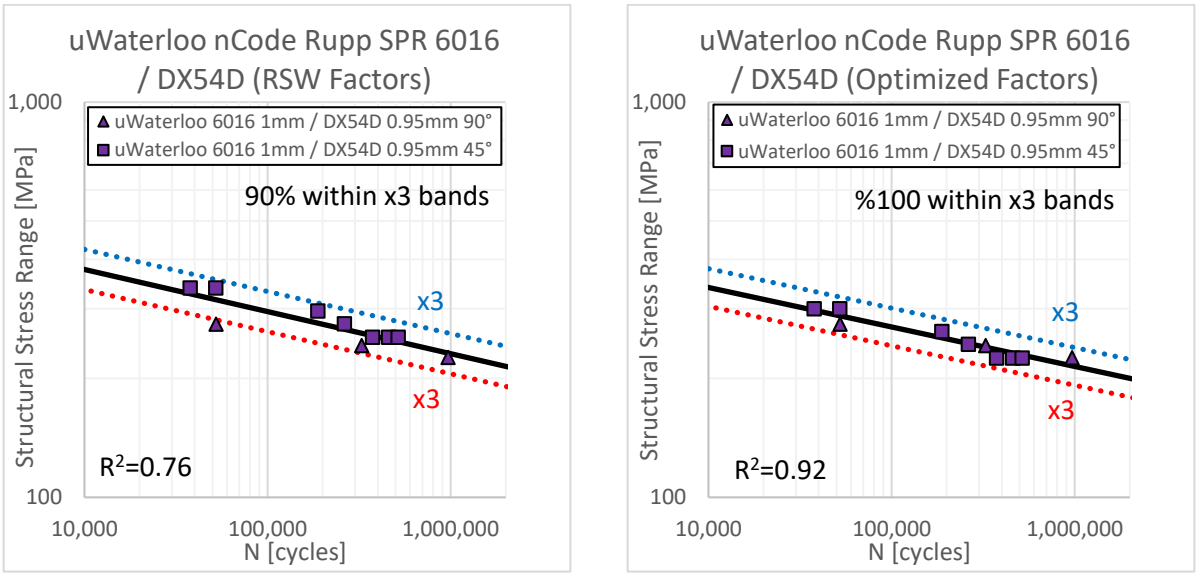

Figure 65: uWaterloo cross-tension SPR 6016 1mm by DX54D 0.95mm stress-life plot converted from Figure 51 load-life plot with nCode Rupp's model RSW factors (left) and GRG optimized factors (right)

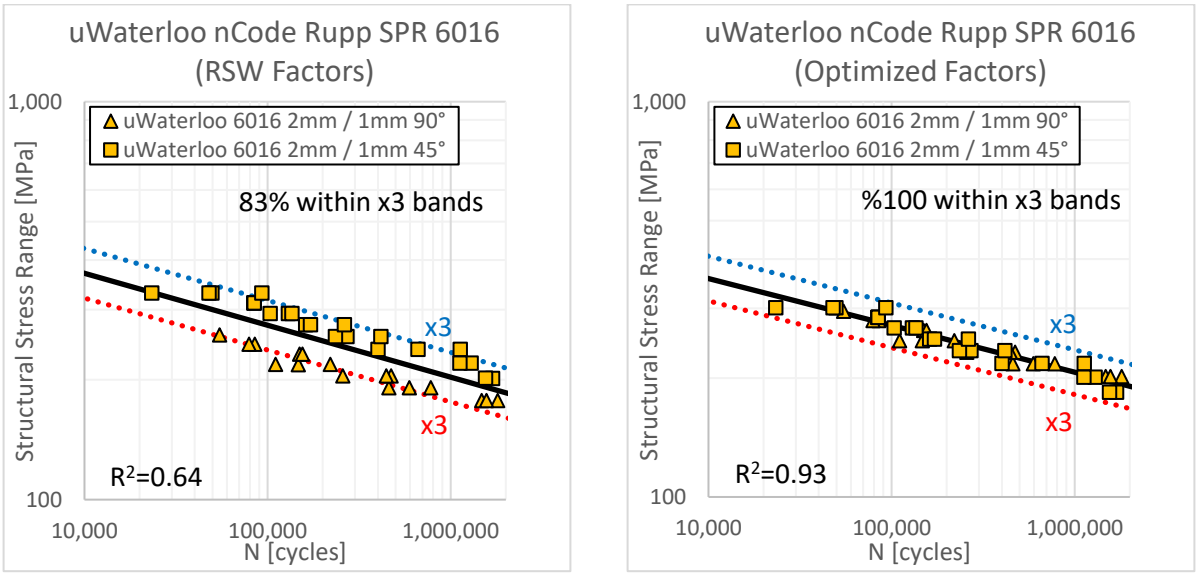

Figure 66: uWaterloo cross-tension SPR 6016 2mm by 1mm stress-life plot converted from Figure 33 load-life plot with nCode Rupp's model RSW factors (left) and GRG optimized factors (right)

Figure 65 (right) and *Figure 66 (right)* show Rupp's model performs well when converting uniaxial and biaxial loaded dissimilar material and thickness cross-tension SPR specimens from load-life to stress-life

with nCode aluminum RSW empirical factors from *Table 4*. Further collapse is achieved with GRG statistical optimization as shown in *Figure 65 (right)* and *Figure 66 (right)* where sum of squared residuals has been minimized resulting in an increased R^2 from 0.64 to 0.93 and 0.76 to 0.92. Optimization has resulted in all data points to be within x3 scatter bands.

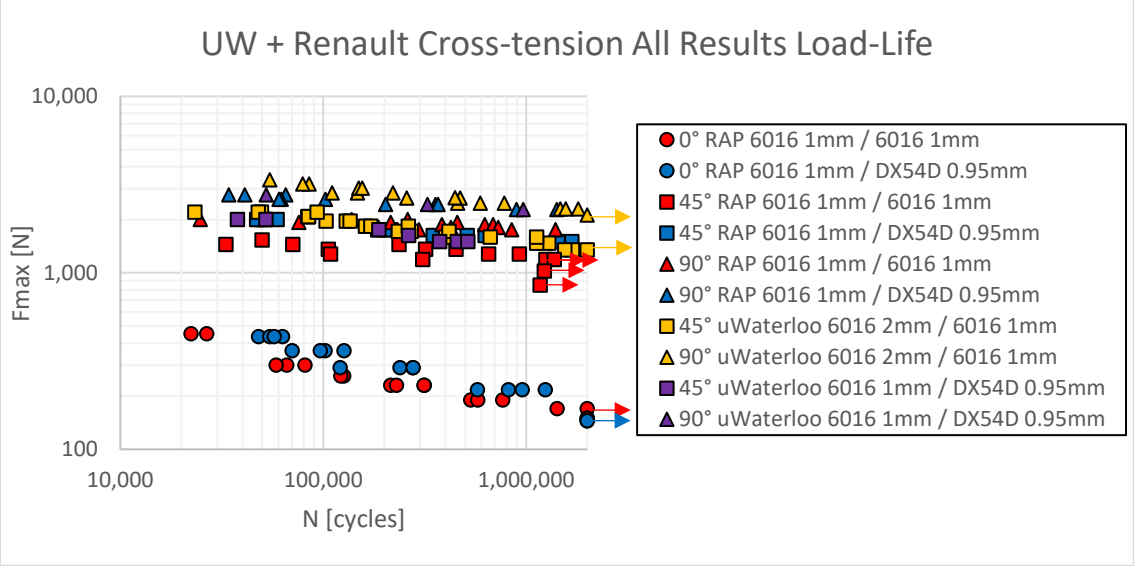

Figure 67: Renault Group and uWaterloo cross-tension SPR fatigue results, all data load-life plot

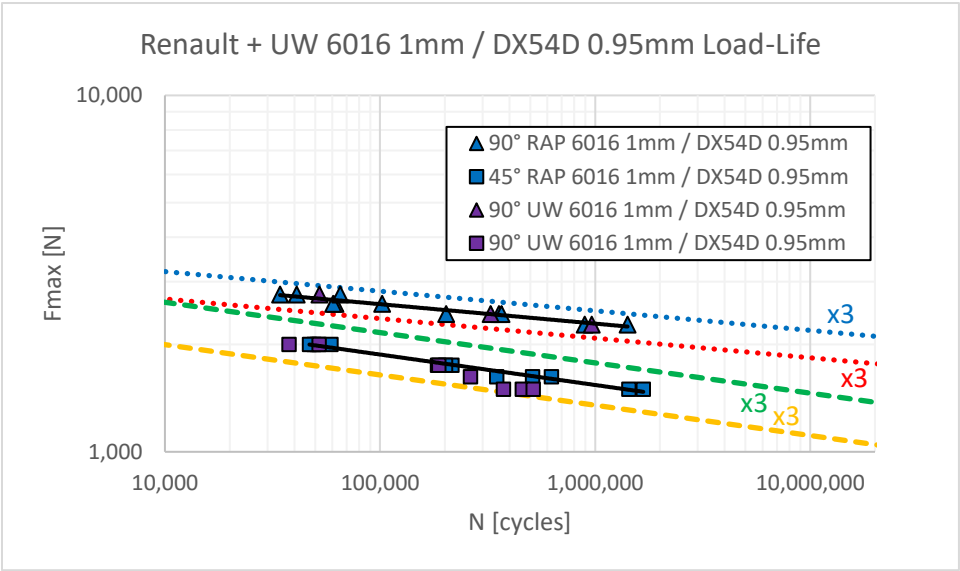

Figure 68: Renault Group and uWaterloo cross-tension SPR Al 6016 1mm / DX54D 0.95mm from Figure 67 load-life plot

Performance of Rupp's model with biaxially loaded SPR cross-tension joints is further validated by adding Renault Group cross-tension fatigue results where all tests were performed with established process

parameters described in Section 3.1.4. *Figure 69 (left)* and *Figure 70 (left)* show some improvement in data collapse when transferring from load-life to stress-life, however the R^2 values 0.17 and 0.37 are significantly lower than *Figure 65 (left)* and *Figure 66 (left)*. Significant improvement in collapse can be seen in *Figure 65 (left)* and *Figure 66 (left)* after GRG statistical optimization resulting in R^2 values of 0.65 and 0.66. *Figure 71* shows collapse of all specimen types performed by Renault Group and The University of Waterloo showing relatively low initial R^2 of 0.26 from initial Rupp's model collapse and good collapse performance after statistical optimization achieving R^2 of 0.61.

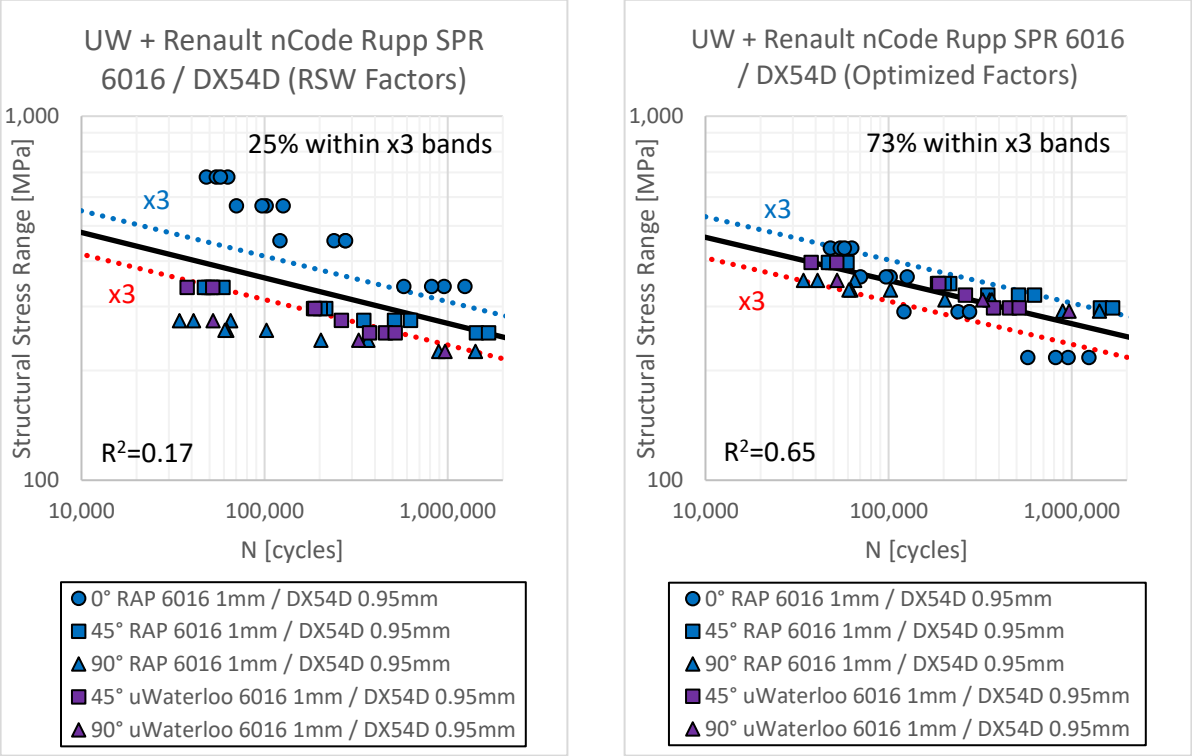

Figure 69: Renault Group and uWaterloo cross-tension SPR Al 6016 1mm / DX54D 0.95mm stress-life plot converted from Figure 67 load-life plot with nCode Rupp's model RSW factors (left) and GRG optimized factors (right)

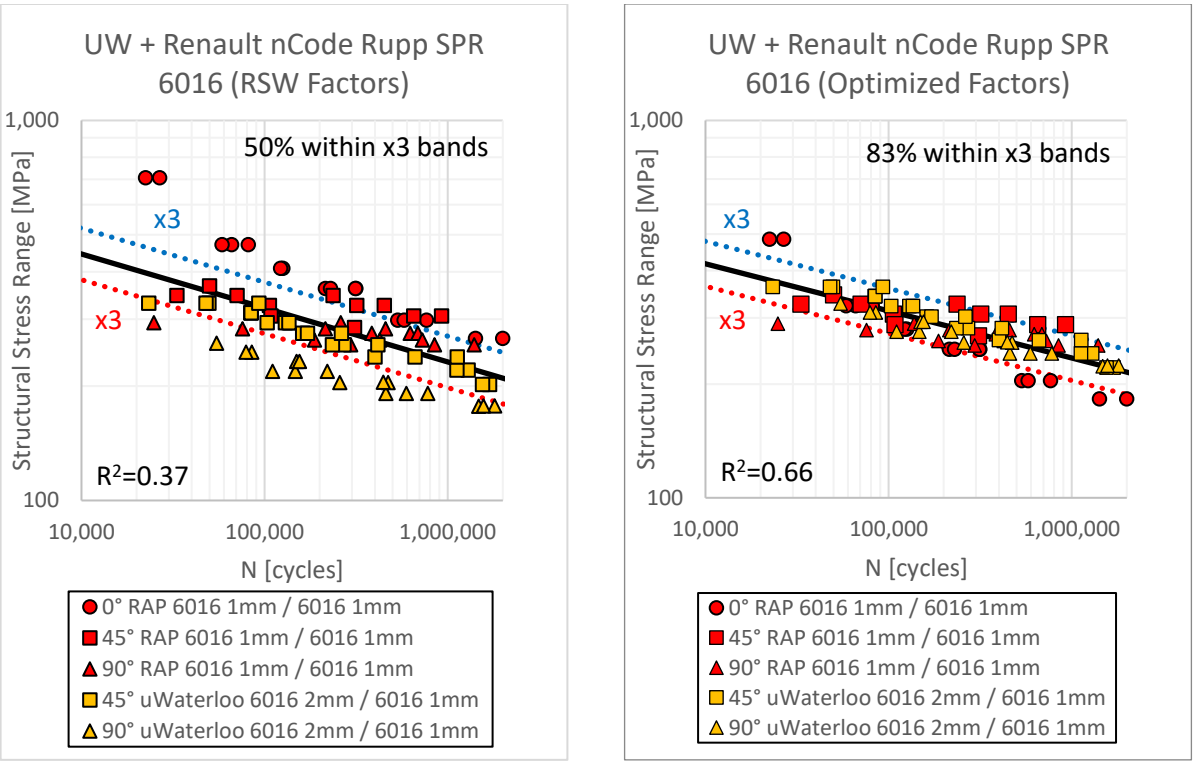

Figure 70: Renault Group and uWaterloo cross-tension SPR 6016 stress-life plot converted from Figure 67 load-life plot with nCode Rupp's model RSW factors (left) and GRG optimized factors (right)

Overall R^2 values in experimental results are lower in combined Renault Group and The University of Waterloo data pools. A contribution of lower R^2 value is high spread in two data sets in *Figure 67*, Renault Group 45° and 90° Al 6016 1mm by 1mm specimens, where fatigue results at certain load level replications vary by an order of magnitude. High initial spread in data *Figure 67* due to variation in specimen loading orientation, material and geometry also contribute to generally lower R^2 values. All specimen variations were tested at unique institutions except for Al 6016 1mm by DX54D 0.95mm specimen which has experimental results generated by both Renault Group and The University of Waterloo. *Figure 68* shows fatigue results for Al 6016 1mm by DX54D 0.95mm specimen from both institutions where 90° results at all load levels have minimal scatter, 45° results at high and mid load levels have minimal scatter, and 45° results at low load levels have relatively high scatter but still within x3 scatter bands.

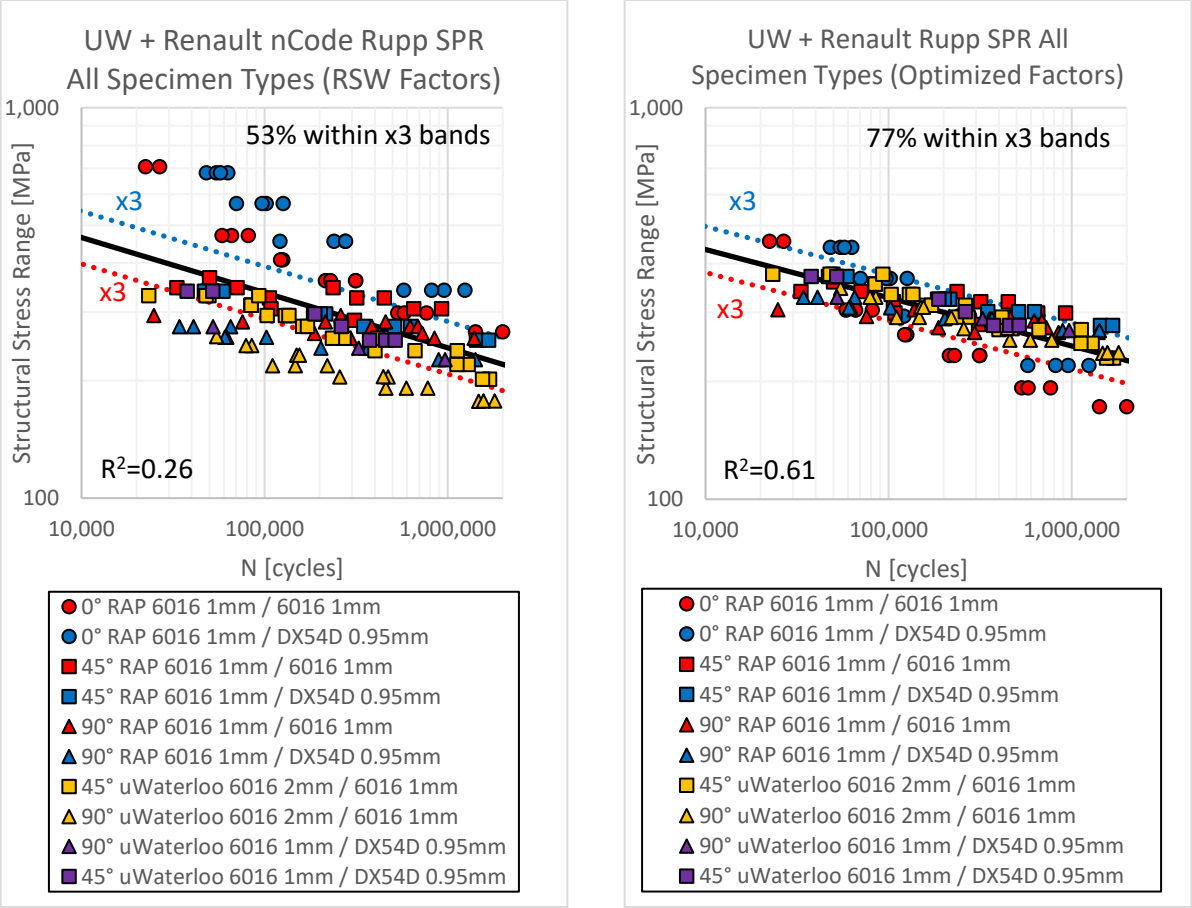

Figure 71: Renault Group and uWaterloo cross-tension all results SPR stress-life plot converted from Figure 67 load-life plot with nCode Rupp's model RSW factors (left) and GRG optimized factors (right)

9 updated nCode Rupp's model empirical factors for *Figure 65*, *Figure 66*, *Figure 69*, *Figure 70*, and *Figure 71* are shown in *Table 13* where bounds for all empirical factors are +/-1. While physical meaning behind values shown in *Table 13* are currently unknown some trends are noticeable. All three empirical factors related to thickness, TEFXY, TEMXY and TEFZ remain unchanged in optimization of all data sets. Minimal change is seen in diameter factors DEFXY and DEMXY while DEFZ shows more significant change in value especially in collapse of data obtained by The University of Waterloo. SFFXY, SFMXY and SFFZ factors stay reasonably consistent except for optimization of Al 6016 combined results and of complete experimental data collection stress-life plot. Two sets of empirical factor starting values were trialed with Al 6016 1mm by 1mm data sets used in *Figure 70*, with all 9 factors starting at either 1 or -1, and compared to nCode aluminum RSW factors post optimization *Table 14*. While all 3 sets of initial empirical factors optimized to the same R^2 value with accuracy of 4 decimal places, the empirical factors are considerably different, suggesting that empirical factors are not fully sensitive to physical properties and that multiple solutions exist. *Table 20* in Appendix B shows optimized empirical factors and R^2 values

for *Figure 65*, *Figure 66*, *Figure 69*, *Figure 70*, and *Figure 71* with optimization bounds at +/-10 and +/100. The converged R^2 is identical for all three limits in each set of optimized data, and empirical values for all +/-10 and +/-100 are identical, indicating bounds of +/-1 are adequate and the converged R^2 solution is unique. *Table 20* shows the most significant differences from bound change in SFFXY, DEMXY, SFFX and DEFX, minimal changes in DEFXY and SFMXY, and no change in TEFXY, TEMXY and TEFZ. In each specimen type tested at Renault Group and The University of Waterloo, failure occurs in a 1mm sheet which results $t = 1$ in equations (16-18). Since base $t = 1$ and TEFXY, TEMXY and TEFZ are exponents there is no mathematical way that nCode Rupp's model can optimize thickness empirical factors in this case.

Table 13: Original nCode aluminum RSW empirical factors and GRG optimized empirical factors for Figure 65, Figure 66, Figure 69, Figure 70, and Figure 71

	SFFXY	DEFXY	TEFXY	SFMXY	DEMXY	TEMXY	SFFZ	DEFZ	TEFZ
nCode Al RSW factors	0.40	0.50	-0.25	0.40	0.50	-0.25	1.00	0	1.00
UW 6016 1mm / DX54D 0.95mm	0.49	0.51	-0.25	0.48	0.35	-0.25	0.83	-0.34	1.00
UW 6016 2mm / 1mm	0.43	0.55	-0.25	0.43	0.51	-0.25	0.89	-0.41	1.00
UW + Renault 6016 1mm / DX54D 0.95mm	0.42	0.53	-0.25	0.45	0.59	-0.25	0.90	-0.15	1.00
UW + Renault 6016	0.61	0.60	-0.25	0.26	0.53	-0.25	0.93	-0.13	1.00
UW + Renault All Data	0.72	0.55	-0.25	0.26	0.54	-0.25	0.91	-0.15	1.00

Table 14: Post optimization empirical factors for Renault Al 6016 1mm by 1mm with different initial values and resulting in R^2 *=0.5707*

Initial empirical factor values	SFFXY	DEFXY	TEFXY	SFMXY	DEMXY	TEMXY	SFFZ	DEFZ	TEFZ
nCode Al RSW factors	0.40	0.51	-0.25	0.43	0.54	-0.25	0.96	-0.08	1.00
1	1.00	0.54	1.00	1.00	-0.11	1.00	1.00	-0.10	1.00
-1	0.14	-1.00	-1.00	0.97	0.29	-1.00	1.00	-0.10	-1.00

To observe Rupp's model master curve effectiveness for SPR fatigue life prediction, each data set from *Figure 67* was excluded from Rupp's model process and plotted against generated curves of all other data sets after optimization. *Figure 72* and *Figure 73* show Rupp's model under-predicts 0°, slightly over-predicts 90° and 45° is well predicted. Poor prediction of 0° indicate that Rupp's model is sensitive to quantity of data points included for calibration due to 0° being the smallest data set. *Figure 74* shows a replicate of the process used to generate master curves in *Figure 72* and *Figure 73* with all multiaxially loaded 45° data sets removed, where Rupp's model poorly predicts fatigue life. This indicates that while Rupp's model is capable of predicting uniaxially and multiaxially loaded SPR, multiaxially loaded experimental results are required for multiaxial fatigue life prediction.

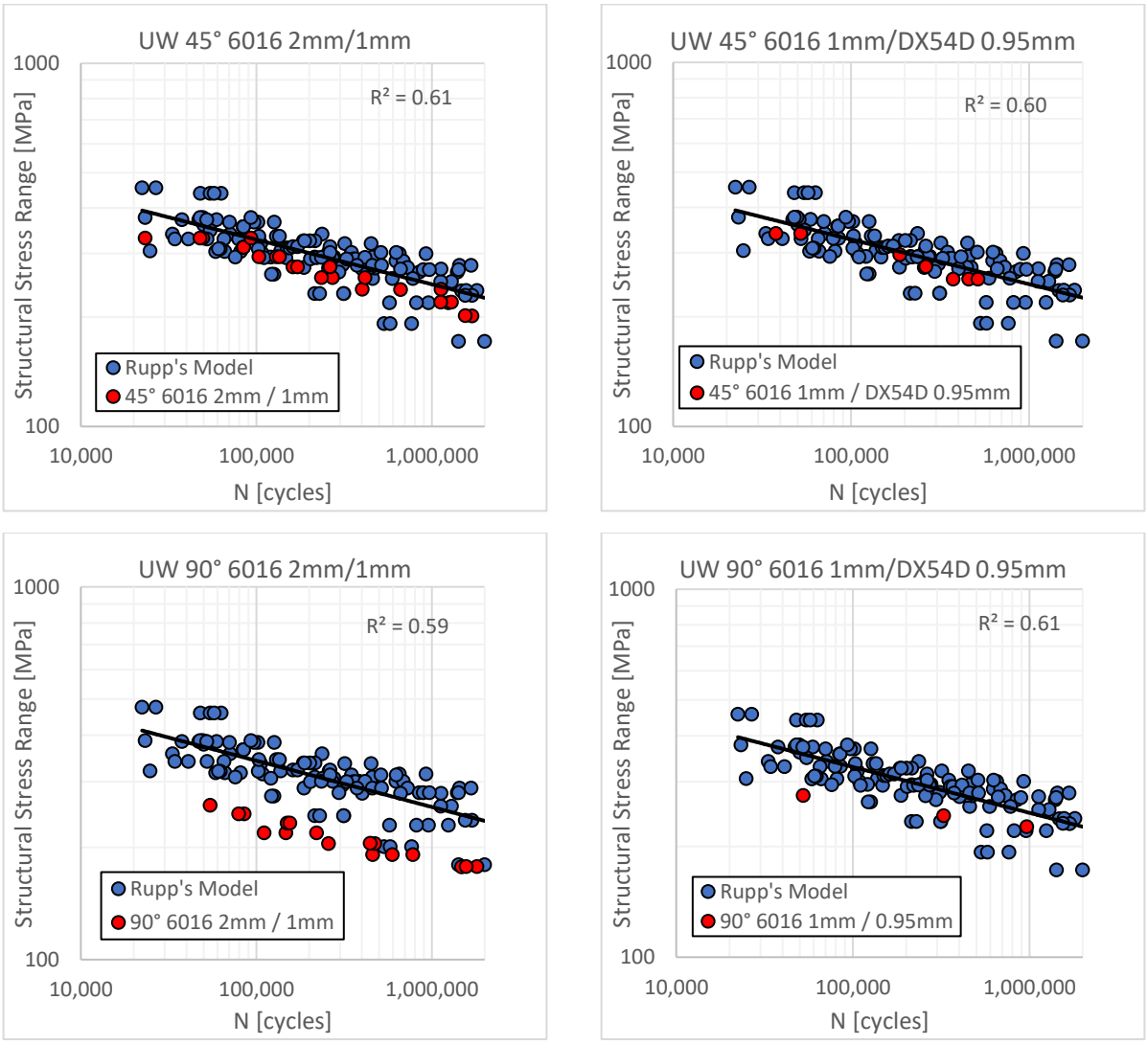

Figure 72: The University of Waterloo cross-tension SPR optimized Rupp's model master curves

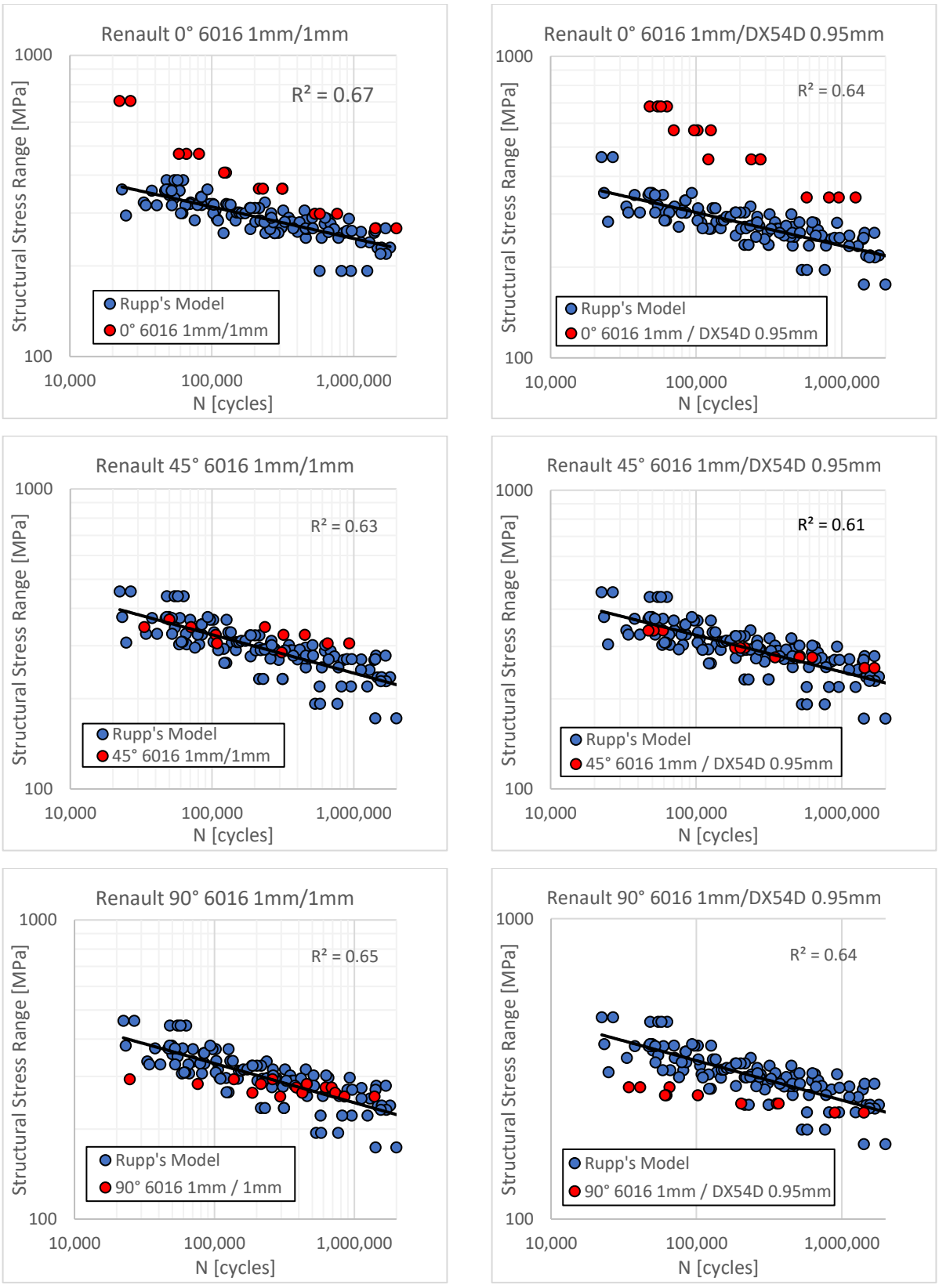

Figure 73: Renault cross-tension SPR optimized Rupp's model master curves

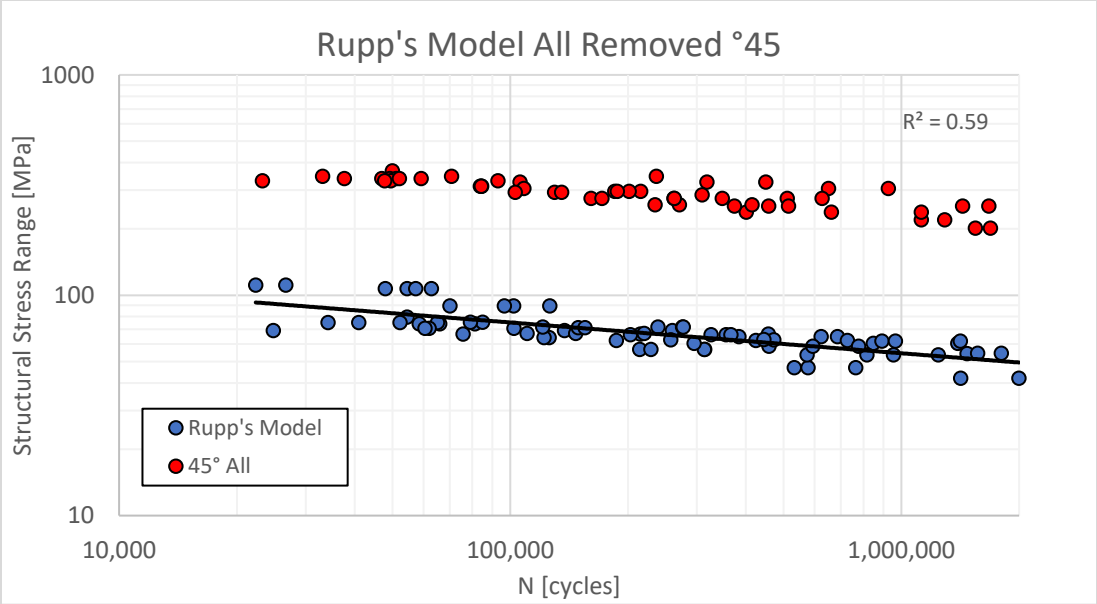

Figure 74:Cross-Tension SPR Optimized 0° and 90° Rupp's Model with 45° data

7. SPR and RSW Stress State Comparison

Although Section 4 and 6 show Rupp's model and statistical optimization are compatible with fatigue life prediction of SPR joints, some clear geometrical differences exist between RSW and SPR joints. Further investigation with finite elements into effects of geometrical differences may yield results to further improve data collapse.

7.1. Detailed Finite Element Pre-Processing

To understand stress state of SPR joints, two finite element models were created in ABAQUS to observe behavior. Geometry was derived from cross-sections of Al 6016 2mm by 2mm and Al 6016 1mm by 1mm cross-tension specimens *Figure 75*.

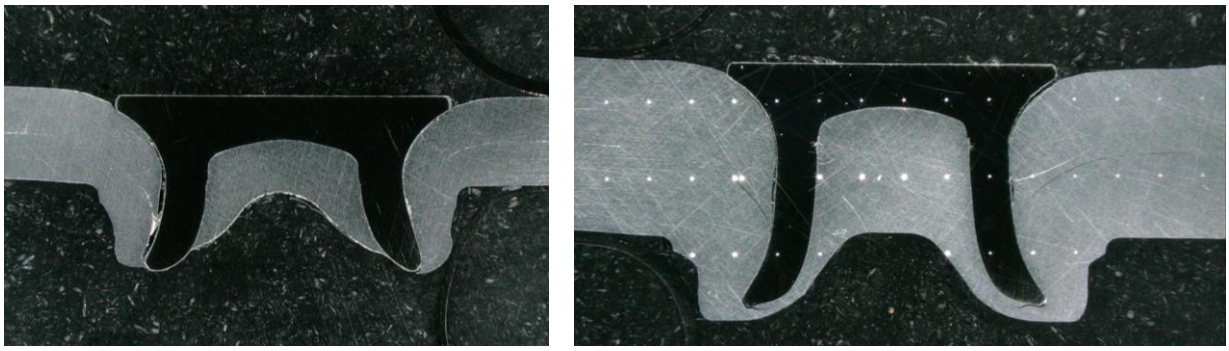

Figure 75: Cross-tension SPR cross-sections with geometry used for finite element modelling Al 6016 1mm by 1mm (left) and Al 6016 2mm by 2mm (right)

Three finite element models were created per specimen geometry for a total of six, where each specimen was modelled with 0°, 45°, and 90° loading directions. Material properties for all models were Modulus = 72 GPa and Poisson's Ratio = 0.3 for aluminum, and Young's Modulus = 190 GPa and Poisson's Ratio = 0.29 for steel. All contact interactions modeled with general contact with default normal behavior and penalty tangential behavior with friction coefficient $\mu = 0.2$ suggested by [17], [20], [22]. For computational efficiency, each model was created as half model with XSYMM boundary condition applied at cross-section surface to minimize model element count *Figure 76*. Clamped areas of clenched sheet are constrained in all degrees of freedom and reference point is constrained in all degrees of freedom excluding loading direction. Each model has applied load at reference point in corresponding direction to loading orientation with magnitude of 0.5N resulting in applied unit load due to half modelling technique. The reference point is then connected to clamped areas of pierced sheet with MPC beam connections. The Al 6016 1mm by 1mm model consists of 31,200 linear hexahedral elements (C3D8R) and Al 6016 2mm by 2mm model consists of 69,696 C3D8R elements.

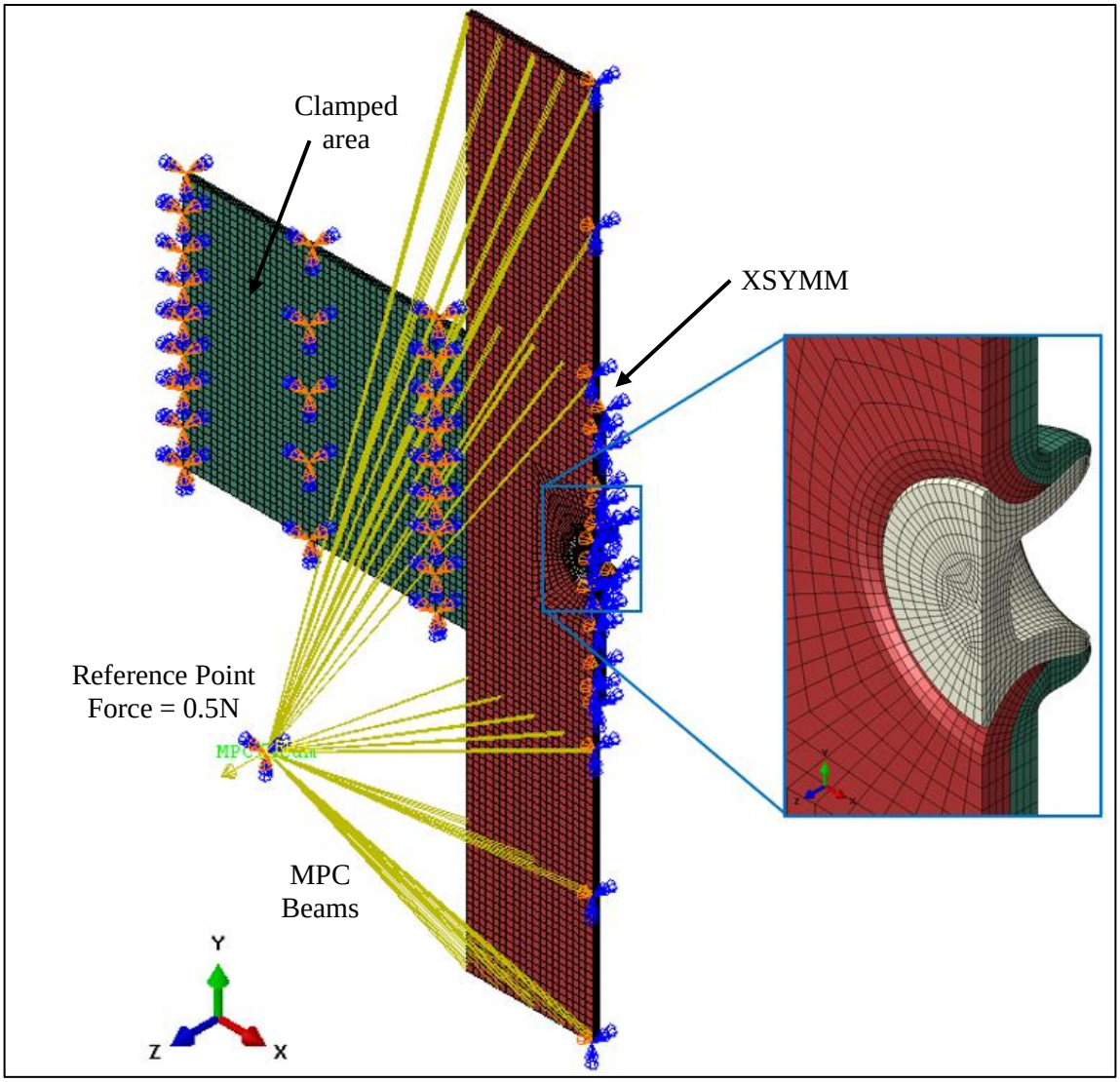

Figure 76: Isometric view of detailed finite element half model for Al 6016 1mm by 1mm SPR cross-tension joint under 0° loading with boundary conditions, applied load and joint center mesh details

7.2. Detailed Finite Element Post-Processing

Aside from mechanical interlocking differences between the RSW and SPR joints, geometrical differences exist causing difference in stress state between joining methods. Since Rupp's model fatigue life prediction method is based on analytical structural stress equations derived from RSW like geometry, this should be investigated for further understanding and optimization potential. A von Mises stress contour plot with expected deformation mode is shown in *Figure 77*. Note that captive volume of top sheet separated from main volume was removed from all models for computational efficiency. An initial comparison between stress and deformation states with and without this component showed negligible influence.

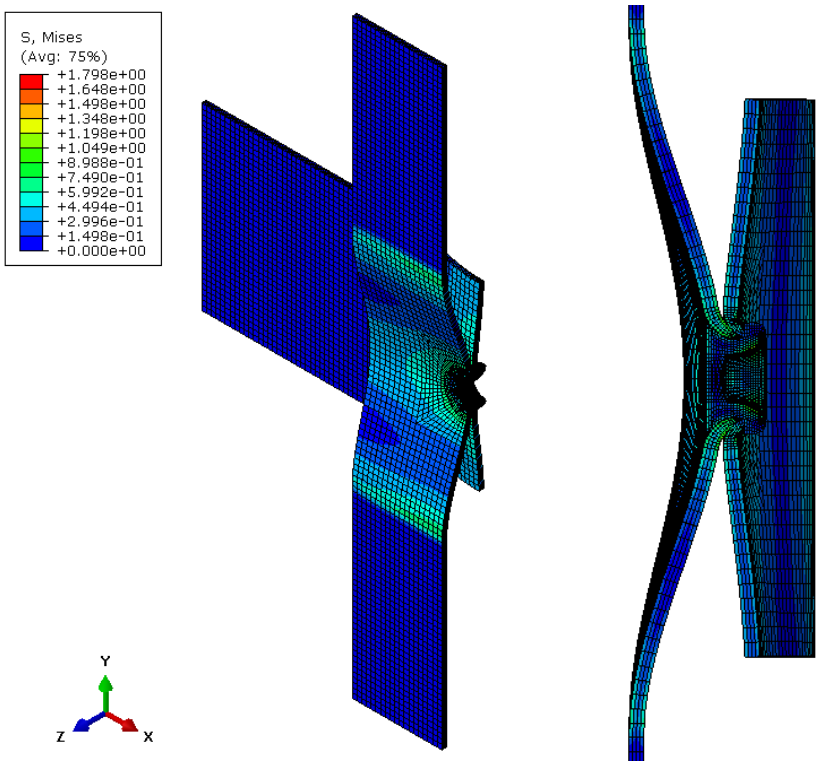

Figure 77: Mises stress contour plot of cross-tension 6016 1mm by 1mm detailed finite element half model 0° loading (deformation scale factor: 2,000) isometric view (left) and right view (right)

The pierced sheet of SPR joints flare inwards towards the next sheet due to the countersink of SPR, resulting in axisymmetric geometry where pierced sheet reduces in cross-sectional area terminating to a point at the pierced sheet inner edge. In 0° loading orientation the dominant mode of stress is bending due to F_z however, due to complex geometry some normal membrane stress may exist. Additionally, due to difference in radius of inner and outer curved surfaces of the pierced sheet formed protrusion, bending neutral axis is near but not exactly coincident with geometrical mid-point. To extract only normal bending stress values of the top sheet shown in *Figure 78 (left)* for comparison with equation (11), a plane near perpendicular to neutral axis and passes through a node of highest or lowest S22 stress magnitude, is used to generate a new coordinate system. S22 stress values are then transformed into the new coordinate system and extracted at either side of the pierced sheet at outermost fibers, where normal bending stresses are of highest magnitude. Membrane stress can then be calculated by averaging two extracted S22 values and bending stresses calculated by subtracting membrane stress from either extracted S22 nodal values. Due to axisymmetric stress state in 0° loaded cross-tension specimen, this process only needs to be performed for one side of the pierced sheet. This stress decomposition method is applied to the 90° model where bending and membrane stresses need to be isolated to compare with equations (10) and (12) where S22 contour plots

shown in *Figure 79* are for tension side of the joint. This procedure is replicated for the bottom compressive side.

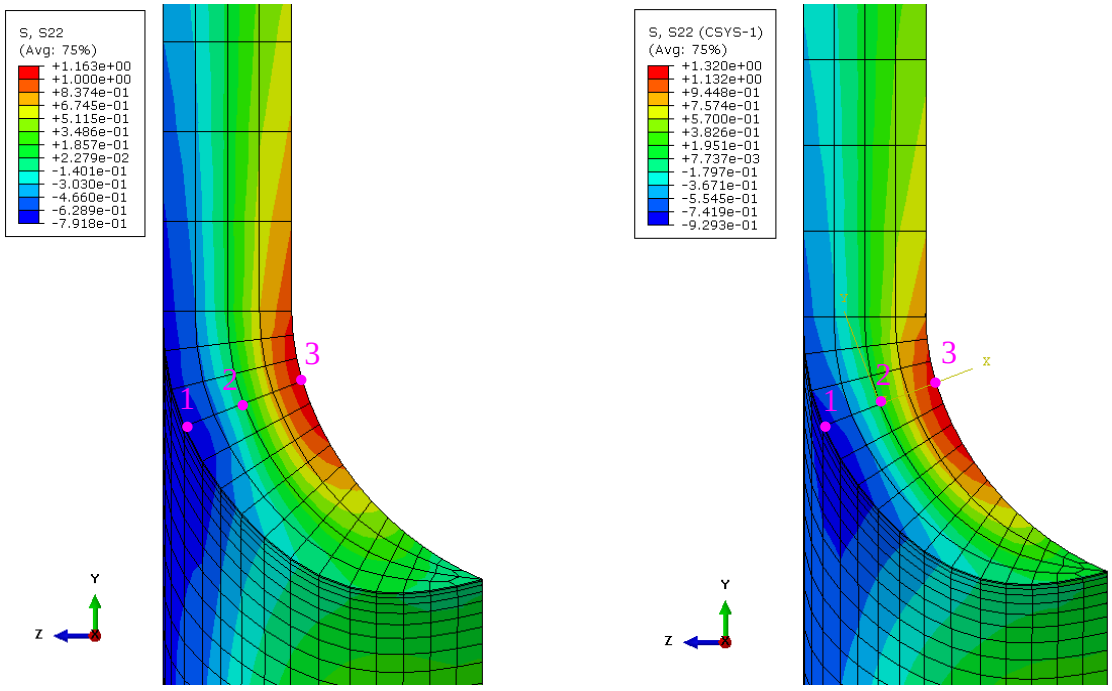

Figure 78: Global S22 contour plot of 0° top sheet from Figure 77 with 3 indicated nodes: node 2 on geometrical midpoint, and node 1 and node 3 at outermost fibers of sheet (left) and S22 contour plot transformed coordinate system where bending stresses are extracted at nodes 1 and 3 (right)

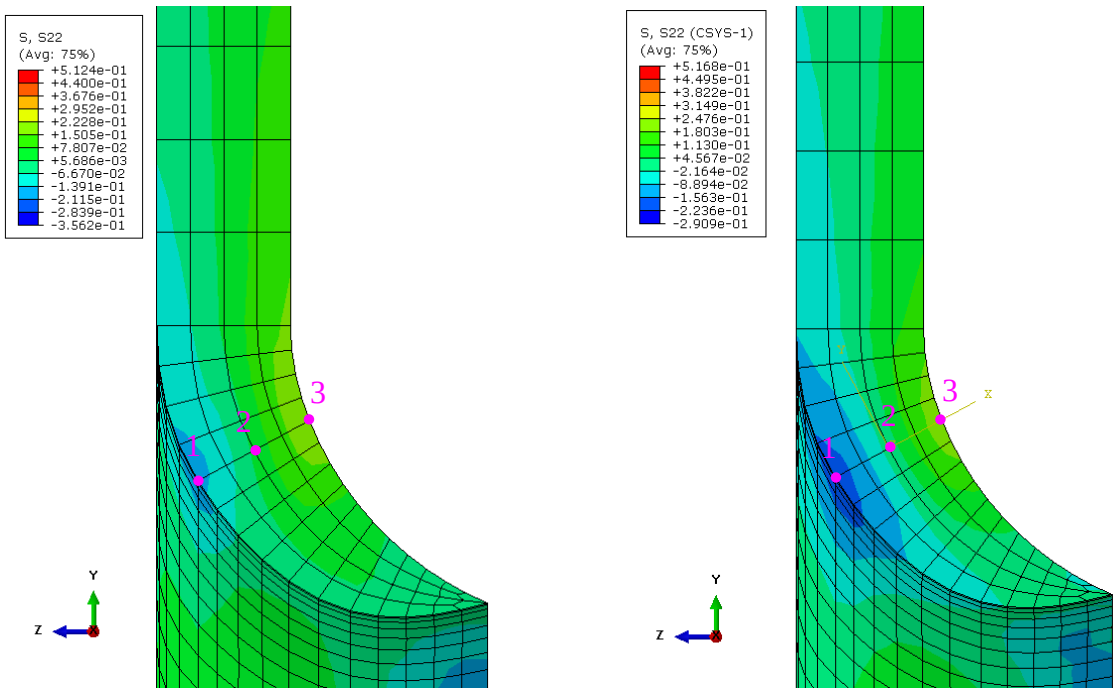

Figure 79: Global S22 contour plot of 90° top sheet from Al 6016 1mm by 1mm model with 3 indicated nodes: node 2 on geometrical midpoint, and node 1 and node 3 at outermost fibers of sheet (left) and S22 contour plot transformed coordinate system where bending stresses are extracted at nodes 1 and 3 (right)

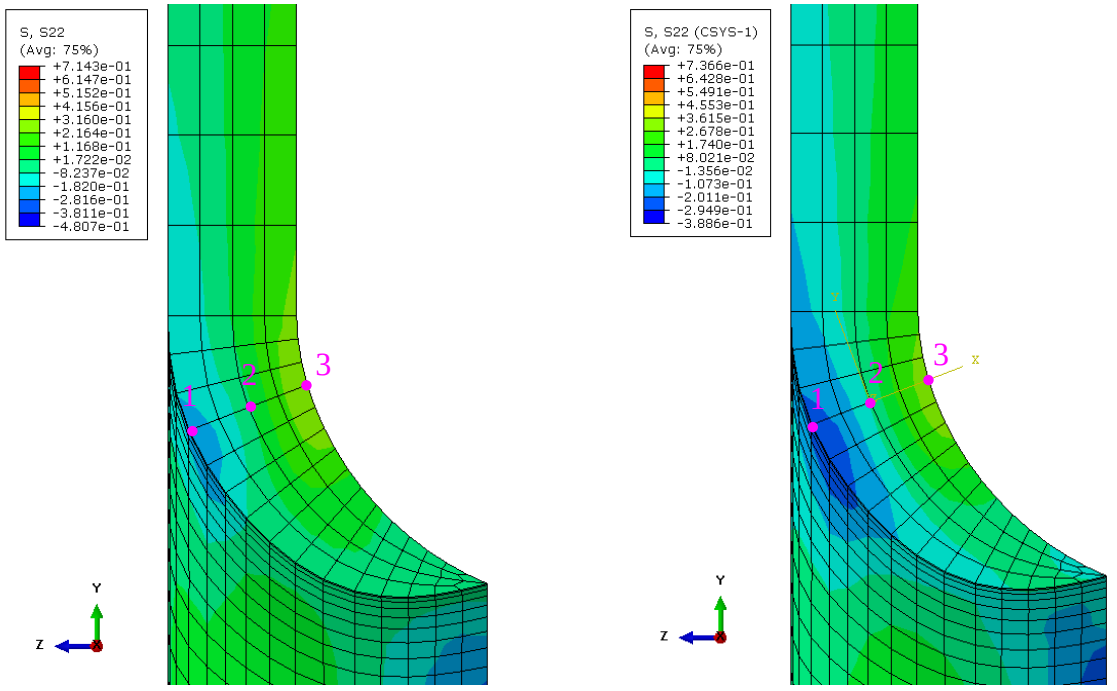

Figure 80: Global S22 contour plot of 45° top sheet from Al 6016 1mm by 1mm model with 3 indicated nodes: node 2 on geometrical midpoint, and node 1 and node 3 at outermost fibers of sheet (left) and S22 contour plot transformed coordinate system where bending stresses are extracted at nodes 1 and 3 (right)

Decomposition of 45° loaded joints is more complex since bending due to F_z and M_x are unique to 0° and 90° loading orientations respectively, however, are both present in 45° models due to biaxial loading. An attempt was made to isolate bending due to F_z and M_x by taking advantage of the mostly linear elastic modelling of 45° finite element models, where the only non-linearities are caused by contact. If effects of contact are negligible to joint stress state, stress values obtained from 0° and 90° models can be easily scaled linearly with respective force component from the 45° model. Membrane stress can be extracted directly from the 45° model with the same decomposition method used in 0° and 90° models *Figure 80*.

The decomposition method used for Al 6016 1mm by 1mm model has been replicated for Al 6016 2mm by 2mm sheet with all S22 contour plots and extracted data in Appendix C and Appendix D respectively. The simplified finite element model shown in *Figure 62* was replicated twice to reflect the geometry of Al 6016 1mm by 1mm and Al 6016 2mm by 2mm specimens shown in *Figure 75* to provide tractions for RSW analytical structural stress equations. The same material properties used in detailed models are used for respective joint components in simplified models. Since the purpose of this study is to observe differences in SPR numerical and RSW analytical stress values, two sets of 45° analytical structural stress values are provided due to lack of shell element F_z output and unusually high in-plane force values associated with 45° simplified models *Table 15*. One set of analytical structural stresses are calculated from exact forces and moments extracted from simplified 45° model's beam element, and the other being a set of stress values where F_y is divided by 2 and F_z calculated with static equilibrium. This can be done since sum of section forces along any set of deformable shell elements along the x direction equal to exactly half the probed F_y value at beam element end. All extracted forces for calculated analytical unit stress values are tabulated in *Table 15* and *Table 16*.

Table 15: Specimen material, geometries, and extracted unit traction values for simplified finite element model of Figure 75 specimens

Specimen	Sheet Material	t1, t2 [mm]	Load [N]	Fx [N]	Fy [N]	Fz [N]	Mx [Nmm]	My [Nmm]
0°	6016	1	1	0	0	1	0	0
45° (as extracted)	6016	1	1	0	1.397	0.0228	-0.7252	0
45° (decomposed)	6016	1	1	0	0.6985	0.7157	-0.7252	0
90°	6016	1	1	0	1	0	-0.5000	0
0°	6016	2	1	0	0	1	0	0
45° (as extracted)	6016	2	1	0	1.325	0.0888	-0.7252	0
45° (decomposed)	6016	2	1	0	0.6627	0.7515	-1.351	0
90°	6016	2	1	0	1	0	-1	0

Table 16: Unit stress values calculated from tractions and geometry in Table 15

Specimen	t1, t2 [mm]	σ(fx) [MPa]	σ(fy) [MPa]	σ(fz) [MPa]	σ(mx) [MPa]	σ(my) [MPa]	θ [°]	σsheet [MPa]
0°	1	0	0	1.744	0	0	0	1.744
45° (as extracted)	1	0	0.0556	0.0397	0.1697	0	90	0.2650
45° (as extracted)	1	0	-0.0556	0.0397	-0.1697	0	270	-0.1856
45° (decomposed)	1	0	0.0278	1.248	0.1697	0	90	1.446
45° (decomposed)	1	0	-0.0278	1.248	-0.1697	0	270	1.051
90°	1	0	0.0398	0	0.1170	0	90	0.1568
90°	1	0	-0.0398	0	-0.1170	0	270	-0.1568
0°	2	0	0	0.4360	0	0	0	0.4360
45° (as extracted)	2	0	0.0264	0.0387	0.0790	0	90	0.1297
45° (as extracted)	2	0	-0.0264	0.0387	-0.0790	0	270	-0.0600
45° (decomposed)	2	0	0.0132	0.3277	0.0790	0	90	0.4199
45° (decomposed)	2	0	-0.0132	0.3277	-0.0790	0	270	0.2354
90°	2	0	0.1989	0	0.0585	0	90	0.0706
90°	2	0	-0.1989	0	-0.0585	0	270	-0.0706

Table 17 and *Table 18* compare SPR numerical and RSW analytical stress values where 0° and 90° model numerical stresses were extracted directly from their respective finite element models, and 45° decomposed numerical stresses were extrapolated from 0° and 90° models. Due to asymmetry of stress state in 45° and 90° models, stresses were extracted from tension side at θ = 90° and from compression side at θ = 270°.

Table 17: Comparison of numerical stress values from SPR finite element and RSW analytical structural stress equations for Al 6016 1mm by 1mm SPR cross-tension top sheet

Specimen Orientation	σ [MPa]	270° (compression)			90° (tension)		
		SPR FEA	RSW Analytical	Ratio	SPR FEA	RSW Analytical	Ratio
0°	Membrane	0.2091	0	N/A	0.2083	0	N/A
	Bending (Fz)	1.071	1.744	**0.6143**	1.065	1.744	0.6107
	Bending (Mx)	0	0	N/A	0	0	N/A
45° (as extracted)	Membrane	-0.0681	-0.0556	1.224	0.0233	0.0556	0.4187
	Bending (Fz)	0.7027	0.0397	17.70	0.7944	0.0397	20.01
	Bending (Mx)	-0.1279	-0.1697	0.7536	0.1498	0.1697	0.8827
45° (decomposed)	Membrane	-0.0681	-0.0278	2.449	0.0233	0.0278	0.8373
	Bending (Fz)	0.7027	1.248	0.5630	0.7944	1.248	0.6364
	Bending (Mx)	-0.1279	-0.1697	0.7536	0.1498	0.1697	0.8827
90°	Membrane	-0.0527	-0.0398	**1.325**	0.0269	0.0398	0.6751
	Bending (Fz)	0	0	N/A	0	0	N/A
	Bending (Mx)	-0.1809	-0.1170	**1.546**	0.1972	0.1170	1.686

Table 18: Comparison of numerical stress values from SPR finite element and RSW analytical structural stress equations for Al 6016 2mm by 2mm SPR cross-tension top sheet

Specimen Orientation	σ [MPa]	270° (compression)			90° (tension)		
		SPR FEA	RSW Analytical	Ratio	SPR FEA	RSW Analytical	Ratio
0°	Membrane	0.0559	0	N/A	0.0559	0	N/A
	Bending (Fz)	0.2037	0.4360	**0.4671**	0.2037	0.4360	0.4671
	Bending (Mx)	0	0	N/A	0	0	N/A
45° (as extracted)	Membrane	-0.0361	-0.0264	1.370	0.0404	0.0264	1.534
	Bending (Fz)	0.1307	0.0387	3.377	0.1440	0.0387	3.721
	Bending (Mx)	-0.0459	-0.0790	0.5802	0.0713	0.0790	0.9029
45° (decomposed)	Membrane	-0.0361	-0.0132	2.740	0.0404	0.0132	3.067
	Bending (Fz)	0.1307	0.3277	0.3989	0.1440	0.3277	0.4395
	Bending (Mx)	-0.0459	-0.0790	0.5802	0.0713	0.0790	0.9029
90°	Membrane	-0.0369	-0.0199	**1.854**	0.0302	0.0199	1.520
	Bending (Fz)	0	0	N/A	0	0	N/A
	Bending (Mx)	-0.0718	-0.0585	**1.226**	0.1044	0.0585	1.785

For 0° comparison, it is seen that some membrane stress exists in SPR finite element model; however, this is uncaptured by any of structural stress equations used in Rupp's model. RSW bending stresses are expectedly higher due to different compliances in joining mechanisms. Mechanical interlock of SPR joint allows for slippage, while RSW joints have fused two separate masses of material, creating a less locally compliant joint. Stress ratios between SPR and RSW stresses are similar for 0° models when comparing 1mm and 2mm values, 0.6143 and 0.4671 respectively with an average value of 0.54.

For 90° models, bending stress is expectedly higher in pierced sheet due to out of plane deformation occurring during the SPR forming process, resulting a higher moment arm due to applied load. Stress ratios between tension and compression side of 2mm by 2mm joint are reasonably close; however, this is not true for the 1mm by 1mm joint where tensile side stress ratio 0.6751 is considerably smaller than compression side's ratio of 1.3251. This small ratio value is due to smaller membrane stress from SPR model, caused by slippage of a SPR joint's mechanical interlocking. Since this low membrane stress is not observed in the 2mm model, results suggest that sheet thickness has an effect on membrane stress in 90° loaded SPR joints. Stress ratios between SPR and RSW stresses are similar for both 90° models at compression side of joints, where membrane stress values average to 1.59 and average bending due to M_x ratios average to 1.39.

In 45° models, when tractions are left as extracted, the SPR model produces a much higher bending due to an unrealistically small F_z value. The ratios of 17.70 for compression and 20.01 tension side of 1mm models are exceptionally high, while the ratios of 3.3768 and 3.7205 for same respective side of 2mm models are relatively high. Membrane stress ratios in 2mm models are reasonably close to 90° stress ratios however, bending due to M_x are dissimilar. 45° with decomposed forces for RSW analytical stress values have closer values to numerical SPR stress values; however, are still relatively poor compared to 0° and 90° ratios. Due

to poor correlation of 45° numerical SPR and analytical RSW structural stress ratios compared with 0° and 90° ratios, correction factors were made by only averaging 0° and 90° models' ratios while 45° results were excluded.

Table 19: List of stress correction factors generated averaging stress ratio values in Table 17 and Table 18

Stress	Correction Factor
σ(Fz)	0.54
σ(Fy)	1.59
σ(Mx)	1.39

To see if stress correction factors have effect on Rupp's model, stress life plots in *Figure 70* were re-created by scaling unit forces and moments in *Table 12* with correction factors in *Table 19*. *Figure 81* shows results of scaling structural stresses where significant decline is collapse performance is observed. While the R^2 value decreased from 0.37 to 0.21, percentage of data within error bands remains similar. 45° and 90° data series remain reasonably clustered; however, 0° data series has been scaled to significantly increase data spread. It should be noted that after GRG optimization *Figure 81 (right)* shows identical R^2 value of 0.66 with 3% decrease in data within x3 scatter bands. To conclude although some trends can be observed with differences in numerical SPR and analytical RSW structural stress values, they do not improve data collapse for fatigue life prediction with Rupp's model and in fact drastically decrease initial collapse quality. However, this study has further validated the power of GRG optimization as *Figure 81 (right)* shows nearly identical collapse quality when compared to original GRG optimized stress-life plot with unscaled stresses.

Since it is expected for pierced sheet to fail when SPR joint sheets are of same thickness and materials, and due to complex and highly incompatible geometry of the bottom sheet, this study was only performed for the pierced sheet. It can be seen in *Figure 82* that although bending stress are present, they are influenced by the stress concentration factor caused by sharp notch effect in the formed protrusion. This will clearly add a factor that is not captured by analytical structural stresses used in Rupp's model therefore, the bottom sheet was excluded from this study.

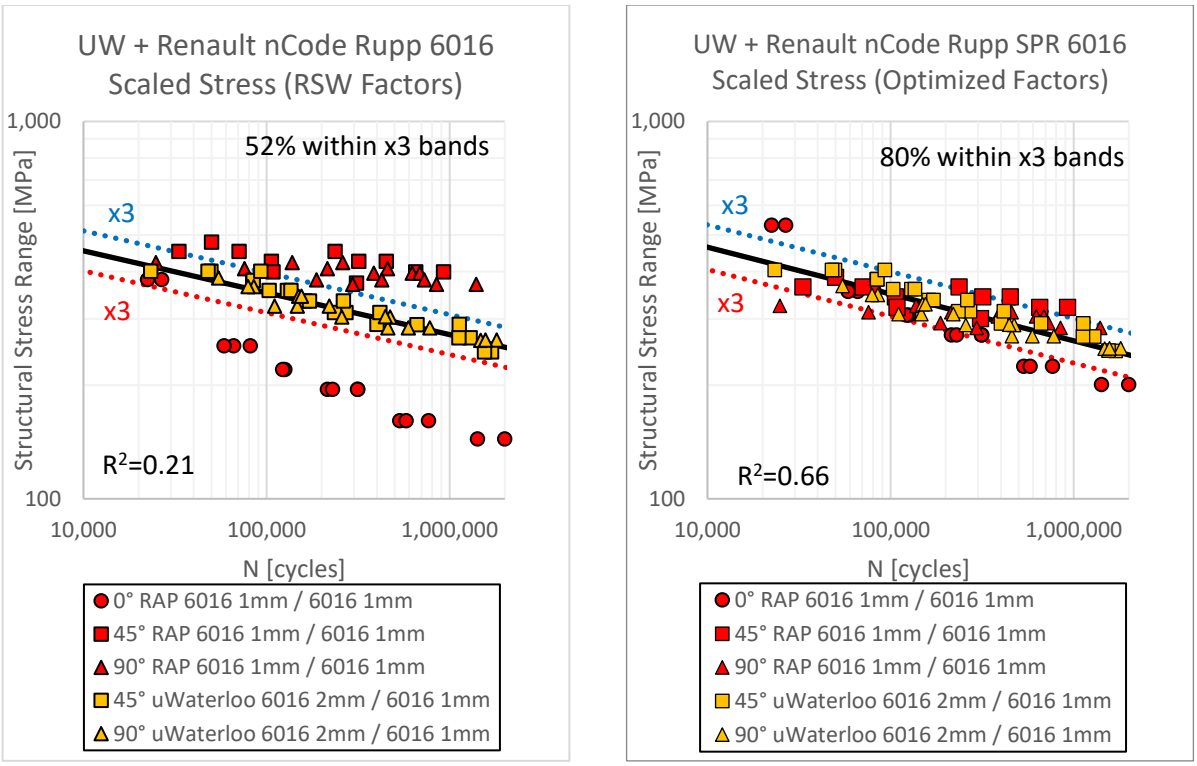

Figure 81: Renault Group and uWaterloo cross-tension SPR 6016 stress-life plots from Figure 70 with scaled stresses by Table 19 factors

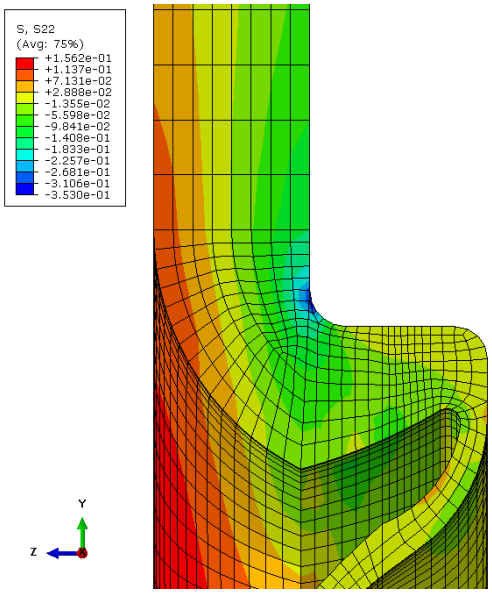

Figure 82: Global S22 contour plot of 0° clenched sheet from Al 6016 2mm by 2mm model

8. Conclusions

The objective of providing fatigue characterization of dissimilar thickness aluminum-aluminum and aluminum-steel SPR joints under uniaxial and multiaxial loading and to establish a life prediction model for durability assessment of SPR joints has been accomplished. Several contributions have been made by the work captured in this document and are as follows:

1. Compatibility and strong performance of nCode Rupp's model fatigue life prediction for uniaxially loaded SPR specimens in tensile-shear, coach-peel and tensile cross-tension configurations consisting of various sheet thicknesses and aluminum alloys has been verified. GRG optimization method further increases collapse performance of Rupp's model.
2. Quasistatic and fatigue experimental results of dissimilar thickness aluminum-aluminum and aluminum-steel SPR joints under uniaxial and multiaxial loading have been presented and discussed. SPR Al 6016 2mm by 1mm joints fail in clenched 1mm sheet with radial cracks approximately 90° offset from loading direction. Al 6016 1mm by DX54D fail in pierced aluminum sheet at the joint side consistently under tensile loading. In both specimen types multiaxially loaded specimens withstand lower load levels.
3. Presence and damage due to fretting of aluminum-to-aluminum SPR joints under cyclic loading has documented. Damage in fretting regions appear different depending on sheet thickness, Al 6016 1mm sheets show parallel, perpendicular, and oblique cracking in depth direction of sheet and Al 6016 2mm sheet show descaling or peeling damage at contact surfaces. Aluminum oxide ridges have developed at edge of fretting area near undamaged sheet.
4. Validation of nCode Rupp's model compatibility and performance for SPR fatigue life prediction with uniaxial and multiaxial loading has been achieved with experimental results performed by Renault Group and The University of Waterloo. Significant collapse performance can be further achieved with GRG optimization. This methodology is shown to work with similar and dissimilar material joints as well as simultaneous collapse of both.
5. Comparison between SPR and RSW stress states with detailed SPR finite element modelling yielded some trends; however, did not result in Rupp's model collapse performance increase. Differences between stress states of joints are explored for top sheet where differences in SPR and RSW joint compliance and geometry influence stress state.

9. Recommendations and Future Work

Despite display of nCode Rupp's model successful conversion from load-life to stress-life for fatigue life prediction of uniaxially and multiaxially loaded SPR specimens some recommendations can be made. Some Al 6016 1mm by DX54D specimens were erroneously manufactured with an SPR off-center by 1mm. Although effect on life seems minimal with obtained fatigue lives, difference in crack propagation is clear and can be further studied to understand if there is truly minimal effect in fatigue life. While occurrence of fretting is documented for aluminum-aluminum SPR joints, correlation between fretting and fatigue life is absent. No observations could be made for fretting of aluminum-steel SPR joints due to mechanical interlocking after cyclic loading. Potential investigation can occur if post-fatigue joints can be fully separated.

While performance of nCode Rupp's model is proven to be clearly effective, Rupp's model structural stress equations are not fully representative of the SPR geometry. Further understanding of physical differences and possible model modification is recommended for research and application purposes. Also, in Al 6016 2mm by 1mm specimens, clenched sheet failure mode was uncapturable by Rupp's model resulting in incorrect prediction of crack initiation location. Incorporating SPR geometry into a modified Rupp's model could potentially include prediction of these details. Modification of Rupp's model can also capture much more complex stress state of the clenched sheet in SPR joints, which is especially needed when clenched sheet is of weaker or thinner material than that of pierced sheets.

References

[1] F. Czerwinski, "Current Trends in Automotive Lightweighting Strategies," *Materials,* vol. 14, no. 21, 2021.

[2] D. Li, A. Chrysanthou, I. Patel and G. Williams, "Self-piercing riveting-a review," *The International Journal of Advanced Manufacturing Technology,* vol. 92, pp. 1777-1824, 2017.

[3] X. He, I. Pearson and K. Young, "Self-pierce riveting for sheet materials: State of the art," *Journal of Materials Processing Technology,* vol. 199, pp. 27-36, 2008.

[4] H. Jahed, B. Farshi, Hosseini and M, "Fatigue life prediction of autofrettage tubes using actual material behaviour," *International Journal of Pressure Vessels and Piping,* vol. 83, no. 10, pp. 749-755, 2006.

[5] A. Rupp, K. Storzel and V. Grubisic, "Computer Aided Dimensioning of Spot-Welded Automotive Sctuctures," *SAE Technical Paper Series 950711,* 1995.

[6] HBM, *DesignLife Theory Guide,* United Kingdom, 2013, pp. 209-226.

[7] S. Sunday, "Self-Piercing Rivets for Aluminum Components," *SAE Technical Paper Series 830526,* 1983.

[8] E. Partick and L. Sharp, "Joining Aluminum Auto Body Structure," *SAE Technical Paper Series 920282,* 1992.

[9] J. Mortimer, "Jaguar uses X350 car to pioneer use of self-piercing rivets," *Industrial Robot,* vol. 28, no. 3, pp. 192-198, 2001.

[10] K. Buchholz, ""Self-piercing rivets shoot for vehicle-lightweighting applications beyond aluminum"," sae.org, 31 08 2016. [Online]. Available: https://www.sae.org/news/2016/08/self-piercing-rivets-shoot-for-vehicle-lightweighting-applications-beyond-aluminum. [Accessed 10 04 2022].

[11] L. Han, M. Thorton and M. Shergold, "A comparison of the mechanical behaviour of self-piercing riveted and resistance spot welded aluminium sheets for the automotive industry," *Materials & Design,* vol. 31, no. 3, pp. 1457-1467, 2010.

[12] W. Yan, T. Mu, Z. Xie and C. Yu, "Experimental investigation of typical connections for fabricated cold-formed steel structures," *Advances in Structural Engineering,* vol. 22, pp. 141-155, 2019.

[13] Z. Su, P. Lin, W.-J. Lai and J. Pan, "Fatigue analyses of self-piercing rivets and clinch joints in lap-shear specimens of aluminum sheets," *International Journal of Fatigue,* vol. 72, pp. 53-65, 2015.

[14] G. Booth, C. Olivier and S. Westgate, "Self-Piercing Riveted Joints and Resistance Spot Welded Joints in Steel and Aluminium," *SAE Technical Paper Series 2000-01-2681,* 2000.

[15] W. Cai, P. Wang and W. Yang, "Assembly dimensional prediction for self-piercing riveted aluminum panels," *International Journal of Machine Tools and Manufacture,* vol. 45, no. 6, pp. 695-704, 2005.

[16] M. Fu and P. Mallick, "Fatigue of self-piercing riveted joints in aluminum alloy 6111," *International Journal of Fatigue,* vol. 25, p. 183–189, 2003.

[17] K. Iyer, S. Hu, F. Brittman, P. Wang, D. Hayden and S. Marin, "Fatigue of single- and double-rivet self-piercing riveted lap joints," *Fatigue & Fracture of Engineering Materials and Structures,* vol. 28, pp. 997-1007, 2005.

[18] X. Zhang, X. He, W. Wei, J. Lu and K. Zeng, "Fatigue characterization and crack propagation mechanism of self-piercing," *International Journal of Fatigue,* vol. 134, 2020.

[19] L. Huang, Y. Shi, H. Guo and X. Su, "Fatigue behavior and life prediction of self-piercing riveted joint," *International Journal of Fatigue,* vol. 88, pp. 96-110, 2016.

[20] L. Huang, H. Guo, Y. Shi, S. Huang and X. Su, "Fatigue behavior and modeling of self-piercing riveted joints," *International Journal of Fatigue,* vol. 100, pp. 274-284, 2017.

[21] S. K. Khanna, X. Long, S. Krishnamoorthy and N. H. Agrawal, "Fatigue properties and failure characterization of self-piercing riveted 6111 aluminum sheet joints," *Science and Technology of Welding and Joining,* vol. 11, no. 5, pp. 544-549, 2006.

[22] S.-H. Kang and H.-K. Kim, "Fatigue strength evaluation of self-piercing riveted Al-5052 joints under different specimen configurations," *International Journal of Fatigue,* vol. 80, pp. 58-68, 2015.

[23] X. Sun, E. Stephens and M. Khaleel, "Fatigue behaviors of self-piercing rivets joining similar," *International Journal of Fatigue,* vol. 29, pp. 370-386, 2007.

[24] L. Han, A. Chrysanthou, K. W. Young and J. M. O'sullivan, "Characterization of fretting fatigue in self-piercing rivted alumin alloy sheets," *Fatigue & Fracture of Engineering Materials and Structures,* vol. 29, no. 8, pp. 646-654, 2006.

[25] L. Zhao, X. He, B. Xing, Y. Lu, F. Gu and A. Ball, "Influence of sheet thickness on fatigue behavior and fretting of self-piercing riveted joints in aluminum alloy 5052," *Materials and Design,* vol. 87, pp. 1010-1017, 2015.

[26] Y. Chen, L. Han, A. Chrysanthou and J. O'sullivan, "Fretting wear in self-piercing riveted aluminium alloy sheet," *Wear,* vol. 225, pp. 1463-1470, 2003.

[27] L. Huang, J. Bonnen, J. Lasecki, H. Guo and X. Su, "Fatigue and fretting of mixed metal self-piercing riveted joint," *International Journal of Fatigue,* vol. 83, pp. 230-239, 2016.

[28] G. Du, Y. Xing and X. Li, "Fatigue properties of self-piercing riveted multi-rivet joints in steel and aluminum sheets," *Materialwiss. Werkstofftech.,* vol. 50, p. 1495–1502, 2019.

[29] S. Zhang, "Stress intensities at spot welds," *International Journal of Fracture,* vol. 88, no. 2, pp. 167-185, 1997.

[30] A. Blows, "Development of a CAE Method to Predict the Fatigue Life of Aluminium Panels Joined by Self Piercing Rivets," in *The 8th UK Altair Technology Conference*, 2013.

[31] H. Rao, J. Kang, G. Huff and K. Avery, "Impact of specimen configuration on fatigue properties of self-piercing riveted aluminum to carbon fiber reinforced polymer composite," *International Journal of Fatigue,* vol. 113, pp. 11-22, 2018.

[32] H. Rao, J. Kang, G. Huff and K. Avery, "Structural Stress Method to Evaluate Fatigue Structural Stress Method to Evaluate Fatigue Self-Piercing Riveted Joints," *Metals,* vol. 9, 2019.

[33] A. Cox and J. Hong, "Fatigue Evaluation Procedure Development for Self-Piercing Riveted Joints Using the Battelle Structural Stress Method," *SAE Technical Paper 2016-01-0384,* 2016.

[34] H. Kang, X. Wu, A. Khosrovaneh and Z. Li, "Data Processing Procedure for Fatigue Life Prediction of Spot-Welded Joints Using a Structural Stress Method," in *Fatigue and Fracture Test Planning, Test Data Acquisitions and Analysis*, ASTM International, 2017, pp. 198-211.

[35] G. Gabriele and K. Ragsdell, "The Generalized Reduced Gradient Method: A Reliable Tool for Optimal Design," *Journal of Engineering for Industry,* pp. 394-400, 1977.

[36] S. Rao, Engineering Optimization, Hoboken, New Jersey: John Wiley & Sons, Inc., 2009, pp. 412-422.

[37] P. Bouchard, T. Laurent and L. Tollier, "Numerical modeling of self-pierce riveting—From riveting process modeling down to structural analysis," *Journal of Materials Processing Technology,* vol. 202, pp. 290-300, 2008.

[38] M. Noban, H. Jahed, S. Winkler and A. Ince, "Fatigue characterization and modeling of 30CrNiMo8HH under multiaxial loading," *Materials Science and Engineering: A,* vol. 528, no. 6, pp. 2484-2494, 2011.

[39] M. Noban, H. Jahed, E. Ibrahim and A. Ince, "Load path sensitivity and fatigue life estimation of 30CrNiMo8HH," *International Journal of Fatigue,* vol. 37, pp. 123-133, 2012.

[40] A. Roostaei and H. Jahed, "Multiaxial cyclic behaviour and fatigue modelling of AM30 Mg alloy extrusion," *International Journal of Fatigue,* vol. 97, pp. 150-161, 2017.

[41] S. B. Behravesh, H. Jahed and S. Lambert, "Characterization of magnesium spot welds under tensile and cyclic loadings," *Materials & Design,* vol. 32, no. 10, pp. 4890-4900, 2011.

[42] S. B. Behravesh, H. Jahed and S. Lambert, "Fatigue characterization and modeling of AZ31B magnesium alloy spot-welds," *International Journal of Fatigue,* vol. 64, pp. 1-13, 2014.

[43] A. Gryguć, S. B. Behravesh, S. K. Shaha, H. Jahed, M. Wells, B. Williams and X. Su, "Multiaxial cyclic behaviour of extruded and forged AZ80 Mg alloy," *International Journal of Fatigue,* vol. 127, pp. 324-337, 2019.

[44] W. C. Young, R. G. Budynas and A. M. Sadegh, Roark's Formulas for Stress and Strain, McGraw Hill, 2012.

[45] J. J. Bonnen, H. Agrawal, M. A. Amaya, J. M. Iyengar, H. Kang, A. K. Khosrovaneh, T. M. Link, H. Shih, M. Walp and B. Yan, "Fatigue of Advanced High Strength Steel Spot-Welds," *SAE Technical Paper Series*, 2006.

Appendices

Appendix A – Simplified Finite Element Models for Rupp's Model for Section 6

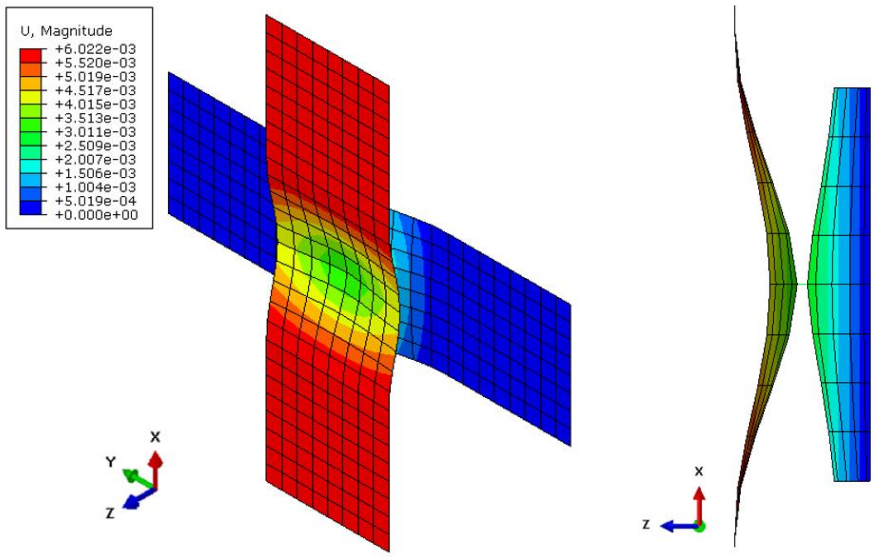

Figure 83: Displacement contour plot of cross-tension 6016 1mm by 1mm simplified finite element model 0° loading (deformation scale factor: 2,000) isometric view (left) and right view (right)

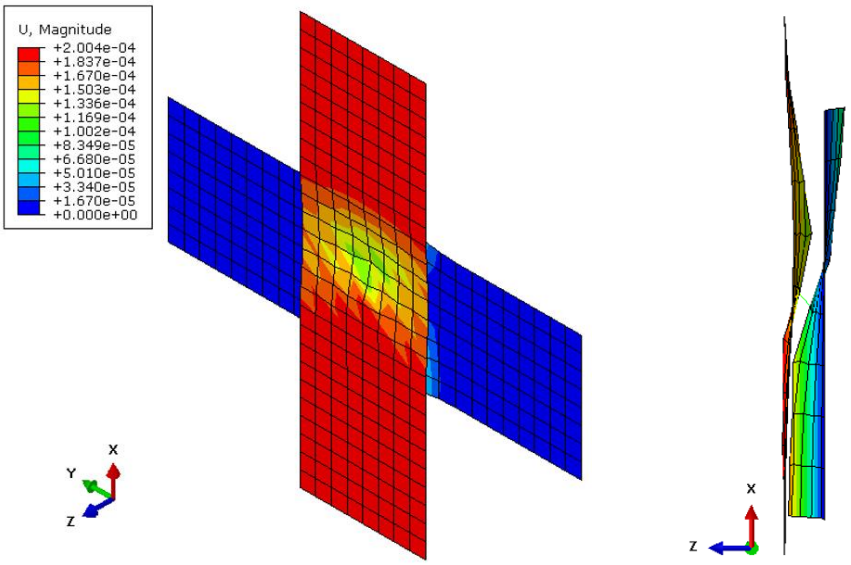

Figure 84: Displacement contour plot of cross-tension 6016 1mm by 1mm simplified finite element model 45° loading (deformation scale factor: 20,000) isometric view (left) and right view (right)

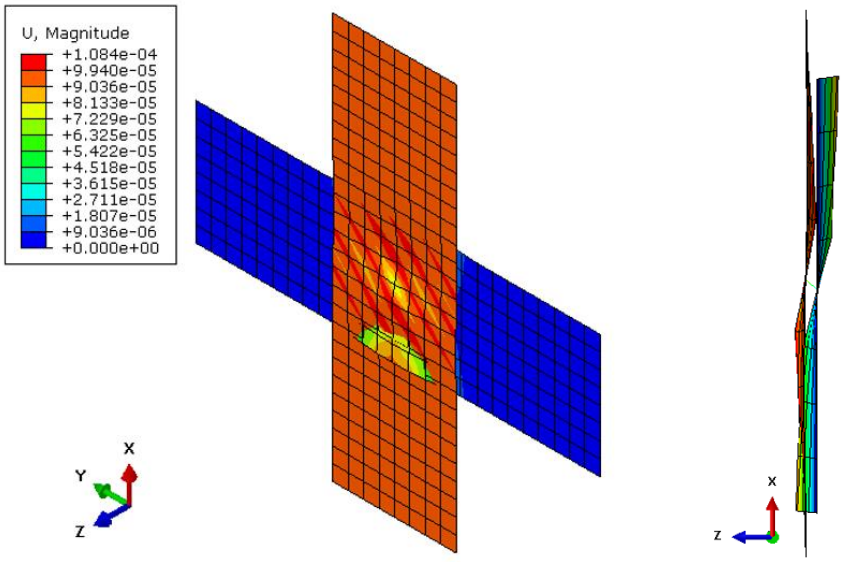

Figure 85: Displacement contour plot of cross-tension 6016 1mm by 1mm simplified finite element model 90° loading (deformation scale factor: 20,000) isometric view (left) and right view (right)

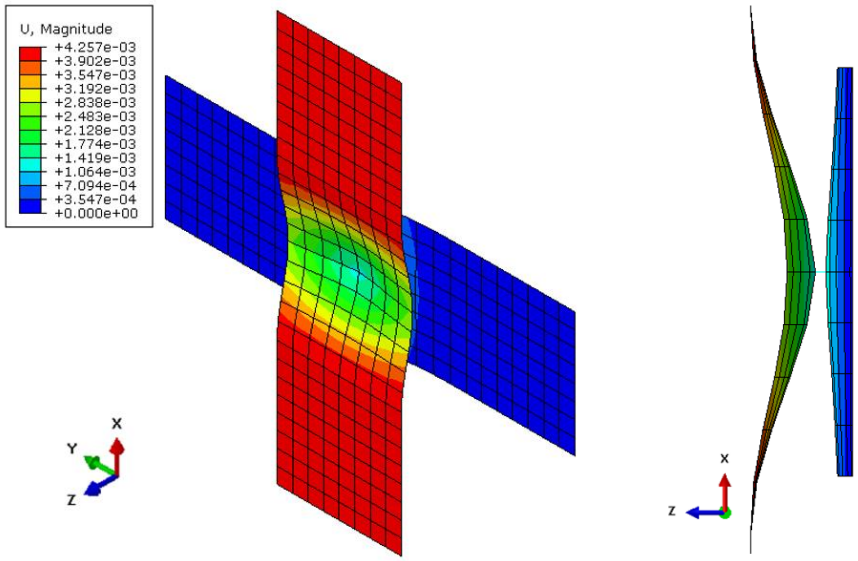

Figure 86: Displacement contour plot of cross-tension 6016 1mm by DX54D 0.95mm simplified finite element model 0° loading (deformation scale factor: 2,000) isometric view (left) and right view (right)

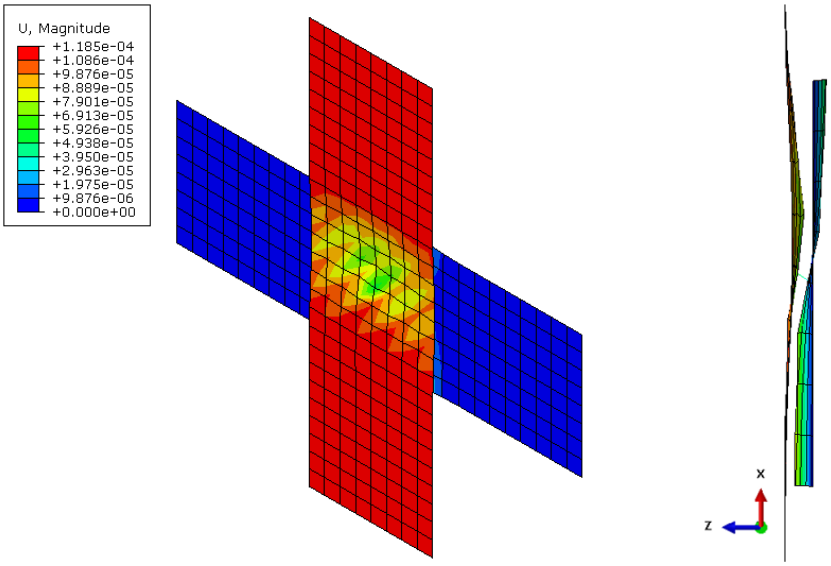

Figure 87: Displacement contour plot of cross-tension 6016 1mm by DX54D 0.95mm simplified finite element model 45° loading (deformation scale factor: 2,000) isometric view (left) and right view (right)

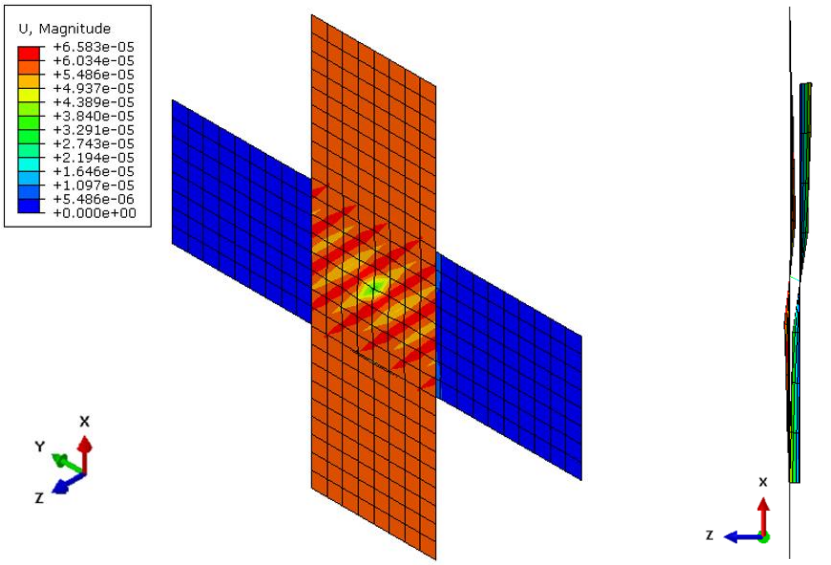

Figure 88: Displacement contour plot of cross-tension 6016 1mm by DX54D 0.95mm simplified finite element model 90° loading (deformation scale factor: 2,000) isometric view (left) and right view (right)

Appendix B – GRG Optimized Empirical Factors for Section 6

Table 20: GRG optimized factors with +1/-1 bounds from Figure 65 (right), Figure 66 (right), Figure 69 (right), Figure 70 (right), and Figure 71 (right), +10/-10 bound values, and +100/-100 bound values

UW Al 6016 1mm / DX54D 0.95mm										
Bounds	SFFXY	DEFXY	TEFXY	SFMXY	DEMXY	TEMXY	SFFZ	DEFZ	TEFZ	R^2
1/-1	0.4950	0.5112	-0.2500	0.4793	0.3473	-0.2500	0.8319	-0.3398	1.000	0.9109
10/-10	0.3633	0.4832	-0.2500	0.4398	0.4882	-0.2500	0.4052	-0.0275	1.000	0.9109
100/-100	0.3633	0.4832	-0.2500	0.4398	0.4882	-0.2500	0.4052	-0.0275	1.000	0.9109

UW Al 6016 2mm / 1mm										
Bounds	SFFXY	DEFXY	TEFXY	SFMXY	DEMXY	TEMXY	SFFZ	DEFZ	TEFZ	R^2
1/-1	0.4304	0.5473	-0.2500	0.4254	0.5071	-0.2500	0.8948	-0.4051	1.000	0.9264
10/-10	0.7067	0.4774	-0.2500	0.3815	0.3391	-0.2500	0.3267	0.0324	1.000	0.9264
100/-100	0.7067	0.4774	-0.2500	0.3815	0.3391	-0.2500	0.3267	0.0324	1.000	0.9264

RAP + UW Al 6016 1mm / DX54D 0.95mm										
Bounds	SFFXY	DEFXY	TEFXY	SFMXY	DEMXY	TEMXY	SFFZ	DEFZ	TEFZ	R^2
1/-1	0.4195	0.5310	-0.2500	0.4518	0.5883	-0.2500	0.8967	-0.1479	1.000	0.6512
10/-10	0.7566	0.5268	-0.2500	0.5622	0.2949	-0.2500	0.9810	-0.1869	1.000	0.6512
100/-100	0.7566	0.5268	-0.2500	0.5622	0.2949	-0.2500	0.9810	-0.1869	1.000	0.6512

RAP + UW Al 6016										
Bounds	SFFXY	DEFXY	TEFXY	SFMXY	DEMXY	TEMXY	SFFZ	DEFZ	TEFZ	R^2
1/-1	0.5741	0.6261	-0.2500	0.2424	0.5496	-0.2500	0.9816	-0.1559	1.000	0.6637
10/-10	0.6064	0.6024	-0.2500	0.2555	0.5267	-0.2500	0.9267	-0.1309	1.000	0.6637
100/-100	0.6064	0.6024	-0.2500	0.2555	0.5267	-0.2500	0.9267	-0.1309	1.000	0.6637

All										
Bounds	SFFXY	DEFXY	TEFXY	SFMXY	DEMXY	TEMXY	SFFZ	DEFZ	TEFZ	R^2
1/-1	0.7664	0.5291	-0.2500	0.3186	0.4470	-0.2500	0.9040	-0.1475	1.000	0.6128
10/-10	0.8262	0.4964	-0.2500	0.3056	0.4651	-0.2500	0.8769	-0.1342	1.000	0.6128
100/-100	0.8262	0.4964	-0.2500	0.3056	0.4651	-0.2500	0.8769	-0.1342	1.000	0.6128

Appendix C – Detailed Finite Element Model S22 Contour Plots for Section 7.2

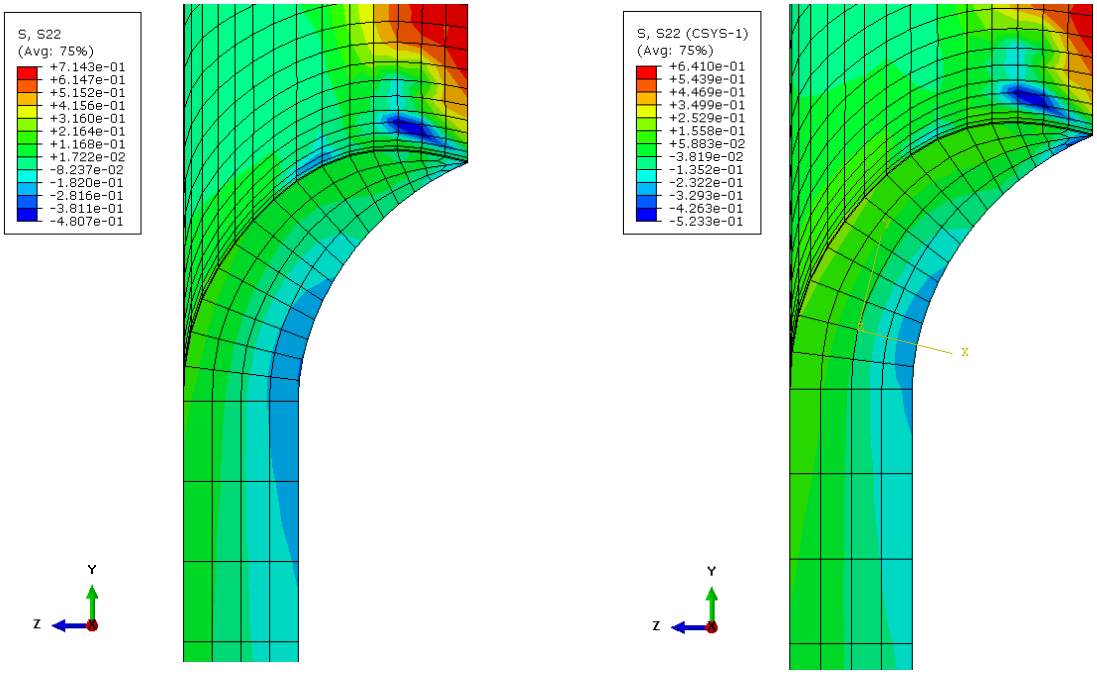

Figure 89: Global S22 contour plot of 45° top sheet compression side from Al 6016 1mm by 1mm model (left) and S22 contour plot transformed coordinate system (right)

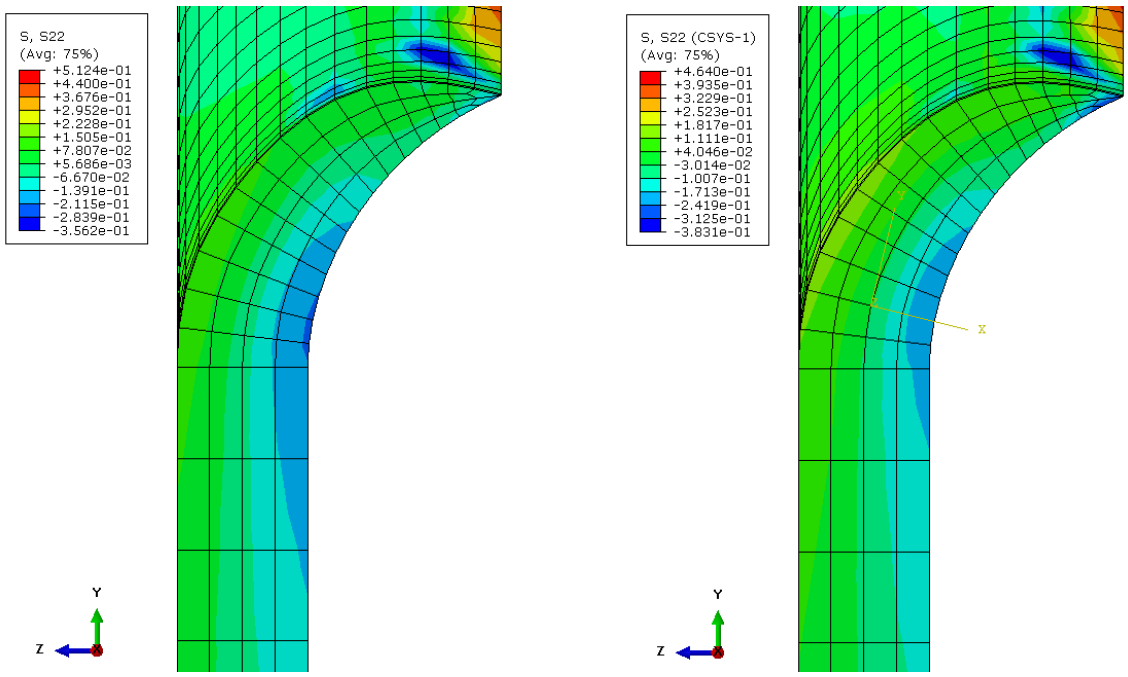

Figure 90: Global S22 contour plot of 90° top sheet compression side from Al 6016 1mm by 1mm model (left) and S22 contour plot transformed coordinate system (right)

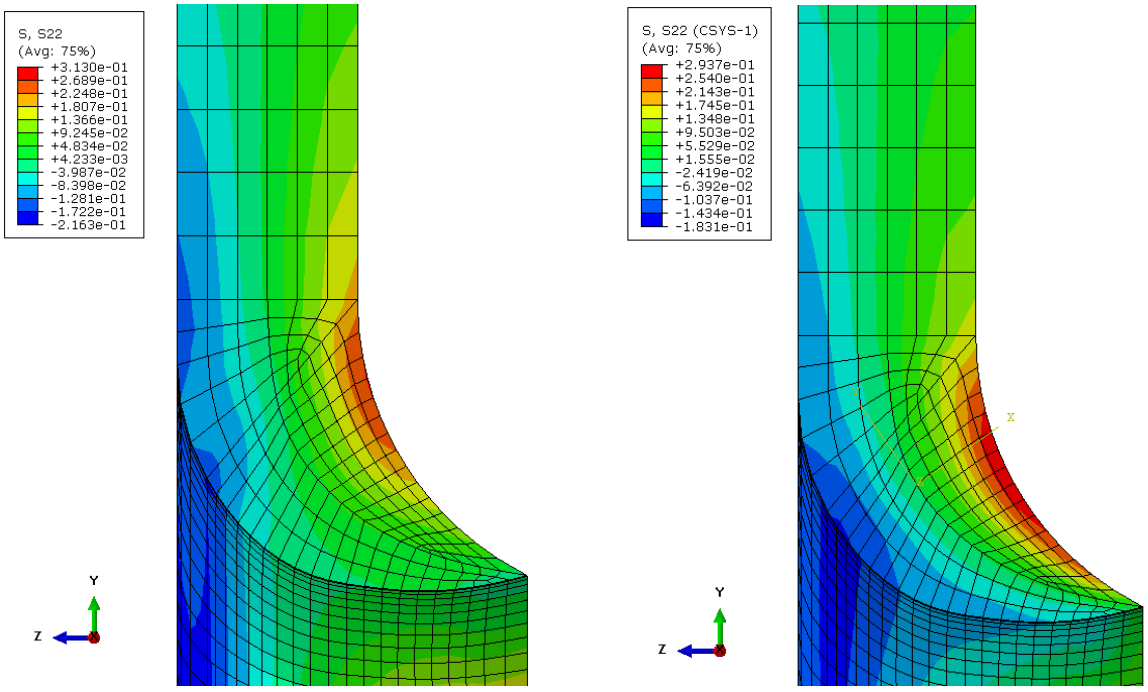

Figure 91: Global S22 contour plot of 0° top sheet from Al 6016 2mm by 2mm model (left) and S22 contour plot transformed coordinate system (right)

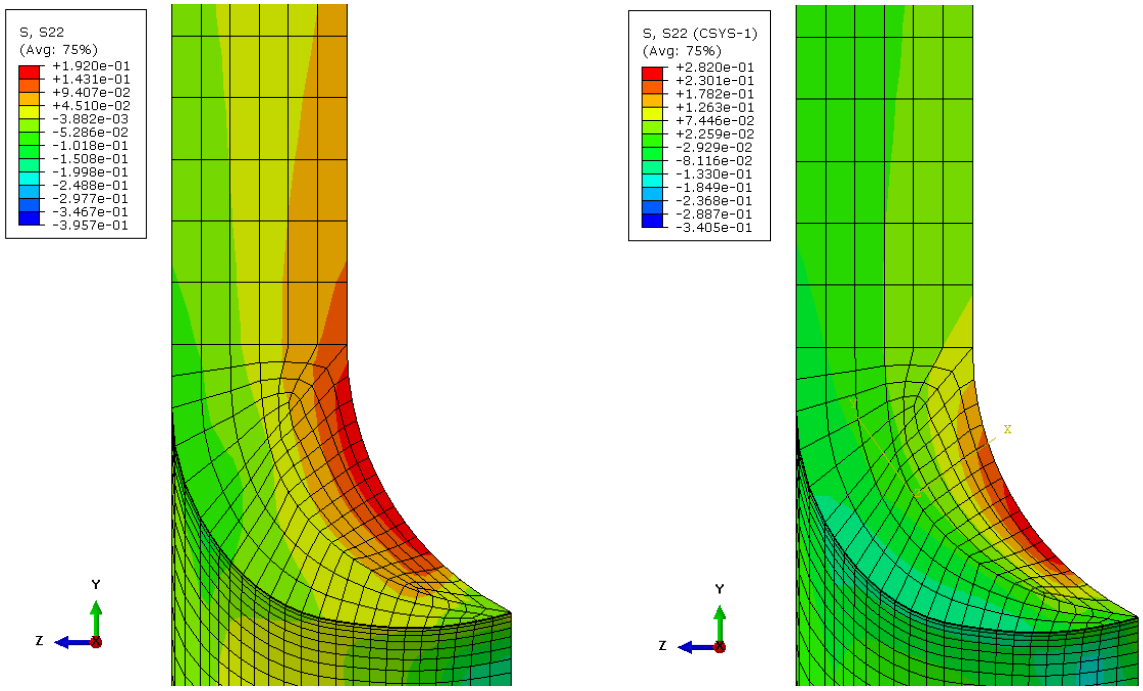

Figure 92: Global S22 contour plot of 45° top sheet compression side from Al 6016 2mm by 2mm model (left) and S22 contour plot transformed coordinate system (right)

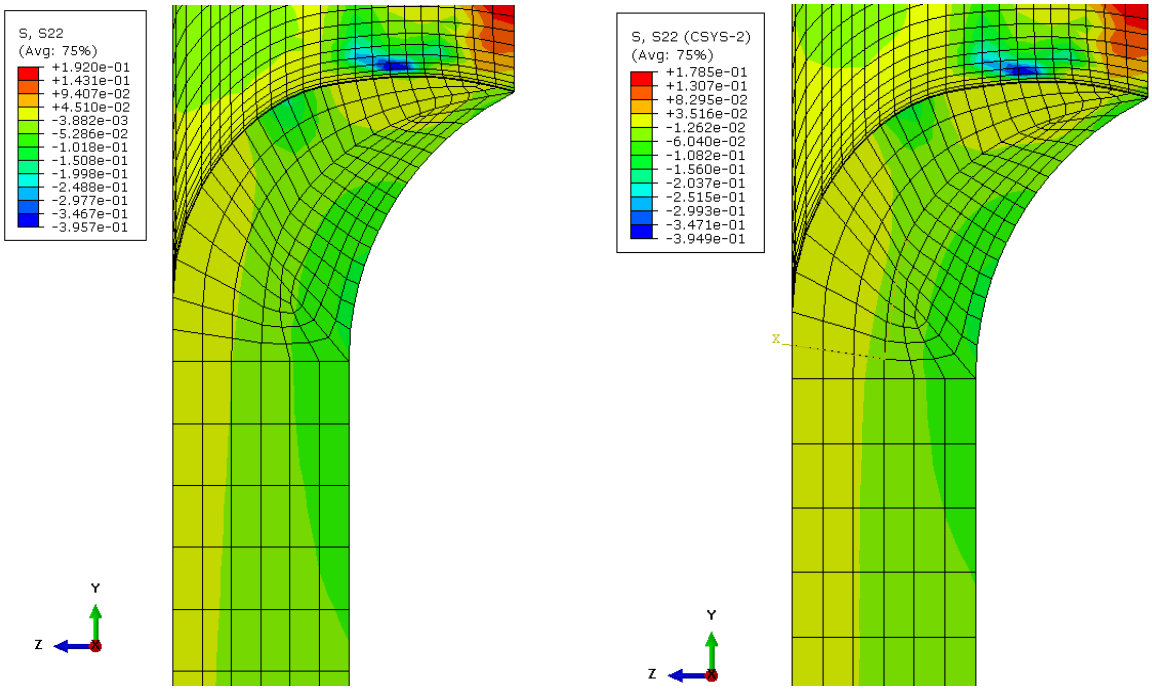

Figure 93: Global S22 contour plot of 45° top sheet tension side from Al 6016 2mm by 2mm model (left) and S22 contour plot transformed coordinate system (right)

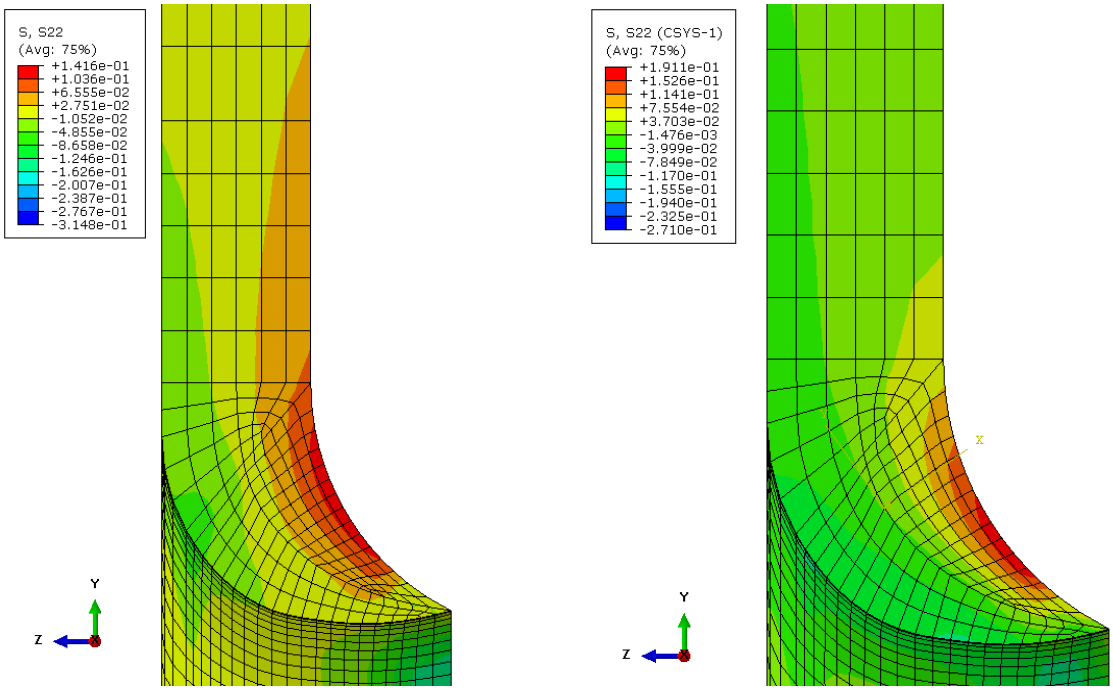

Figure 94: Global S22 contour plot of 90° top sheet compression side from Al 6016 2mm by 2mm model (left) and S22 contour plot transformed coordinate system (right)

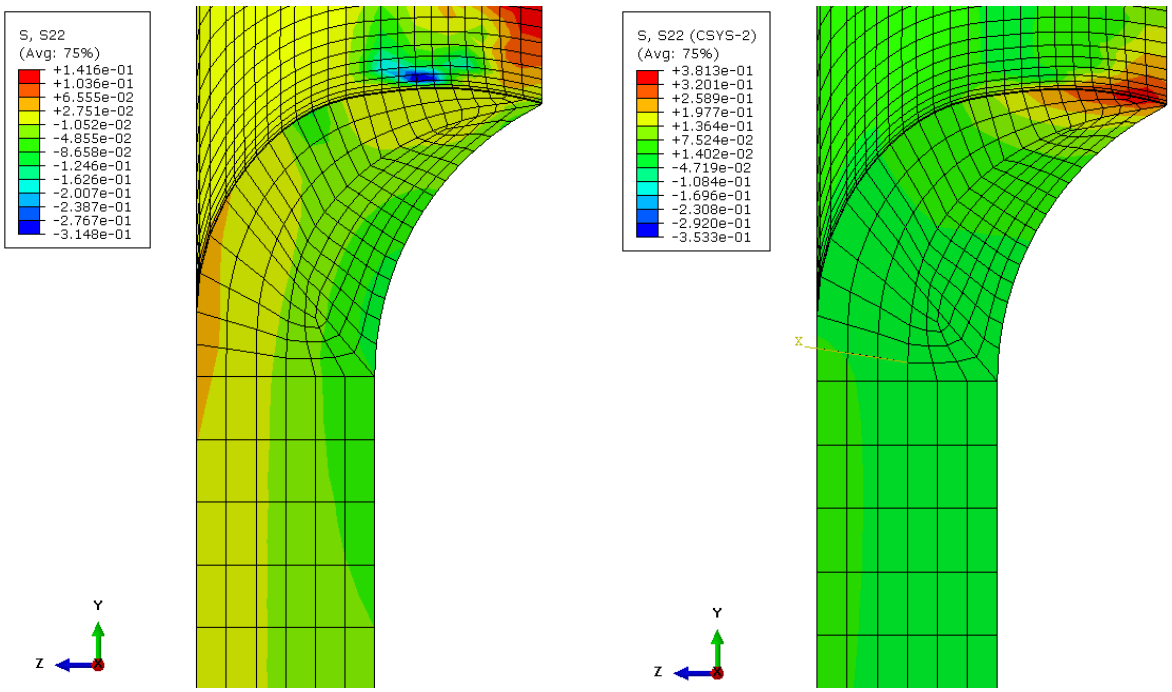

Figure 95: Global S22 contour plot of 90° top sheet tension side from Al 6016 2mm by 2mm model (left) and S22 contour plot transformed coordinate system (right)

Appendix D – Extracted S22 Values from Detailed Finite Element Models for Section 7.2

Table 21: Al 6016 1mm by 1mm detailed finite element half model extracted local S22 values with calculated membrane and bending stresses

Loading Orientation	0°		45°		90°	
Angular Location	0°	180°	0°	180°	0°	180°
Node ID:	122	548	121	41	121	41
Maximum S22 [MPa]	1.280	1.273	0.1613	0.3283	0.1281	0.2268
Minimum S22[MPa]	-0.8623	-0.8567	-0.2974	-0.2818	-0.2336	-0.1969
σ membrane [MPa]	0.2091	0.2083	-0.0681	0.0233	-0.0527	0.0149
σ Maximum Bending [MPa]	1.071	1.065	0.2293	0.3051	0.1809	0.2119
σ Minimum Bending [MPa]	-1.071	-1.065	-0.2293	-0.3051	-0.1809	-0.2119

Table 22: Al 6016 1mm by 1mm detailed finite element half model extracted local S22 values with calculated membrane and bending stresses for 45° bending stress decomposition

Loading Orientation	0°		90°	
Angular Location	0°	180°	0°	180°
Node ID:	121	41	121	548
Maximum S22 [MPa]	1.2221	1.3045	0.1281	0.2241
Minimum S22[MPa]	-0.7655	-0.9423	-0.2336	-0.1704
σ membrane [MPa]	0.2283	0.1811	-0.0527	0.0269
σ Maximum Bending [MPa]	0.9938	1.1234	0.1809	0.1972
σ Minimum Bending [MPa]	-0.9938	-1.1234	-0.1809	-0.1972

Table 23: Al 6016 1mm by 1mm detailed finite element half model decomposed S22 values scaled from Table 22 by a factor of $\sqrt{2}$ with calculated membrane and bending stresses for 45° bending stress

Loading Orientation	0°		90°	
Angular Location	0	180	0	180
Node ID:	121	41	121	41
Maximum S22 [MPa]	0.8641	0.9224	0.0906	0.1603
Minimum S22[MPa]	-0.5413	-0.6663	-0.1652	-0.1393
σ membrane [MPa]	0.1614	0.1280	-0.0373	0.0105
σ Maximum Bending [MPa]	0.7027	0.7944	0.1279	0.1498
σ Minimum Bending [MPa]	-0.7027	-0.7944	-0.1279	-0.1498

Table 24: Al 6016 2mm by 2mm detailed finite element half model extracted local S22 values with calculated membrane and bending stresses

Loading Orientation	0°		45°		90°	
Angular Location	0°	180°	0°	180°	0°	180°
Node ID:	1415	329	1415	329	1415	329
Maximum S22 [MPa]	0.2595	0.2595	0.0342	0.1950	0.0352	0.1255
Minimum S22[MPa]	-0.1478	-0.1478	-0.1065	-0.1141	-0.0945	-0.0763
σ membrane [MPa]	0.0559	0.0559	-0.0361	0.0404	-0.0296	0.0246
σ Maximum Bending [MPa]	0.2037	0.2037	0.0703	0.1546	0.0648	0.1009
σ Minimum Bending [MPa]	-0.2037	-0.2037	-0.0703	-0.1546	-0.0648	-0.1009

Table 25: Al 6016 2mm by 2mm detailed finite element half model extracted local S22 values with calculated membrane and bending stresses for 45° bending stress decomposition

Loading Orientation	0°		90°	
Angular Location	0°	180°	0°	180°
Node ID:	1415	329	1409	330
Maximum S22 [MPa]	0.2289	0.2595	0.0349	0.1346
Minimum S22[MPa]	-0.1408	-0.1478	-0.1086	-0.0742
σ membrane [MPa]	0.0441	0.0559	-0.0369	0.0302
σ Maximum Bending [MPa]	0.1848	0.2037	0.0717	0.1044
σ Minimum Bending [MPa]	-0.1848	-0.2037	-0.0717	-0.1044

Table 26: Al 6016 2mm by 2mm detailed finite element half model decomposed S22 values scaled from Table 25 by a factor of $\sqrt{2}$ with calculated membrane and bending stresses for 45° bending stress

Loading Orientation	0°		90°	
Angular Location	0°	180°	0°	180°
Node ID:	1415	329	1415	329
Maximum S22 [MPa]	0.1619	0.1835	0.0249	0.0887
Minimum S22[MPa]	-0.0995	-0.1045	-0.0668	-0.0540
σ membrane [MPa]	0.0312	0.0395	-0.0210	0.0174
σ Maximum Bending [MPa]	0.1307	0.1440	0.0458	0.0713
σ Minimum Bending [MPa]	-0.1307	-0.1440	-0.0458	-0.0713